SOME ASPECTS OF CHEMICAL NON-EQUILIBRIUM IN HIGH SPEED HIGH TEMPERATURE FLOWS

Chul Park
Department of Aeronautics
Imperial College of Science and Technology

1964

ABSTRACT

The effects of dissociative and ionic nonequilibrium on nozzle flow characteristics, the flow in the stagnation region of a sphere and heat transfer rates are investigated both theoretically and experimentally. The content is divided into two parts. Part I describes the work on ionized argon, while Part II is devoted to dissociated nitrogen. The theoretical calculations for nonequilibrium nozzle flow were carried out employing the relaxing gas model suggested by Freeman and using a digital computer. Tests were made in the one-inch arc-heated wind tunnel as follows: i) stand-off distance of a hemisphere, ii) heat transfer rates to a hemisphere and a cone with catalytic and noncatalytic surfaces, and iii) heat transfer by radiation.

Conclusions drawn, among others, are: i) the ionic recombination rate constant of argon is not greater than $5 \times 10^{27} T^{-4.5} \mathrm{cm}^{-6} \mathrm{mole}^{2} \mathrm{sec}^{-1}$ where T is in °K, ii) the variations of shock wave stand-off distance for a sphere due to the frozen nature of the flow are verified, iii) copper, chromium and stainless steel have the surface catalytic reaction rate constants of the order of 10 fps for surface recombination of nitrogen, and two boro-silicate ceramics are much less catalytic than these metals, and iv) the heat transfer to a hemisphere from ionized argon is greater

than that from non-ionized flow and this occurs because the boundary layer is ionically frozen and the cold surface acts as a fully catalytic surface to the ionic recombination.

TABLE OF CONTENTS

INTRODUCTION

The rapid increase in flight speed during recent years has made the studies of high temperature real-gas effects essential. At around 1000 °K, i.e. corresponding to the flight condition of $M \simeq 4$, the vibrational energy of oxygen and nitrogen is excited; at 3000 °K, or $M \simeq 8$, oxygen starts dissociating; at around 8000 °K, or $M \simeq 15$, oxygen and nitrogen start ionizing. These activations are all energy absorbing processes and the amounts of energy involved are of the same order as the total energy of the gas. Therefore the performance of an aircraft flying at high speeds is strongly influenced by these effects.

A considerable amount of work has been done both theoretically and experimentally on real-gas effects at high temperature (Ref. 1 of Part I). As a result, the flow of gas in thermo-chemical equilibrium has come to be understood in some detail. When a potentially active gas is brought to a high temperature from a cold state, or vice versa, it takes a finite time before it reaches a steady state. The ultimate state beyond which the activation does not proceed is called the equilibrium state. The equilibrium state is a function of thermodynamic properties only, and therefore involves less uncertainty. The greater difficulty is in the so-called nonequilibrium state, where the gas is in the process of reacting to reach equilibrium.

Since the flow conditions encountered in hypersonic reentry include those in all degrees of nonequilibrium state as well as equilibrium, the knowledge of nonequilibrium flow is essential to the understanding of real-gas effects.

There are mainly two types of facility for producing the high temperature flow suitable for real-gas effect research, namely the shock-tube and the arc-heated, or plasma-jet wind tunnel. Of these, the shock-tube has two serious limitations, i.e. the short duration and the limit on the attainable energy level of the gas. The development of the plasma-jet wind tunnel, which is essentially free of the above limitations, is only recent and many of the basic problems of arc-heating are still unresolved (Ref. 2 of Part I). Because of this uncertainty in the arc-heating mechanism, the experimental work one can carry out at the present stage in the field of nonequilibrium real-gas effects with a plasma-jet wind tunnel is quite limited.

The purpose of the present work is to investigate some of the most important nonequilibrium real-gas effects relevant to the plasma-jet wind tunnel test conditions. Dissociation and ionization are treated mainly because they are the most serious effects, and electron temperature equilibration and molecular vibration are mentioned in connection with the two main effects. The discussions are divided into two parts, the first part is devoted to ionized argon flow while the second part is concerned with dissociated nitrogen. In both parts, the processes considered are i) the wind tunnel nozzle flow, ii) the flow in the stagnation region of a hemisphere iii) boundary layer flow with heat transfer, and iv) radiation from the jet exit flow.

The theoretical basis of this work is taken from the existing literature and the theoretical treatment contained here is mostly an extension and detailed manipulation of such theories. The entire work is aimed to derive useful conclusions on: i) heat transfer to a reentering body, and ii) basic physical quantities related to the reentry problem, i.e. reaction rates, transport properties and surface catalytic activities.

PART I

FLOW OF IONIZED ARGON

I-1. LIST OF SYMBOLS

A : nozzle cross-sectional area

C_p : frozen specific heat at constant pressure

D : diffusivity

$\left(\frac{du_e}{dx}\right)_o$: stagnation point velocity gradient

E : electrical energy input to plasma-jet head

e : voltage across head electrodes

f : velocity profile function ($f' = df/d\eta = u/u_e$)

g : energy profile function = h_t/h_{te}

H : enthalpy = $h + \phi h_i$, Btu/lb unless otherwise stated

H_t : total enthalpy = $H + \frac{1}{2}u^2$ "

h : frozen enthalpy = $C_p T$ "

h_i : ionization energy = 16,300 Btu/lb

h_t : frozen total enthalpy = $h + \frac{1}{2}u^2$, Btu/lb unless otherwise stated

I : electrical current to head electrodes

j : = 0 for two-dimensional flow and = 1 for axisymmetric flow

K : local Damköhler number

k : rate constant, $cm^6 mole^{-2} sec^{-1}$

L_e : Lewis number

$\dot{M}$: water flow rate through head cooling passage

$\dot{m}$: gas mass flow rate through tunnel, lb/min unless otherwise stated

N : molar number of particles
n : $=\rho\mu/(\rho\mu)_e$
p : pressure
Q : overall heat transfer rate
q : local heat transfer rate
R : gas constant or nose radius
r : distance from center line
S_c : Schmidt number
T : temperature, ^{o}K
T_e : electron temperature, ^{o}K
T_i : reference temperature = $182{,}100^{o}K$
u, v : velocity in x and y direction
W : plasma-jet head cooling water loss
x, y : distance along and normal to wall
x_o : reference length
Γ : throat-mass flow parameter, see Eq. (23)
γ : effective frozen specific heat ratio
Δ : stand-off distance of bow shock wave
η : plasma-jet head efficiency
λ : frozen thermal conductivity
μ : viscosity
ξ, η : dimensionless length parameter in x and y direction
ρ : density, $cm^{-3}mole$

ρ_i : reference density = 3,78 cm^{-3}mole

σ : frozen Prandtl number

σ_E : equilibrium Prandtl number

τ : relaxation time

ϕ : ionization fraction

Subscripts

a : atom

c : critical point

E : equilibrium

e : edge of boundary layer or shock layer

F : frozen

mf : mass flow method

pb : power balance method

w : wall

ε : electron

$*$: nozzle throat

∞ : test section of wind tunnel

I-2. THEORY

I-2.1. Fundamentals of nonequilibrium ionized argon

It is known that the state of a gas in thermo-chemical equilibrium can be determined by using the partition functions when these are known. (In the present work the term thermodynamic equilibrium will be used to inherent to a Maxwell - Boltzmann distribution as well as vibrational equilibrium, while chemical equilibrium is referred to the equilibration of reactions between different species, i.e. dissociative and ionic equilibrium.) For a pure monatomic gas, Bray and Wilson (Ref. 3) have shown that the flow of gas can be approximated by using an ideal ionizing gas model, which neglects the second order terms in the partition function. In the ideal ionizing gas, the equilibrium ionization fraction is determined by the simplified Saha equation (Ref. 3)

$$\frac{\phi_E^2}{1-\phi_E} = \frac{\rho_i}{\rho}\left(\frac{T}{T_i}\right)^{\frac{3}{2}} \exp\left(-\frac{T_i}{T}\right) \qquad (1)$$

where ϕ is the ionization fraction

$$\phi = \frac{N_i}{N_a + N_i}$$

and the subscripts a and i refer to the neutral atoms and ions, respectively. Eq. (1) is accurate to approximately 5% within the range (Ref. 3)

$$0.005 < \phi < 0.9$$

$$0.001 < p < 100 \quad \text{atm.}$$

The state of gas is determined by (Ref. 4)

$$p = \rho RT\left(1 + \phi \frac{T_\varepsilon}{T}\right) \tag{2}$$

The electron temperature T_ε is not necessarily equal to the atom temperature T in a nonequilibrium ionized gas because i) the collisions involving electrons are accompanied by radiation and therefore are not generally elastic ones, and ii) the frequency of collisions between atoms and electrons is much smaller than those between the same species and so the electron temperature may lag behind atom temperature, or vice versa, in a changing flow state. The enthalpy of the ideal ionizing monatomic gas is

$$H = h + \phi h_i = C_p T + \phi h_i = 2.5\left(1 + \frac{T_\varepsilon}{T}\phi\right)T + h_i\phi \quad . \tag{3}$$

The equilibrium electron temperature $T_{\varepsilon E}$ is controlled by the radiative property of the gas. In the weakly ionized regime ($\phi \leq 0.2$ for argon) the effect of radiation is very small (Ref. 5) and the equilibrium electron temperature is approximated with sufficient accuracy by

$$T_{\varepsilon E} = T \quad . \tag{4}$$

In the present work, the consideration is limited to this regime only, and so Eq. (4) is used throughout.

In a nonequilibrium flow, the electron temperature and ionization fraction are changing with time even for fixed enthalpy and pressure, i.e. relaxing, and must be determined by the relevant rate equations. For the relaxation of electron temperature, Spitzer (Ref. 6) derived the rate equation, which can be written for argon gas as

$$\frac{\partial T_\varepsilon}{\partial t} = 7.32 \times 10^{16} p\phi (\log_e \Lambda) T^{-2} (T - T_\varepsilon) \qquad (5)$$

where $\Lambda = 4.59 \times 10^{-7} \frac{T^2}{\sqrt{p\phi}}$.

For ionic relaxation, Bray (Ref. 3) derived the necessary rate equation in the same way as Freeman (Ref. 7) derived the rate equation for dissociating gas, which can be written, neglecting radiative recombination, as

$$\frac{\partial \phi}{\partial t} = k\rho_i \rho\phi \left\{ \left(\frac{T}{T_i}\right)^{\frac{3}{2}} (1 - \phi)\, e^{-\frac{T_i}{T}} - \frac{\rho}{\rho_i} \phi^2 \right\} \qquad (6)$$

The rate constant k was obtained experimentally for the shock-compression flow for argon by Byron and Petschek (Ref. 5) as

$$k = 9.2 \times 10^{15} \left(\frac{133{,}600}{T_\varepsilon} + 2 \right) \exp\left(-\frac{48{,}200}{T}\right) \qquad (7)$$

Similarly for a recombining flow with hydrogen, helium and argon Hinnov and Hirschberg (Ref. 8) obtained

$$k = 5.0 \times 10^{27} T^{-4.5} \qquad (8)$$

The condition necessary for Eq. (5) to hold is that the mean free path of neutral atoms is sufficiently smaller than the scale of the flow field for the velocity distribution of the neutral atoms to be regarded as Maxwellian. Eq. (6) holds for a dense plasma in which the radiative recombination is negligibly small compared with the total relaxation rate. In the calculation of ionization level, however, radiative recombination can be neglected even if it is the major process provided the absolute rate of the radiative recombination is small compared with the total ionization level. The rate constant of Eq. (7) holds for any continuum flow in which the fundamental equations (1) to (3) are valid, and Eq. (8) holds when the electron density is greater than $10^{11}\,\mathrm{cm}^{-3}$ for $T > 1000^{\circ}K$.

By introducing the relaxation time τ, the rate equation (5) can be written in the form

$$\frac{\partial T_g}{\partial t} = \frac{T - T_g}{\tau} \tag{9}$$

The rate equation (6) which is nonlinear can also be written in the form of Eq. (9). The appropriate relaxation time in the latter case is a function of ϕ as well as other properties.

I-2.2. Steady one-dimensional nozzle flow

The adiabatic steady one-dimensional flow of non-equilibrium ionized argon can be solved using Eqs. (1) to (9) and the following basic nozzle flow equations;

continuity : $\rho u A = \dot{m} = \mathrm{const.}$ (10)

momentum : $u\dfrac{du}{dx} = -\dfrac{1}{\rho}\dfrac{dP}{dx}$ (11)

energy : $$H_t = H + \frac{u^2}{2} = \text{const.} \tag{12}$$

For one-dimensional steady flow, the rate equation (9) becomes

$$\frac{dT_\varepsilon}{dx} = \frac{T - T_\varepsilon}{u\tau} \tag{13}$$

(Note also that Eq. (6) can be written in the same form as Eq. (13) with T_ε replaced by ϕ and T replaced by ϕ_E).

By introducing the dimensionless length parameter

$$\xi = \frac{x}{x_0}$$

where x_0 is an arbitrary reference length, Eq. (13) can be written as

$$\frac{dT_\varepsilon}{d\xi} = K(T - T_\varepsilon) \qquad K \equiv \frac{x_0}{u\tau} \tag{14}$$

When K is very large, T_ε (or ϕ) tends to equalize rapidly with T (or ϕ_E), i.e. a near equilibrium flow. When K is very small, T_ε (or ϕ) remains almost unchanged, i.e. near frozen flow. Thus K is the main factor controlling the degree of relaxation. Since x_0/u represents the time taken to travel the distance x_0 at the velocity u, x_0/u is called the mechanical transit time. K is then the ratio of mechanical transit time to the relaxation time τ, and is called the local Damköhler number. The representative or characteristic Damköhler number of a system is obtained by substituting for u and τ the most representative values of velocity and relaxation time in the system.

In order to determine the flow properties in ionized argon, one must solve Eqs. (5) and (6) simultaneously with the conservation equations (10) to (12). The flow system therefore involves two degrees of relaxation. Since it is extremely difficult to solve Eqs. (5) and (6) simultaneously for a nozzle flow starting from a settling chamber, consideration is limited in the present work to those problems in which the departure of electron temperature from the atom temperature is small and may be neglected. Thus, for the calculation of ionic recombination, the approximation

$$T_\varepsilon = T_{\varepsilon_E} = T \quad \text{(for Eq. (6) only)} \qquad (15)$$

is used. The variation of electron temperature T_ε is then calculated from the ionization fraction values obtained by using the simplification of Eq. (15). The resulting distributions of ϕ and T_ε are therefore the first approximations to the true solutions, and the procedure comprises a kind of small perturbation method. The solutions are accurate, therefore, to the order of magnitude of the largest neglected terms in Eqs. (17) to (19), which is $(1 - T/T_\varepsilon)^2$.

The electron temperature relaxation and ionic relaxation are now mathematically decoupled and the resulting equations are;

$$H_t = 2.5(1+\phi)RT + \phi h_i + \frac{u^2}{2} = \text{const.} \tag{16}$$

$$\frac{1}{T}\frac{dT}{dx} = \frac{\frac{1}{A}\frac{dA}{dx} - \frac{d\phi}{dx}\left\{\frac{1}{1+\phi} - \left(\frac{\rho}{p} - \frac{1}{u^2}\right)\left(2.5T + \frac{h_i}{R}\right)R\right\}}{1 - \left(\frac{\rho}{p} - \frac{1}{u^2}\right) \times 2.5(1+\phi)RT} \tag{17}$$

$$\frac{d\phi}{dx} = \frac{k\rho_i\rho}{u}\phi\left\{\left(\frac{T}{T_i}\right)^{1.5}(1-\phi)e^{-\frac{T_i}{T}} - \frac{\rho}{\rho_i}\phi^2\right\} \tag{18}$$

$$\frac{dT_e}{dx} = 7.32 \times 10^{16}\frac{p\phi\log_e\Lambda}{T^2}(T - T_e)\ , \tag{19}$$

$$\Lambda = 4.59 \times 10^{-7}\frac{T^2}{\sqrt{p\phi}}$$

Note here that although the system of equations include two degrees of relaxation, effectively it involves only one degree of relaxation, because the electron temperature does not come into the temperature equation (17).

The solution of Eqs. (16) to (19) for a supersonic flow is straightforward if $\overset{\circ}{m}$ is given as an initial condition. For a convergent-divergent nozzle flow starting from rest, there are two singular points in the low speed region. One singular point occurs when the denominator of RHS in Eq. (17) is zero. Since the LHS of Eq. (17) is finite, the numerator of Eq. (17) must also be zero at this singular point. In the *perfect gas* in which $d\phi/dx$ is zero, the singular point is at the point $dA/dx = 0$, i.e. the throat. In a flow with recombination, in which $d\phi/dx < 0$, this singular point is in the divergent portion of the nozzle because the quantity in the parenthesis in the numerator of Eq. (17) is positive. Another singular point is at the settling chamber where $u = 0$, making Eqs. (18) and (19) indeterminate.

The boundary conditions for Eqs. (17) to (19) are given by the condition in the settling chamber. In the present work, it was assumed that the flow is completely in equilibrium for all reactions and activations in the settling chamber, i.e.

at $x = -\infty$ (in the settling chamber)

$$T = T_0 \tag{20a}$$

$$\phi = \phi_{E0} \tag{20b}$$

$$T_g = T \tag{20c}$$

In order to satisfy these conditions, Eqs. (17) and (18) must be first solved for the subsonic region between the two singular points to find the correct value of mass flow rate $\dot{m}$. In the present work, the solution in the subsonic region is obtained by solving Eqs. (17) and (18) consecutively. The temperature equation (17) is first solved with an assumed distribution of along the nozzle, starting from the downstream singular point. The temperature distribution obtained from this integration is fed into the ionic relaxation equation (18), which is integrated from the settling chamber toward downstream. The resulting ϕ distribution is also fed into Eq. (17) to solve for T and so on.

In the first upstream integration, the mass flow rate $\dot{m}$ is assumed. When the upstream integration of Eq. (17)

is terminated at a point sufficiently upstream of the throat, the resulting pressure and temperature are compared with the given settling chamber values and the mass flow rate $\dot{m}$ and the temperature values are corrected in accordance with Newton's iterative principle. The iteration is repeated until the terminal values of upstream integration agree with the given settling chamber conditions.

The downstream singularity of Eq. (17) is overcome by choosing the initial values of integration such that Eq. (17) is satisfied in the limit, i.e.

$$\left(\frac{dT}{dx}\right)_c = \lim_{x \to x_c} \left[\text{Eq. (17)} \right] \qquad (21)$$

The values of ϕ, $d\phi/dx$ and $d^2\phi/dx^2$ necessary for the evaluation of Eq. (21) are obtained from the preceding solution of Eq. (18). For the first approximation, both ϕ and $d\phi/dx$ are assumed as varying linearly with x. Once the distribution of ϕ is specified through the nozzle, the value of T at some point Δx upstream of the singular point can be determined by $\Delta T = (dT/dx)\,\Delta x$ using Eq. (21) and by the conditions for a singularity in Eq. (17), i.e. both the numerator and denominator are zero, together with the conservation equations (10) to (12). The singular point for Eqs. (18) and (19) is avoided by starting the integration from a finite velocity, i.e. from the point where $A/A_* = 5$.

Once the solution for the low speed region is found, the solution for the divergent portion of the nozzle is straightforward. The limiting value of Eq. (21) is again used as the initial slope for temperature in the downstream integration.

The problem was solved numerically using the Ferranti Mercury digital computer for the flow of argon through a typical convergent-divergent nozzle for a total of 18 sets of operating conditions. Because the flow through such a nozzle is a recombining flow, the form of the rate constant is taken to be the same as that derived by Hinnov and Hirschberg (Ref. 8) from measurements in recombining conditions. The magnitude of the rate constant is varied as 0.1k, k and 10k, where k is the value obtained by Hinnov and Hirschberg. The nozzle shape taken for the computation was the one incorporated in the Imperial College one-inch plasma-jet wind tunnel (Fig. 1), which was approximated by a hyperbola in the convergent portion and up to the point $x = 0.8$ inch in the divergent portion, and by a parabola

$$\frac{A}{A_*} = 1.023x(\text{inch}) + 0.5$$

in the rest of the nozzle. The hyperbola and parabola chosen match each other smoothly at $A/A_* = 1.323$. The settling chamber conditions chosen are also those of the Imperial College plasma-jet wind tunnel. For the 18 cases chosen, the computation has shown that the iterative method converges with a fixed step number of 150 and reaches the stable solution within 6 iterations. The results of integration are presented

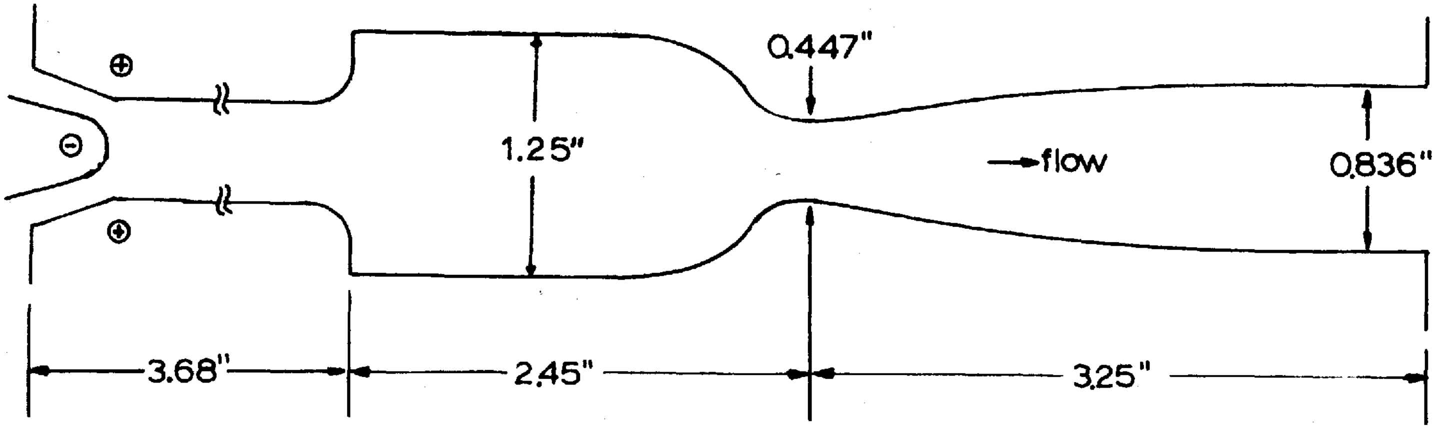

Fig. 1. Geometry of electrodes, settling chamber and nozzle of Imperial College one-inch plasmajet wind tunnel

in Figs. 2(a) to 2(c).

As seen from the figures, there is moderate relaxation both in the electron temperature and ionization fraction under these conditions. The electron temperature is only slightly higher than the atom temperature at the ionization levels $\phi_0 > 0.02$, and by up to 30% at the very low ionization levels $\phi_0 < 0.005$. Thus the requirement set earlier, in Eq. (15), that the electron temperature is equal to the atom temperature (for the calculation of ionic recombination only), is met to the first approximation for these conditions. The ionization fraction falls steadily through the nozzle and there is no 'sudden freezing' point in the flow, a trend which was shown by Bray (Ref. 4). The temperature and pressure are appreciably increased by the recombination in the divergent portion of the nozzle, and the exit temperature and pressure are sensitively affected by the recombination rate used in the calculation under these circumstances.

The equation of continuity through the nozzle

$$\dot{m} = \rho_* u_* A_*$$

can be rearranged, by using Eqs. (2), (3) and (15), as

$$h_0 = 2.5\left(\frac{\Gamma p_0 A_*}{\dot{m}}\right)^2 \tag{22}$$

where Γ is the throat-mass flow parameter

$$\Gamma = \frac{\rho_*}{\rho_0}\frac{u_*}{\sqrt{(1+\phi_0)RT_0}} \quad . \tag{23}$$

The parameter Γ was calculated from the computed results

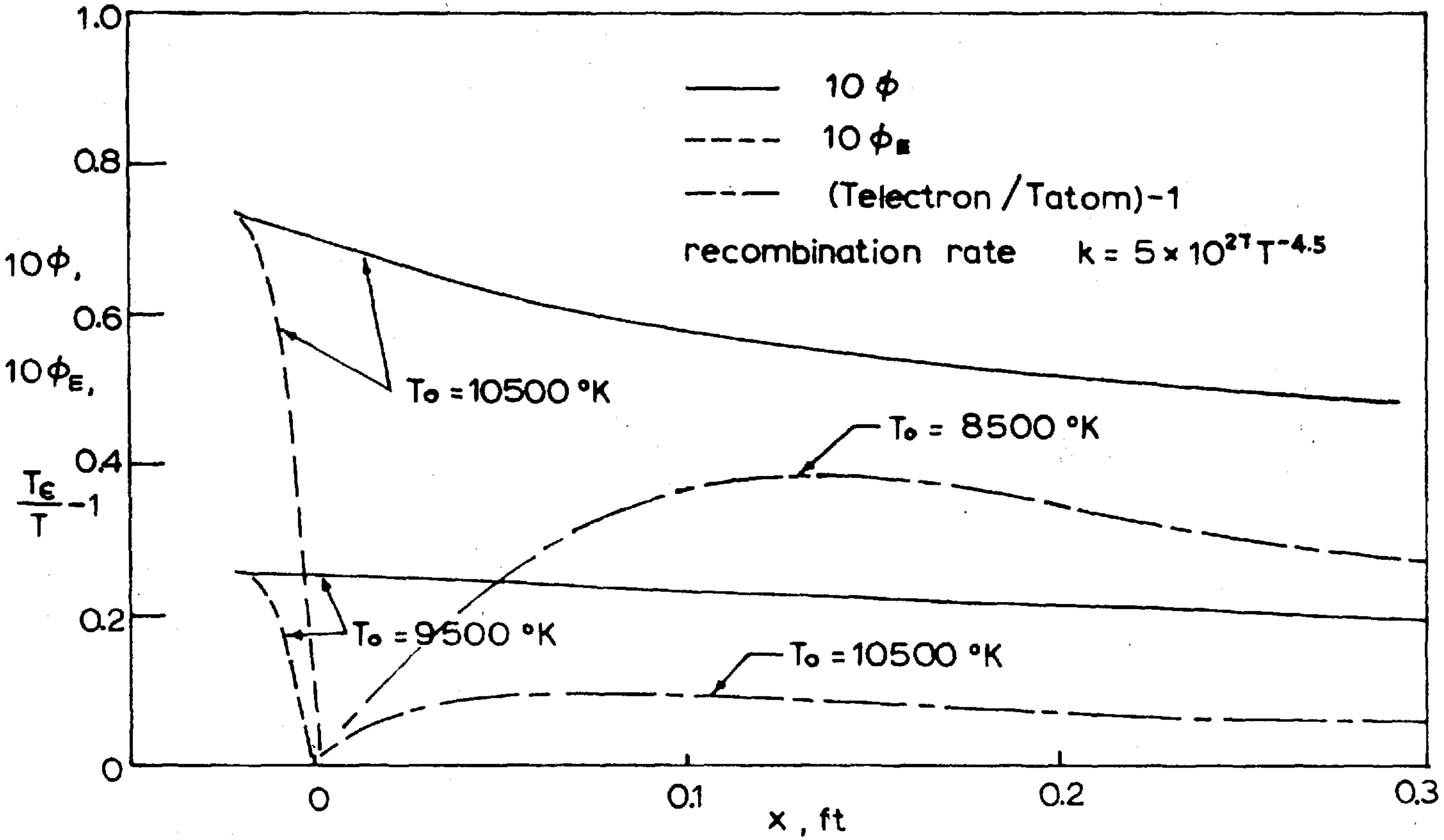

Fig. 2(a). Typical variation of ionization fraction and electron temperature along the wind tunnel nozzle, computed result, $A_\infty/A_* = 3.5$, $p_o = 0.25$ atm.

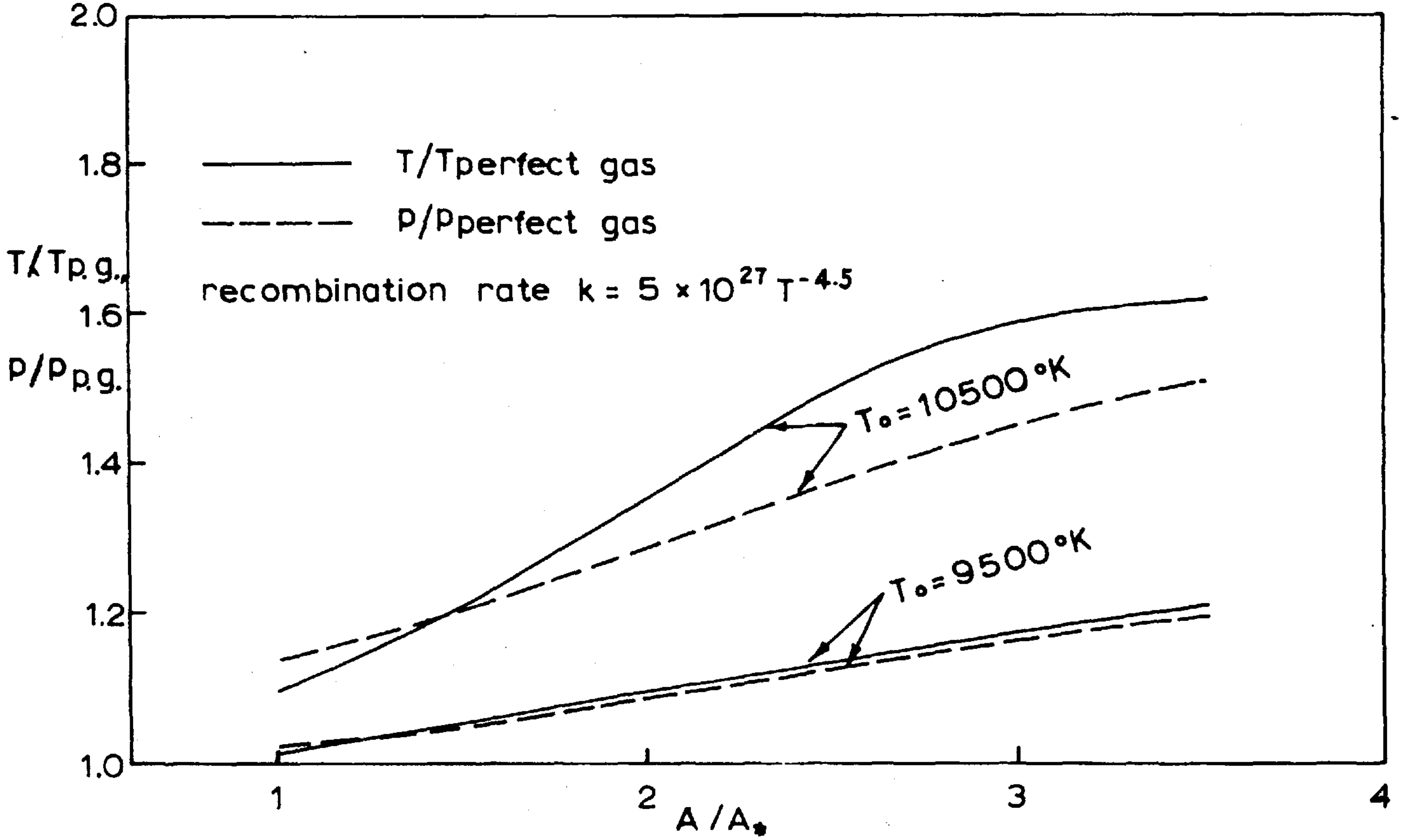

Fig. 2(b). Typical variation of temperature and pressure along the wind tunnel nozzle, computed result, $p_o = 0.25$ atm.

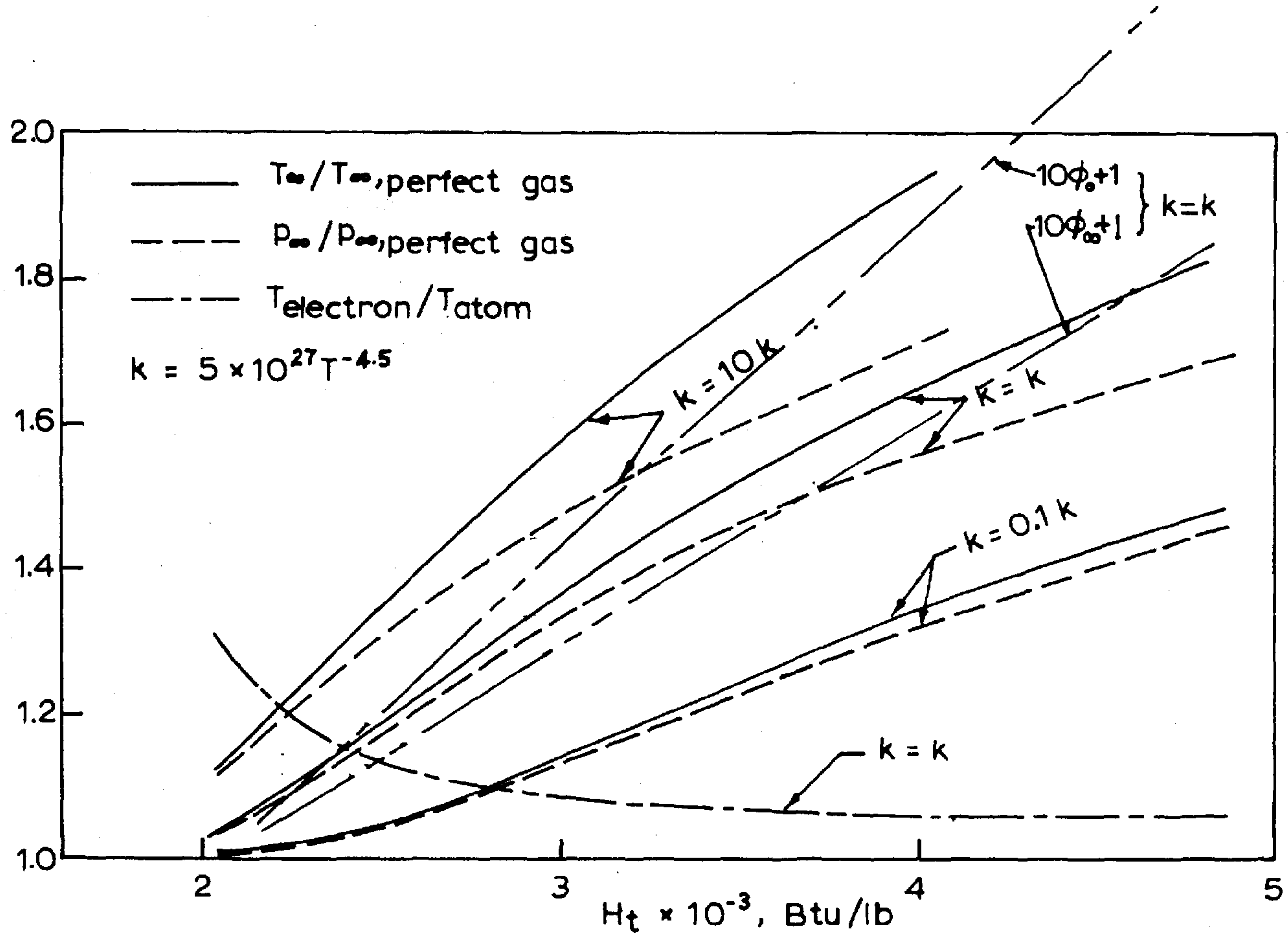

Fig. 2(c). Variation of exit condition with enthalpy level, computed result, $A_\infty / A_* = 2.7$, $p_o = 0.25$ atm, for the reaction rates k = 10k, k and 0.1k.

of nozzle flow properties and was found to be closely equal to

$$\Gamma = 0.725 \quad (|\text{error}| < 15\%) \qquad (24)$$

for all the cases considered. The value 0.725 is the value for the perfect gas ($\gamma = 5/3$). The results of computation show therefore that the frozen enthalpy is related to the factor $(p_0/\dot{m})^2$ in exactly the same way as in the perfect gas and is directly proportional to $(p_0/\dot{m})^2$, for the range of conditions considered.

I-2.3. Shock wave stand-off distance of a sphere

When a sphere is placed in a wind tunnel nozzle, the flow process across the bow shock wave of the sphere and within the shock layer are in general affected by the relaxation phenomena within the nozzle. When the stand-off distance is very small compared with the nozzle length there are in general three limiting cases in the degree of nonequilibrium in the flow through the nozzle and shock wave of the sphere. They are, in descending order of Damköhler number;

i) case E-E; equilibrium both through the nozzle and behind the shock, here, K is very large,

ii) case E-F; equilibrium through the nozzle but frozen behind the shock, K intermediate, and

iii) case F-F; frozen both through the nozzle and behind the shock, K small.

A fourth condition, i.e. the case F-E (frozen through the nozzle and equilibrium behind the shock) is not likely to occur because the characteristic length behind the shock wave is obviously much smaller than the nozzle length.

For the above mentioned limiting cases, density does not vary much within the shock layer in the direction perpendicular to the wall. Thus the shock layer theory of perfect gas (see e.g. Ref. 9) can be used to calculate the shock wave stand-off distance. According to the shock layer theory of a perfect gas, the relative shock stand-off distance is very closely a function only of density ratio

$$\frac{\Delta}{R} = f\left(\frac{\rho_\infty}{\rho_e}\right)$$

where ρ_∞ and ρ_e are the densities in the freestream and at the point just behind the normal portion of the bow shock wave. Comparing with the experimental results of Ref. 10, it is seen that for density ratios of around 4, the stand-off distance is best approximated by

$$\frac{\Delta}{R} = \frac{0.58}{\frac{\rho_e}{\rho_\infty} - 1} \; . \tag{25}$$

When the flow is ionically frozen behind the bow shock wave, (here, and in the following discussions, the electron temperature is assumed to be the same as the atom temperature), regardless of the degree of ionization and degree of nonequilibrium in front of the shock, the density ratio is then determined by the Rankine-Hugoniot relation for a perfect gas, i.e. $\gamma = 5/3$ (Ref. 3). When the flow behind the shock is in equilibrium, the density ratio is determined, again irrespective of the degree of nonequilibrium in the freestream, by solving the normal shock relations,

$$\rho_\infty u_\infty = \rho_e u_e$$

$$\rho_\infty u_\infty^2 + p_\infty = \rho_e u_e^2 + p_e$$

$$H_{t\infty} = H_{te}$$

simultaneously with Eqs. (1), (2) and (15). Of the three limiting cases mentioned earlier, the cases E-F and F-F will result in the same stand-off distance, because in both cases the density ratio is determined by the perfect gas relation. Thus the shock wave stand-off distance of a sphere placed in the test section of a wind tunnel is determined in an ionized monatomic gas only by the degree of nonequilibrium behind the shock wave in the above mentioned limiting cases, i.e. independent of the condition in the freestream.

The shock wave stand-off distance of a 0.4" diameter sphere placed in the nozzle considered in §I-2.2. under a varying enthalpy levels, is calculated for the two limiting cases of frozen and equilibrium flows behind the shock using Eq. (25), and the results are shown in Fig. 3. The effective area ratio of the nozzle in this calculation is taken as 2.7 so that the result can be compared directly with experiment (see §I-3.2. Note that the nozzle profile does not come into consideration in either equilibrium or frozen ionized flows.). The displacement thickness of the shock layer is calculated

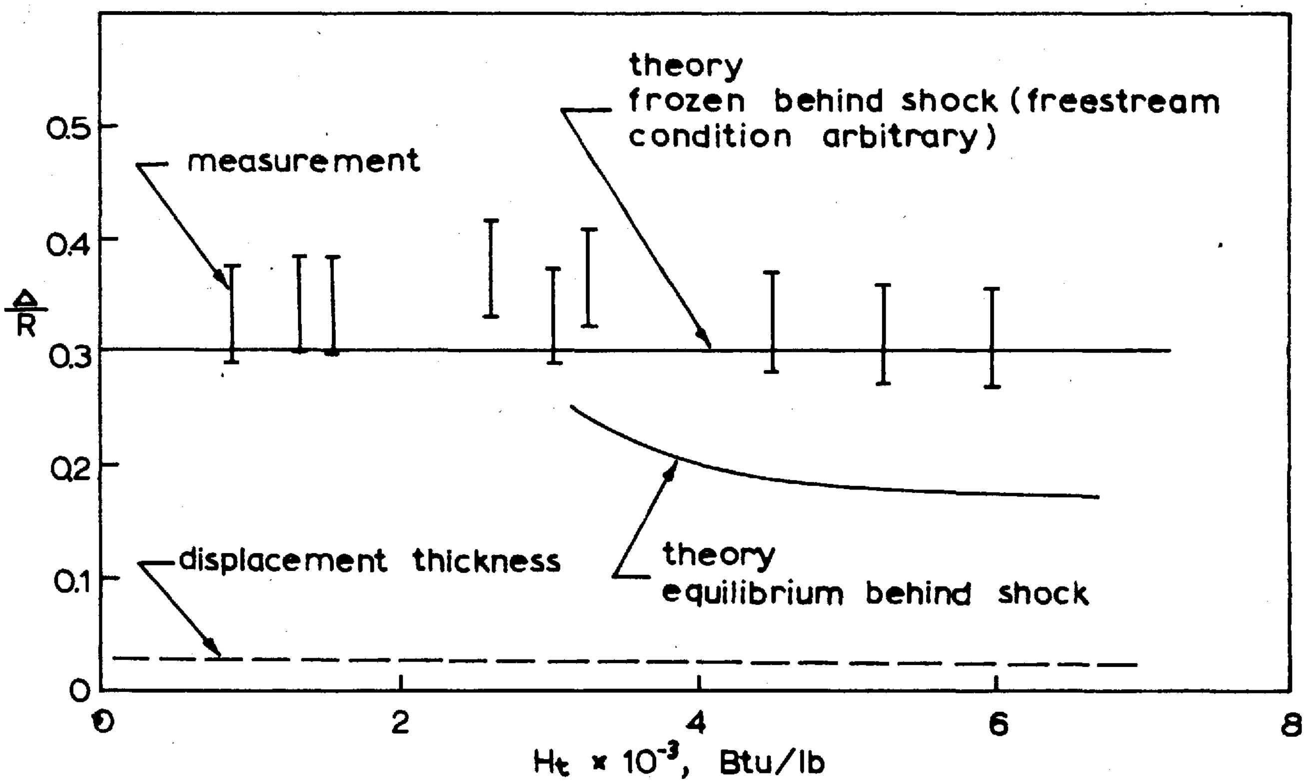

Fig. 3. Shock wave stand-off distance of hemisphere in ionized argon, measurement at $\dot{m} = 0.15$ lb/min.

by the theory of Van Dyke (Ref. 29) for the sample flow conditions pertaining to the computed solutions in §I-2.2. and is added to the thickness of the shock layer to calculate the total stand-off distances shown in Fig. 3.

The exact stand-off distance in a general relaxing ionized gas flow is at present unknown. It is inferable however that the true stand-off distance in the relaxing flow must lie between the two limiting theoretical values of frozen and equilibrium flows. For the flow conditions solved in §I-2.2., one expects that the actual stand-off distance may be close to the frozen flow values because the flow through the nozzle is only mildly relaxing.

I-2.4. Boundary layer and heat transfer*

The effect of ionization on boundary layer flow was originally estimated by Rutowski (Ref. 12) and Adams (Ref. 13). By extending the known property of the solution of boundary layer equations, they concluded that the heat transfer rate from an ionized gas may not be much different from that of a nonionized gas. Following these two authors, Cohen (Ref. 14), Hoshizaki (Ref. 15), and Pallone and Van Tassell (Ref. 16) solved the case for the boundary layer flow of equilibrium air using Hansen's data for the transport

---

*An abridged version of this section, along with the experimental counterpart, §I-3.3., is published as Ref. 26.

properties (Ref. 17); and Fay and Kemp (Ref. 18) treated both equilibrium and frozen cases using Yos's data (Ref. 19). The works mentioned above give results which are similar to each other and they show a general trend of decreasing Nusselt number in the ionized regime, the rate of decrease being more rapid with equilibrium flows than with frozen flows. Experimental results of Rose and Stankevics (Ref. 20) agree approximately with the equilibrium flow theories of the above mentioned authors. Quite independently from these authors, Scala and Warren (Ref. 21) studied the case of air both theoretically and experimentally and report that the heat transfer rates increase remarkably in the ionized regime.

Since there is such a disagreement on the reported effects of ionization and since there is no rigorous theoretical treatment, so far as the present author is aware, on the boundary layer flow of nonequilibrium ionized argon gas, a theory using a simplified binary gas model is developed in the following section.

I-2.4.1. Transport properties of nonequilibrium ionized argon

It is known (Ref. 22) that in an ionized boundary layer, the strong Coulomb attraction between the opposite charges prevents electrons from diffusing faster through the cold layer and that the ions and electrons diffuse effectively in pairs at twice the rate of diffusion of the ions. This is termed 'ambipolar diffusion'. Because of this effect, charge separation does not occur, at least in continuum flow, and the boundary layer flow of a nonequilibrium ionized gas can be treated as a neutral plasma flow, i.e. as an electrically neutral mixture of ions, electrons and neutral atoms.

The transport properties of nonionized argon gas at high temperatures are calculated by Admur and Mason (Ref. 23) and those of ionized argon by Penski (Ref. 24). The viscosity values at 0.1 atm obtained by these authors are compared in Fig. 4. As seen from Fig. 4, the two calculations agree approximately in the nonionized regime, $T < 8000^{\circ}K$. In the present work, the viscosity in this region is approximated by

$$\mu = 8.86 \times 10^{-4} \left(\frac{T}{2000}\right)^{0.784} \text{ poise, } (T < 8000^{\circ}K). \quad (26)$$

In the ionizing region, i.e. $T \geqslant 8000^{\circ}K$, the data of Admur and Mason cannot be used because the effect of ionization is neglected in their calculation. The viscosity value given by Penski is approximately constant within the region $8000^{\circ}K < T < 12{,}000^{\circ}K$. Here, it is approximated by

$$\mu = 26.3 \times 10^{-4} \text{ poise, } (8000^{\circ}K < T < 12{,}000^{\circ}K). \quad (27)$$

The Prandtl number is strongly affected by ionization and therefore the data of Admur and Mason cannot be used for the calculation of Prandtl number. In Fig. 5, the variation of equilibrium and frozen Prandtl numbers calculated by

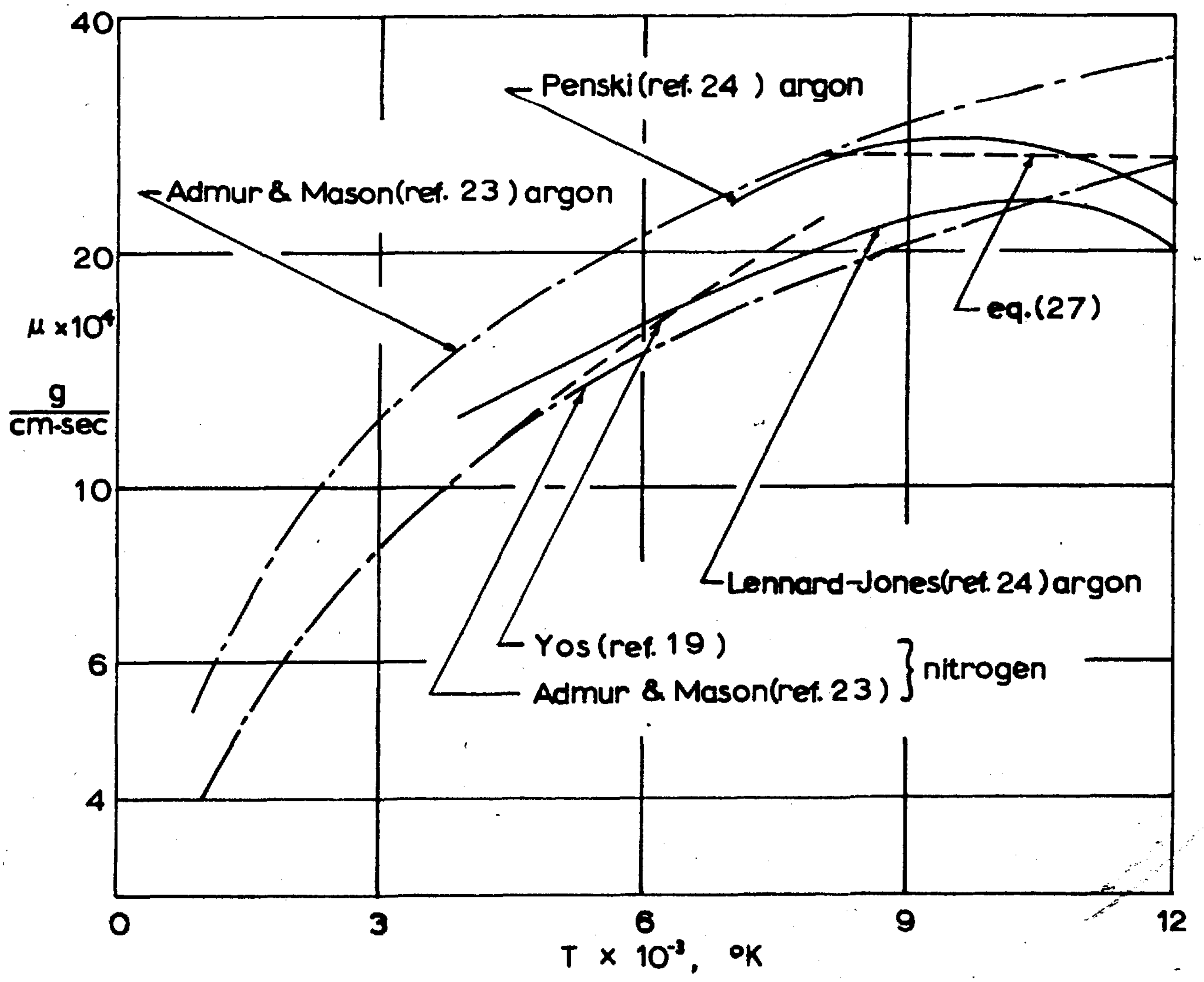

Fig. 4. Viscosity of argon and nitrogen at high temperatures

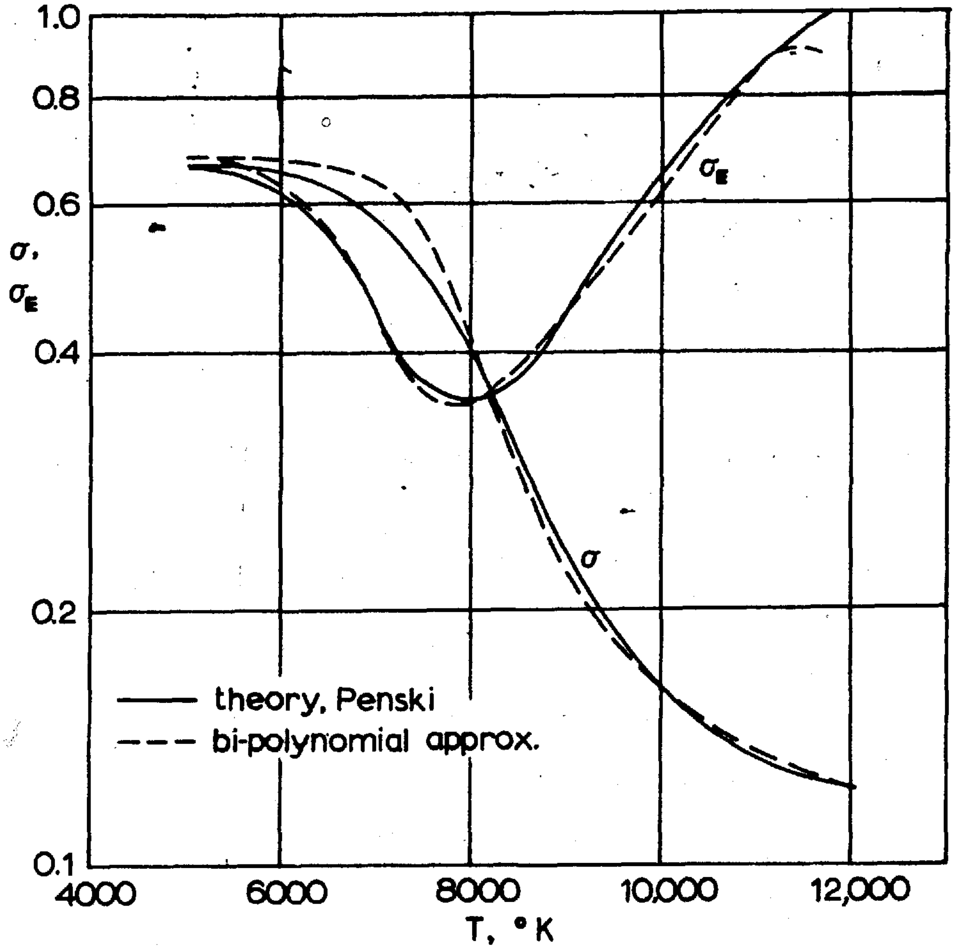

Fig. 5. Frozen and effective equilibrium Prandtl numbers for argon at 0.1 atm.

Penski are shown for $p = 0.1$ atm (here the term frozen Prandtl number is used to denote the Prandtl number based on energy transfer by collision alone, and equilibrium Prandtl number by collision and recombination under equilibrium conditions, see Hansen (Ref. 17)). As seen from Fig. 5, the frozen Prandtl number decreases very rapidly as ionization commences. This is a result of a very small electron-atom collision cross-section. Because of the particular wave nature of the argon atom, the electron-atom collision cross-section is extraordinarily small for argon gas at around $T = 8000^{\circ}K$ (Refs. 24 & 25). The electron-atom collision cross-section used by Penski varies from about $1.6 \times 10^{-16} cm^2$ at $7000^{\circ}K$ to about $3 \times 10^{-16} cm^2$ at $12,000^{\circ}K$, which is at least one order smaller than any other collision cross-sections in air or its component gases (Ref. 19).

For the purposes of computation, the Prandtl numbers are approximated by the ratios of two second order polynomials in the ionization fraction. These bi-polynomial approximations of the Prandtl numbers are compared with exact values in Fig. 6.

The transport properties of nonequilibrium ionized argon are so far unknown. In the present work, therefore, the nonequilibrium properties are derived from the equilibrium properties using the following assumptions;

i) Viscosity is independent of ionization; this is approximately true in a weakly ionized gas, $\phi < 0.1$ say.

ii) Prandtl number is a function of ionization fraction alone. This is true if the collision cross-sections of the various events remain constant. In actual fact, collision cross-sections do not vary greatly except for the case of the Coulomb cross-section. In a weakly ionized gas, the contribution of charge-charge collisions to the total energy transport is very small, and hence the approximation is valid.

iii) The effective Schmidt number for electron diffusion is $\frac{1}{2}$. This is based on the assumption that the effective Schmidt number of ions is unity in an ideal case where the ambipolar diffusion effect is absent, which is approximately true. The exact Schmidt number is not available.

I-2.4.2. Boundary layer equations and their solutions

The fundamental equations of motion of an ionized gas can be derived from the work of Hirschfelder, Curtiss and Bird (Ref. 27). The resulting general equations are, however, too complicated to solve, and also the transport properties needed in the general form of the equations are not all known. There are three different approaches to simplify the fundamental equations of motion into those of a binary mixture. These are:

i) Very weakly ionized gas. - When the ionization fraction is brought to an infinitesimally small value, the terms containing diffusion of ions in the general equations become negligibly small compared with other terms, and the multicomponent diffusion coefficient relevant to electron diffusion becomes that of binary diffusion of electrons into atoms (see Ref. 27). The resulting equations reduce to those for a binary mixture, in which the diffusivity is the binary diffusivity of electrons into atoms.

ii) Binary mixture of heavy particles and electrons. - Assuming that the collision cross-sections of ions are the same as the neutral atoms, the gas can be taken as a binary mixture of electrons and heavy particles, i.e. atoms and ions. The Schmidt number in this method is half that for neutral atoms and ions. If the Schmidt number for atoms and ions is unity, then this model is quite consistent with the assumption of an effective Schmidt number $\frac{1}{2}$ made in the preceding section.

iii) Binary mixture of neutral atoms and electron-ion pairs. - This gas model is used by Fay and Kemp (Ref. 18) in their analysis on ionized nitrogen. The diffusivity in this method is twice that of ions into atoms.

Thus all three models lead to binary mixture equations with slightly different definitions of diffusivity. At very low ionization level, $\phi < 0.01$ say, all three models give the same answer. In the present work, the second model is used because

i) the effective diffusivity of electron-ion pairs is not known, and

ii) the most important collision cross-section involving ion is the ion-atom cross-section, and this was found to be approximately equal to that of atom-atom collision using the method described by Hansen (Ref. 17).

For the steady flow of a binary mixture gas, the fundamental equations in the boundary layer become, neglecting the thermal and pressure diffusions (Ref. 28),

$$\rho(u\frac{\partial\phi}{\partial x}+v\frac{\partial\phi}{\partial y}) = \frac{\partial}{\partial y}(\rho D\frac{\partial\phi}{\partial y}) + \rho\frac{\phi_E-\phi}{\tau} \tag{28}$$

$$\frac{\partial}{\partial x}(\rho u r^j) + \frac{\partial}{\partial y}(\rho v r^j) = 0 \tag{29}$$

$$\rho(u\frac{\partial u}{\partial x}+v\frac{\partial u}{\partial y}) = -\frac{dp}{dx}+\frac{\partial}{\partial y}(\mu\frac{\partial u}{\partial y}) \tag{30}$$

$$\begin{aligned}\rho(u\frac{\partial h_t}{\partial x}+v\frac{\partial h_t}{\partial y}) &= \frac{\partial}{\partial y}\Big\{\frac{\lambda}{C_p}(\frac{\partial h_t}{\partial y}-h_t\frac{\partial\phi}{\partial y})+\rho D h_t\frac{\partial\phi}{\partial y}\\ &\quad +(1-\frac{1}{\sigma})\frac{\partial}{\partial y}(\frac{1}{2}u^2)\Big\} - \rho h_i\frac{\phi_E-\phi}{\tau}\end{aligned} \tag{31}$$

These equations are non-dimensionalized through the following transformation:

$$\xi = \int_0^x \rho_e\mu_e u_e r^{2j}\,dx\ , \qquad \eta = \frac{u_e r}{\sqrt{2\xi}}\int_0^y \rho\,dy$$

$$\rho u r^j = \frac{\partial\psi}{\partial y}\ , \quad \rho v r^j = -\frac{\partial\psi}{\partial x}\ , \quad \psi(\xi,\eta) = \sqrt{2\xi}\ f(\eta)$$

$$\frac{u}{u_e} = \frac{df}{d\eta} = f'\ , \quad \frac{h_t}{h_{te}} = g(\eta)\ , \quad \frac{\rho\mu}{\rho_e\mu_e} = n\ .$$

Eqs. (28) to (31) then become

$$(\frac{n}{S_c}\phi')' + f\phi' = K(\phi_E-\phi) + 2\xi(f'\frac{\partial f'}{\partial\xi} - \phi'\frac{\partial f}{\partial\xi}) \tag{32}$$

$$(nf'')' + ff'' + 2\frac{d(\log u_e)}{d(\log\xi)}(\frac{\rho_e}{\rho} - f'^2) = 2\xi(f'\frac{\partial f'}{\partial\xi} - f''\frac{\partial f}{\partial\xi}) \tag{33}$$

$$\left[\frac{n}{\sigma}\left\{g' + (L_e - 1) g \phi'\right\} + \frac{u_e^2}{h_{te}} f' f'' \left(1 - \frac{1}{\sigma}\right)\right]' + f g' =$$

$$2\xi \left(f' \frac{\partial g}{\partial \xi} - g' \frac{\partial f}{\partial \xi}\right) + \frac{h_i}{h_{te}} K(\phi_E - \phi) \qquad (34)$$

in which the prime denotes differentiation with respect to η, and K is the Damköhler number, i.e. $K = x/(u_e \tau)$ for a flat plate, or $K = \left\{2\tau (du_e/dx)_o\right\}^{-1}$ for the axisymmetric stagnation point. The boundary conditions for the Eqs. (32) to (34) are

$$\begin{aligned} &\text{at} \quad \eta = 0, \quad f = f' = 0, \quad g = g_w, \quad \phi = \phi_w \\ &\text{at} \quad \eta = \infty, \quad f' = g = 1, \quad \phi = \phi_e . \end{aligned} \qquad (35)$$

Eqs. (32) to (34) together with the boundary conditions (35) are solved for frozen and equilibrium boundary layers for both axisymmetric stagnation point and flat plate flows. For the stagnation point, Eqs. (32) to (34) automatically become similar, i.e. the RHS's identically vanish (Ref. 28). For flat plate flow, Eqs. (32) to (34) again become similar for equilibrium flows (Ref. 14). For frozen flow over a flat plate, similar solutions are sought by assuming

$$g_w = \text{constant} \quad (\text{corresponding to } T_w = 500°K), \qquad (36)$$

$$\phi_w = 0 . \qquad (37)$$

For equilibrium flows, the equation of species (32) is replaced by the Saha equation (1) and the energy equation (34) is reduced (Ref. 14) to

$$\left\{ \frac{ng'}{\sigma_E} + \frac{u_e^2}{h_{te}} f'f''\left(1 - \frac{1}{\sigma}\right) \right\}' + fg' = 0 \tag{38}$$

in which σ_E is the equilibrium Prandtl number which includes the effect of recombination.

Under the condition of Eq. (37), the equation of species (32) for a frozen flow is readily integrable when both the velocity profile function f and the viscosity-density parameter n are known. In the present paper n is approximated by

$$n = \left(\frac{T}{T_e}\right)^{-\frac{1}{2}} \tag{39}$$

which is valid as the best simple approximation for the test conditions of the present work. Because of the relatively weak dependence of the solutions on n, the choice of n is not critical. The solution of the energy equation (34) is obtained using the following iteration scheme. When Eq. (34) with RHS zero is formally integrated, it becomes

$$\frac{n_w g_w'}{\sigma_w} = \frac{\exp\left(\int_0^\infty (L_e - 1)\phi' d\eta\right) - g_w - A_1 + A_2}{\int_0^\infty \frac{\sigma}{n} \exp\left[\int_0 \left\{(L_e - 1)\phi' - f\frac{\sigma}{n}\right\} d\eta\right] d\eta} \tag{40}$$

$$A_1 = \int_0^\infty \frac{\sigma}{n} \exp\left[\int \left\{(L_e - 1)\phi' - f\frac{\sigma}{n}\right\} d\eta\right] \int \exp\left(\int f\frac{\sigma}{n} d\eta\right) d\eta \, A_3 d\eta \tag{40a}$$

$$A_2 = \frac{u_e^2}{h_{te}} \int_0^\infty \frac{\sigma}{n} \exp\left\{\int (L_e - 1)\phi' d\eta\right\} \left(1 - \frac{1}{\sigma}\right) f'f'' d\eta \tag{40b}$$

$$A_3 = (L_e - 1) f g_1 \phi' + \frac{u_e^2}{h_{te}} \frac{\sigma}{n} f f' f'' \left(1 - \frac{1}{\sigma}\right) \tag{40c}$$

$$g = \frac{\int_0 \frac{\sigma}{n} \exp\left\{\int (L_e - 1) \phi' d\eta\right\} A_4 d\eta - \frac{u_e^2}{h_{te}} \int_0 A_5 d\eta + g_w}{\exp\left\{\int_0 (L_e - 1) \phi' d\eta\right\}} \tag{41}$$

$$A_4 = \frac{\int_0 \exp\left(\int_0 f \frac{\sigma}{n} d\eta\right) A_3 d\eta}{\exp\left(\int_0 f \frac{\sigma}{n} d\eta\right)} + \frac{n_w}{\sigma_w} g'_w \exp\left(-\int_0 f \frac{\sigma}{n} d\eta\right) \tag{41a}$$

$$A_5 = \frac{u_e^2}{h_{te}} \frac{\sigma}{n} f' f'' \left(1 - \frac{1}{\sigma}\right) \exp\left(\int_0 (L_e - 1) \phi' d\eta\right) \tag{41b}$$

In Eq. (40c), the function g_1 is an approximation for g assumed or obtained from the previous integration. By substituting appropriate distributions of f, g_1, n, σ and ϕ in Eqs. (40) to (41b), the first approximation for g is obtained. The second approximation is obtained by substituting the first approximation of g into g_1, as well as improved values of f, n, σ and ϕ which are obtained by integration of the relevant equations using the first approximation of g, and so on. For the first approximation, g_1 was taken as the Blasius profile. The integration was carried out numerically using the Ferranti Mercury digital computer. The convergence of this method is so fast that for $\phi < 0.3$, the second approximation is accurate within ± 1%. A similar procedure was used for the integration of the energy equation for equilibrium flow, Eq. (38). The momentum equation (33) is integrated using the iteration scheme employing the linearized equation

$$(nf'')' + f_1 f'' + \frac{1}{2}\left(\frac{\rho_e}{\rho} - f_1'^2\right) = 0 \quad . \tag{42}$$

The profile f_1 is first assumed and then the equation is integrated in a similar manner to that in Eqs. (40) and (41) to find the next approximation of f and so on.

The result of computation is shown in Fig. 6. For a frozen boundary layer, the boundary condition Eq. (37) implies that there is surface recombination equal in magnitude to $(\rho D \partial\phi/\partial y)_w$. The effect of this recombination is to increase the heat transfer rate parameter $g_w'/(1-g_w)$ by $(h_i/h_{te})\phi_w'$. In Fig. 6, this effect is taken into account, that is, the parameter $g_w'/(1-g_w)$ for frozen flow is the sum of the value obtained from Eqs. (40) to (41b) plus $(h_i/h_{te})\phi_w'$. The pressure taken for the calculation of equilibrium ionization is 0.1 atm.

In Fig. 6, the theoretical heat transfer rates in the 'sudden freezing' boundary layers are also shown. When the boundary layer is ionically relaxing, the inner region of the boundary layer is likely to be in equilibrium while the outer region remains frozen. This is because the ionic recombination rate is a strong function of temperature and decreases very rapidly as temperature rises. The recombination in a relaxing boundary layer is bound to take place between two nearby stations η_1 and η_2, between which the flow Damköhler

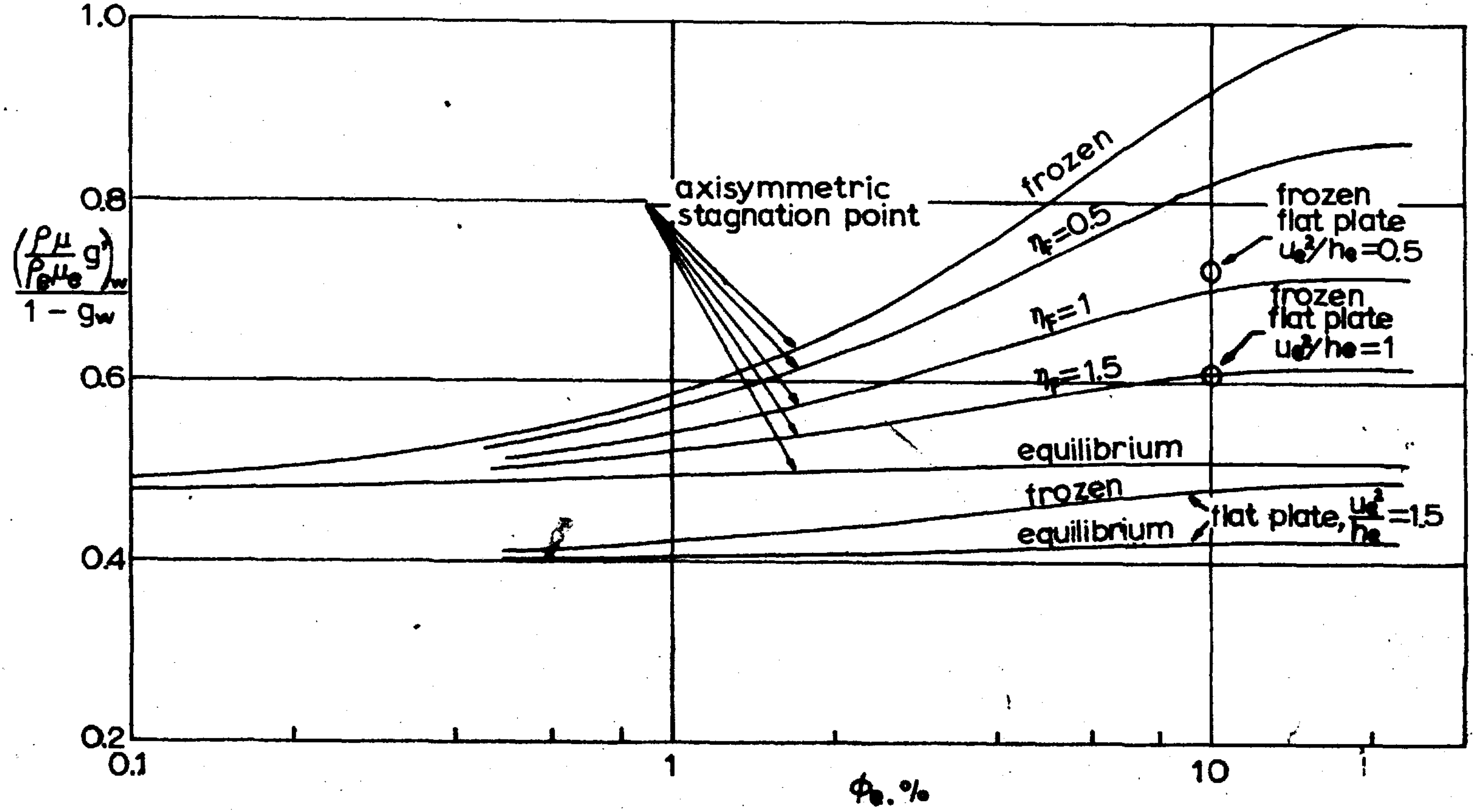

Fig. 6. Computed heat transfer parameters for ionized argon at 0.1 atm.

number falls from a large to a small number, from 10 to 0.1 say. At around $\eta_F = 1$, for instance, the band $\eta_2 - \eta_1$ within which the Damköhler number varies by the factor 100 is only about 10% of the total integrating interval $(\eta_\infty = 6)$. As a first approximation therefore, a 'sudden freezing' approximation is used to estimate the effect of ionic relaxation. This means that one determines the flow property using the equilibrium flow relations below the 'sudden freezing point' $\eta = \eta_F$ but using the frozen flow relations above it. The freezing points chosen for the computation are $\eta_F = 0.5$, 1.0 and 1.5.

The result of the computation shows that for stagnation point flow the heat transfer rate in a frozen boundary layer is much higher than in equilibrium flow, and the sudden freezing cases lie between the two extremes. In the flow over a flat plate, the effect of freezing is diminished by the increased dissipation of kinetic energy at high u_e^2/h_{te} values because of a small Prandtl number.

I-2.4.3. Heat transfer rates to a cone and a hemisphere

The theoretical results obtained in the preceding section are used to calculate the heat transfer rates to a 15° semivertex angle cone and a hemisphere, both of 0.4" diameter, placed in the nozzle flow considered in §I-2.2. at the position where $A/A_* \cong 2.7$. The heat transfer rate to the cone is obtained by integrating the local heat transfer rate

$$q = \frac{n_w g_w^0}{1-g_w} \frac{1}{\sigma_w} \left(\frac{3}{2} \rho_e \mu_e \frac{u_e}{x} \right)^{\frac{1}{2}} (h_{te} - h_w)$$

over the entire surface area of the model. The flow condition at the edge of the boundary layer necessary for the calculation is found by using the assumption

$$\frac{\rho_e u_e}{\rho_\infty u_\infty} = \text{const.}$$

which is valid only in a perfect gas. Using Eqs. (22) and (24), the total heat transfer rate to the cone becomes, neglecting the small terms,

$$Q = 5.9 \times 10^{-5} \frac{n_w g_w^0}{1-g_w} \dot{m}^{\frac{1}{2}} h_{t\infty}^{1.392} \left(1 - \frac{h_w}{h_0}\right) \quad \text{Btu/sec.} \quad (43)$$

The Reynolds number of the flow over a hemisphere of 0.4" diameter based on the freestream condition (i.e. test section condition) and body radius is around 100, and therefore the vorticity interaction behind the bow shock wave of the hemisphere may not be neglected. According to Van Dyke (Ref. 29), the vorticity interaction increases the stagnation point heat transfer rate at this Reynolds number by approximately 10%. The results of computation for the stagnation point presented in Fig. 6, therefore, are multiplied by 1.1 to obtain the heat transfer rate at the stagnation point. The local distribution of heat transfer rate over the hemisphere is not known. Since, however, the nature of the energy and species equation, Eqs. (34) and (32), is common to both ionization and dissociation (Ref. 30), the local heat transfer rate distribution is assumed to be the same as that for the dissociating gas, and hence the result of Ref. 30 is used for the calculation of local heat transfer rates. The resulting overall heat transfer rate to the hemisphere becomes, again neglecting small terms,

$$Q \doteq 8.5 \times 10^{-4} \frac{n_w g_w^0}{1-g_w} \dot{m}^{\frac{1}{2}} h_{t\infty}\left(1 - \frac{h_w}{h_{t\infty}}\right) \quad \text{Btu/sec} \quad . \tag{44}$$

I-2.5. Radiative energy transport

There are a number of mechanisms involving electronic excitation and ionization in which energy is radiated from a hot gas (see e.g. Ref. 31). For ionized argon, however, Bond (Ref. 32) takes the inelastic two-body recombination

$$A + h\nu \longleftarrow A^+ + e$$

as the main source of radiation at a pressure in the range $0.001 < p < 100$ atm, and calculated the radiated power from the above process using quantum mechanical theory. In the present symbols, his result can be written as

$$w = 1.17 \times 10^{34} \frac{p^2 \phi^2}{T^{2.5}} h\nu \qquad \text{erg cm}^{-3} \text{sec}^{-1}$$

in which h and ν are Planck's constant and the frequency of the emitted spectrum expressed in c.g.s. units. In the present work, the quantum $h\nu$ is determined simply by equating

$$h\nu = \text{ionization potential}. \qquad (45)$$

Eq. (45) is based on the assumption that the energy of ionization is completely emitted by radiation in the two-body collision. It neglects the possible transfer of kinetic energy of the electron into radiation or transfer of recombination energy into kinetic energy of the resulting neutralized atom. Since the two extraneous transfer mechanisms involve an energy of the order of only 1 ev, and since the two effects are mutually opposing, the error caused by neglecting these effects may be small. Eq. (45) is true therefore, at least to the first order, if the radiation is being emitted purely from two-body collisions, that is, assuming the frequency of the three-body recombination accompanying partial transfer of energy into radiation is negligibly small compared with that of pure two-body recombination. It is expected that Eq. (45) will be a good approximation for a flow in which three-body recombination is negligibly small, i.e. frozen ionization, or equivalently, in a flow of relatively low density in which the mean free path is too large for the three-body collision to occur significantly.

The equivalent single frequency ν that satisfies Eq. (45) is

$$\nu = 3.8 \times 10^{15} \quad \text{sec}^{-1}$$

which lies in the ultra-violet range. The actual emitted spectrum resulting from the two-body recombination, however, is not likely to be a discrete line lying in the ultra-violet range; it could be a complex of spectral lines or a continuum in the infra-red or visible regions, because the transition from a free, unbound orbit to the appropriate orbit of the atom may occur in stages.

Using the condition Eq. (45), the continuum radiated power per unit volume of ionized argon becomes

$$w = 2.93 \times 10^{16} \frac{p^2 \xi^3}{T^{2.5}} \qquad \text{watt cm}^{-3}. \tag{46}$$

The radiated power emitted from the flow at the exit of the nozzle considered in §I-2.2. was calculated using Eq. (46). The resulting radiated power values are used to compare with the measured radiative heat transfer rates in §I-3.4.

I-3. EXPERIMENT

To verify the theories given in the preceding chapter, the following measurements were taken in a plasma-jet wind tunnel ;

i) Stand-off distance of the bow shock wave from a hemisphere:

ii) Heat transfer to a hemisphere and a cone with metallic or ceramic surfaces:

iii) Radiative heat transfer.

In the following sections, the method of measurement and the results are described and discussed.

I-3.1. The wind tunnel

The wind tunnel used is a Plasmadyne AM-3 supersonic plasma-jet assembly (see Fig. 7 and also Ref. 33) which has throat and exit diameters of 0.447 and 0.836 inch respectively, and a conical semivertex angle of approximately 6 degrees followed by a parallel portion of a length of one exit diameter as shown in Fig. 1.

The arc is initiated at an open circuit voltage of either 320v or 160v; the stable operating arc voltage is maintained at about 30v. In starting at 160v open circuit, a fine copper wire was inserted between the main electrodes to form a short circuit which fuses and is blown away immediately the arc is initiated.

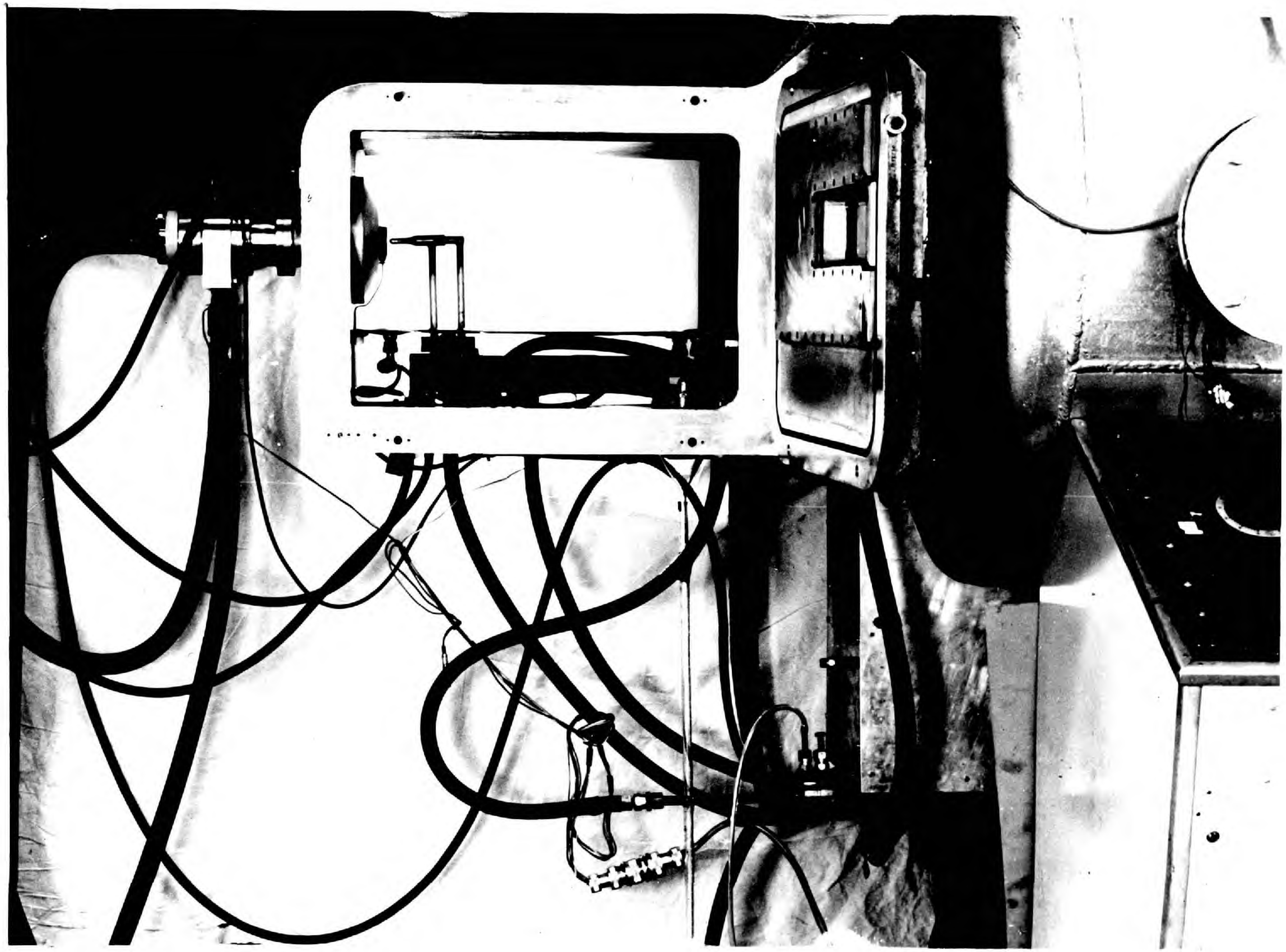

Fig. 7. General view of the head and test section of the Imperial College one-inch plasmajet wind tunnel

The gas flow rate $\dot{m}$ through the wind tunnel nozzle is metered with a float type flowmeter, and the water flow rate through the model with an orifice type flowmeter.

I-3.1.1. Observed nature of the flow

The tests with an impact pressure probe have shown that the flow is uniform at the exit of the nozzle over 50% of the exit diameter (Ref. 33). Since the diameters of the hemispherical and the conical model are about 48% of the exit diameter, and the models were placed close to the exit (Figs. 7 & 8), the effect of non-uniformity of the flow is thought to be negligible compared with other effects in the experiments with those models.

The Mach number of the tunnel flow based on the impact pressure measurement mentioned above varied from 2 to 3 depending on the degree of nonequilibrium assumed in the calculation of sonic speed, i.e. the Mach number based on the equilibrium sound speed was less than the value based on the frozen sound speed by as much as 35%. Therefore, a Mach number has not been used in any calculation in the present work. The effective nozzle exit area ratio determined from the impact pressure, on the other hand, was relatively unaffected by the degree of nonequilibrium assumed in the calculation and was approximately equal to 2.7. Throughout the work, therefore, the effective area ratio of the nozzle

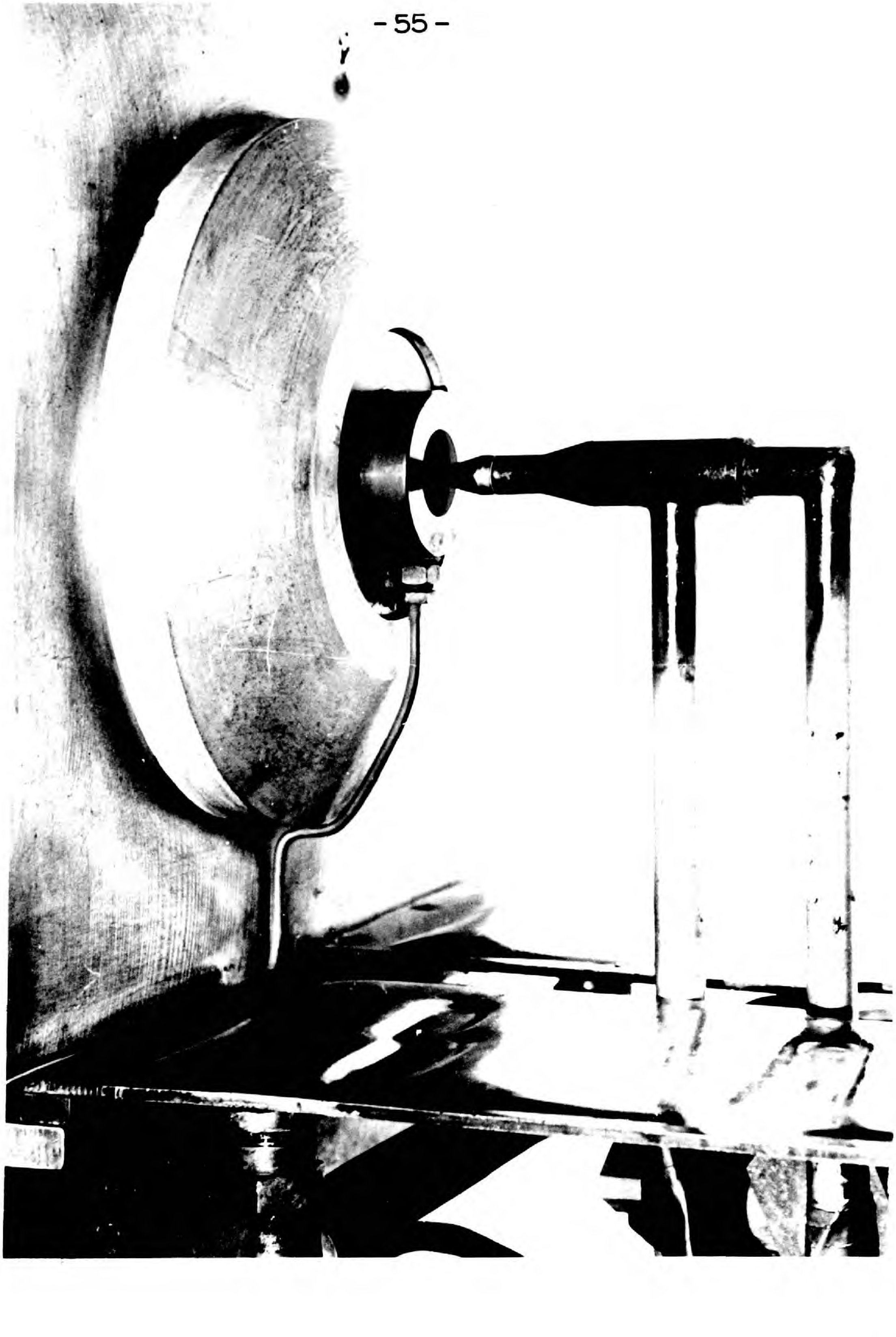

Fig. 8. Close-up view of heat transfer model(cone) in position

was taken as 2.7 .

The record of voltage and current of the main electrodes has shown that the arc is quite stable (Ref. 34). The wearing rate of the water-cooled electrodes was quite low and therefore the flow is known to be clean and steady.

I-3.1.2. Determination of flow properties

Two methods are used to determine the flow properties in the plasma-jet wind tunnel, namely, the power balance method and the 'pressure-mass flow method', which is often referred to as the mass-flow method. In the following paragraphs, the two methods are described and compared.

i) Power balance method.

In the power balance, or energy balance method, one measures the electrical power input to the arc electrodes in the heating head, E, and the heat rejected to the water cooling the electrodes, settling chamber and (in the present wind tunnel) nozzle, W. The total enthalpy, denotes by H_{tpb}, is then determined from

$$H_{tpb} = \frac{E-W}{\dot{m}} = \eta \frac{E}{\dot{m}} \qquad (47)$$

One then refers to the Mollier diagram to determine other properties in the settling chamber.

The associated experimental error in this method is

$$\left|\frac{\delta(H_{tpb})}{H_{tpb}}\right| = \frac{1}{\bar{\eta}}\left|\frac{\delta e}{e}\right| + \frac{1}{\bar{\eta}}\left|\frac{\delta I}{I}\right| + \frac{1-\bar{\eta}}{\bar{\eta}}\left|\frac{\delta \dot{M}}{\dot{M}}\right| + \frac{1-\bar{\eta}}{\bar{\eta}}\left|\frac{\delta(\Delta T)}{\Delta T}\right| + \left|\frac{\delta \dot{m}}{\dot{m}}\right| \qquad (48)$$

in which ΔT is the temperature rise in the cooling water. The factor $\bar{\eta}$ is called the head efficiency. The measured variation of the head efficiency of this plasma-jet wind tunnel is shown in Fig. 10.

In the measurement of cooling water loss W, it is desirable not to include the loss to the nozzle portion. In the present tunnel, it was impossible to separate the heat transfer to the nozzle portion from other parts because of the large bulk of copper surrounding the throat and short nozzle. Therefore, the heat transfer to the nozzle wall from the point at which $M = 0.3$ onward is calculated using the method of Ref. 35. The result shows that for the present operating condition, the heat loss to the nozzle is only 1.5% in the subsonic region and 1.5% in the supersonic portion of the nozzle of the total electrical power input to the head. For simplicity, therefore, the loss to the nozzle wall is neglected in the calculation of enthalpy level H_{tpb}.

ii) Pressure-mass flow method.

A detailed calculation of displacement thickness at the throat was carried out using the method of Cohen and Reshotko (Ref. 11) to determine the effective throat area A_*. The calculation shows that the displacement thickness at the throat

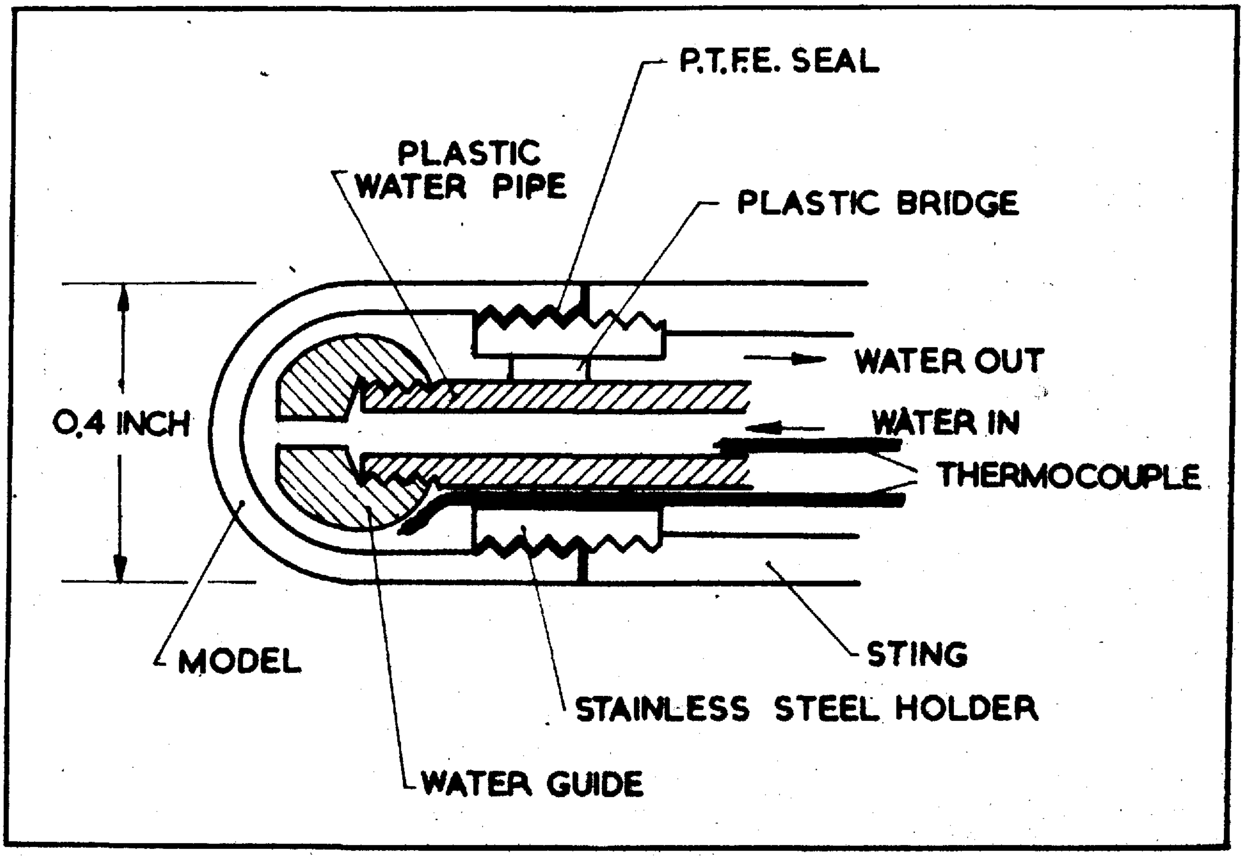

FIG. 9. SKETCH OF CALORIMETER-MODEL

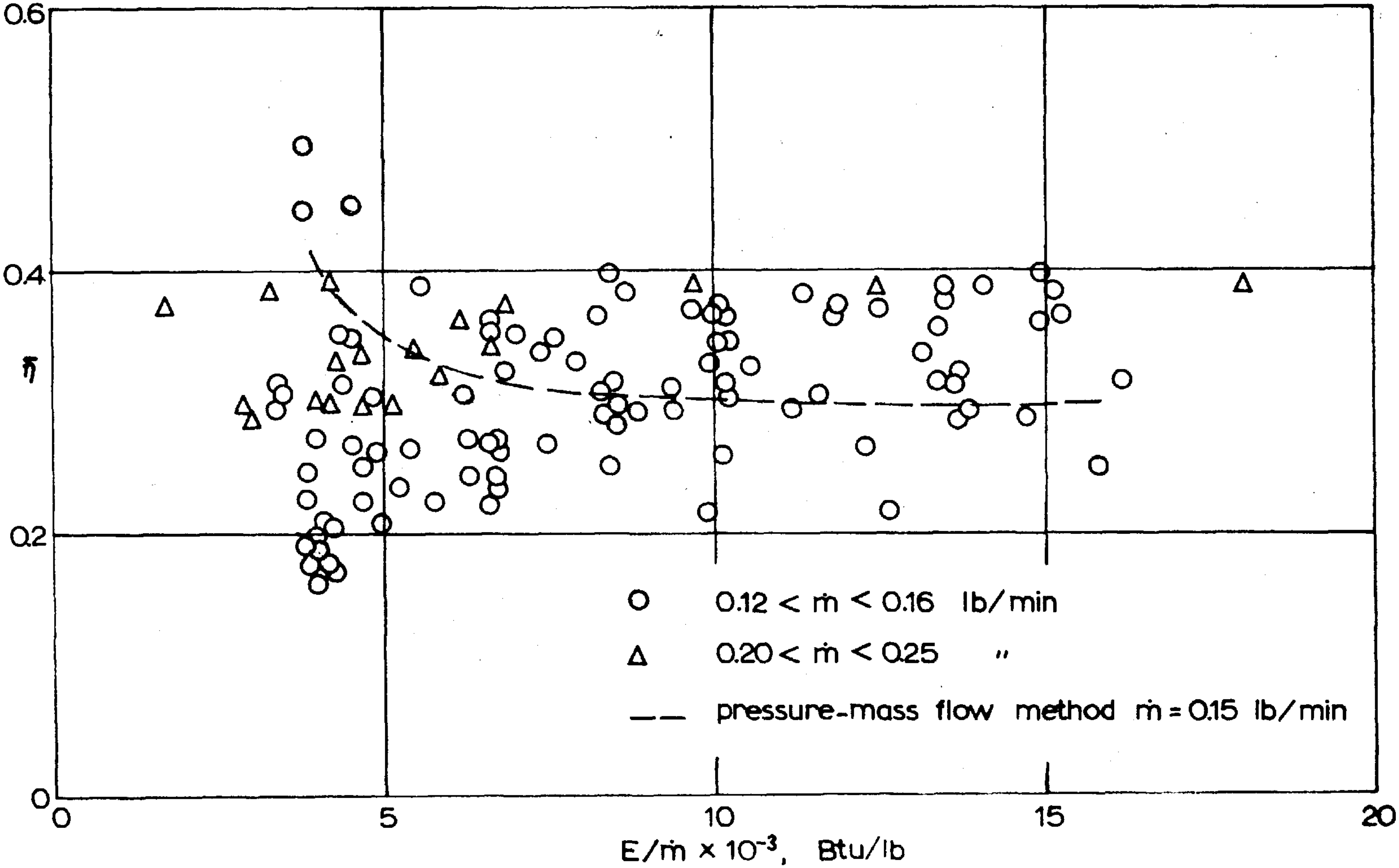

Fig. 10. Tunnel head efficiency for argon

is negative and can be expressed approximately as

$$\frac{\delta_*}{r_*} = -0.02 \left\{ \frac{0.3}{\dot{m}\,(\mathrm{lb/min})} \right\}^{\frac{1}{2}}$$

where δ_* and r_* are the displacement thickness and the radius of nozzle at the throat, respectively. Combining the above relation with Eqs. (22) and (24), the expression for the frozen enthalpy becomes

$$h_{tmf} = 1045 \left\{ 1 + 0.08 \left(\frac{0.3}{\dot{m}}\right) \right\} \left(\frac{p_o}{\dot{m}}\right)^2 \quad \mathrm{Btu/lb} \qquad (49)$$

The Mollier diagram necessary to determine other properties is given in Fig. 11 for the range of interest, which is a modification of that contained in Ref. 36. The maximum experimental error in the determination of frozen enthalpy in this method is simply

$$\left| \frac{\delta h_{tmf}}{h_{tmf}} \right| = 2 \left| \frac{\delta p_o}{p_o} \right| + 2 \left| \frac{\delta (\dot{m}/A_*)}{\dot{m}/A_*} \right| \qquad (50)$$

The tunnel head efficiencies calculated using the above two methods are compared in Fig. 10. As seen from the figure, the two methods agree to within the possible experimental accuracy. The relatively wider scattering of efficiency values obtained from the power balance method is believed to be due to the greater error associated with the form of the Eq. (48). For example, the experimental errors of 1.5% in volt- and ammeter readings, 1 % in thermocouple emf, water flow rate, gas flowmeter, gas pressure and settling chamber pressure readings and 2% in reading the chart gives

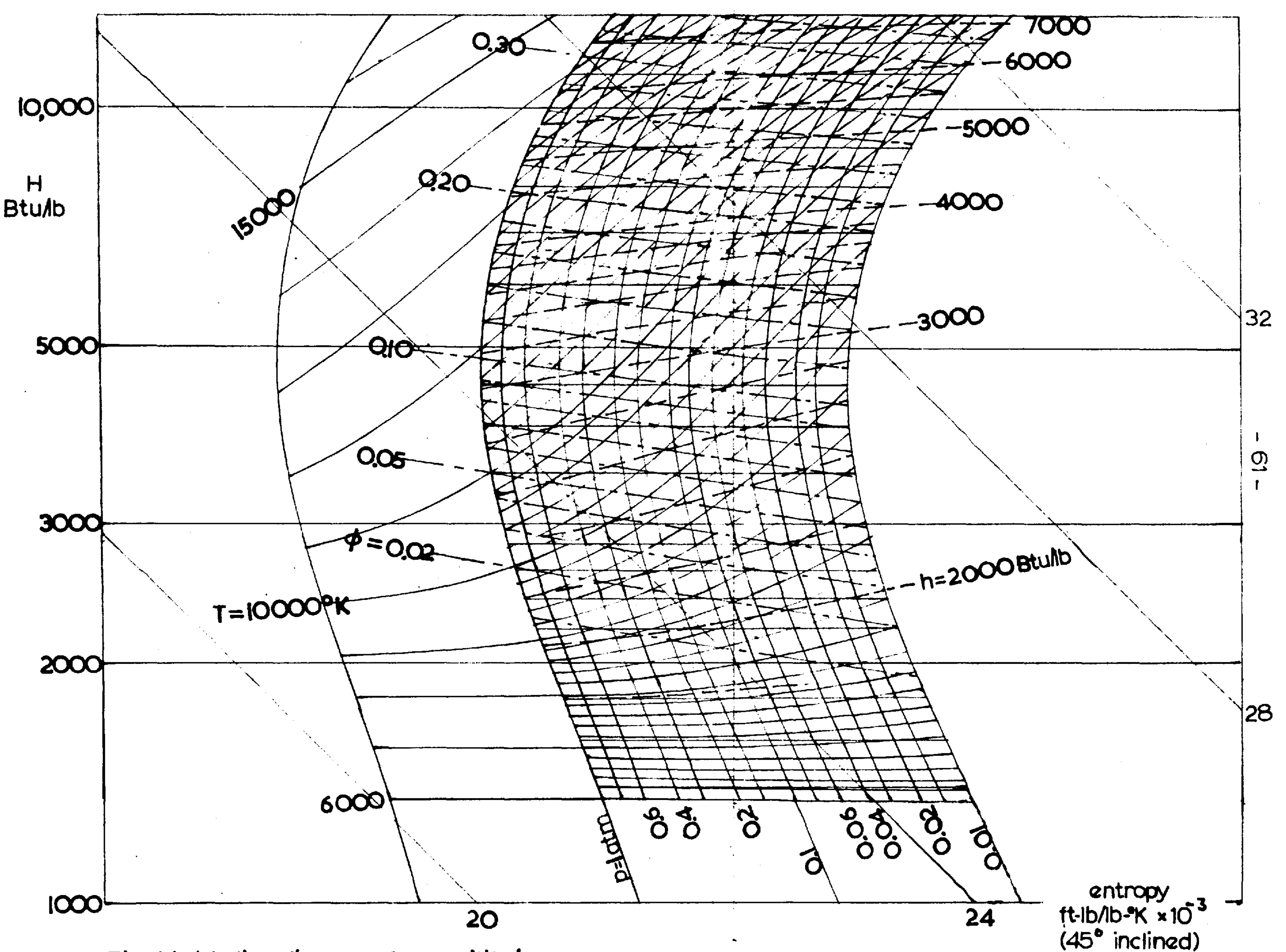

Fig. 11. Mollier diagram for equilibrium argon

in the determination of H_{tpb} and H_{tmf} resultant errors of 16% and 8% respectively under typical operational conditions. In the present investigation, therefore, the mass flow method was used to determine the flow conditions.

The true controlling factors in a plasma-jet wind tunnel are the electrical power input E and gas mass flow rate $\mathring{m}$. The most convenient method of plotting the experimental results directly is to plot them against the electrical power input per unit mass $E/\mathring{m}$ at different mass flow rate $\mathring{m}$, because the factor $E/\mathring{m}$ is roughly the indication of enthalpy level of the flow. If the tunnel head efficiency $\bar{\eta}$ is a function only of flow enthalpy H_t, the input power $E/\mathring{m}$ is a direct indication of enthalpy level.

The variation of the factor $(p_o/\mathring{m})^2$, which is a direct indication of frozen enthalpy (see Eq. (49)) and hence H_t, with the power input $E/\mathring{m}$ is shown in Fig. 12. Fig. 12 shows that the factor $(p_o/\mathring{m})^2$ is quite well correlated with the input power $E/\mathring{m}$, implying that the measurements of $(p_o/\mathring{m})^2$ and $E/\mathring{m}$ are both accurate. Fig. 12 also shows that a considerable portion of the input electrical energy is consumed in ionization, for if there is no energy absorption due to ionization, $(p_o/\mathring{m})^2$ must vary approximately linearly with $E/\mathring{m}$.

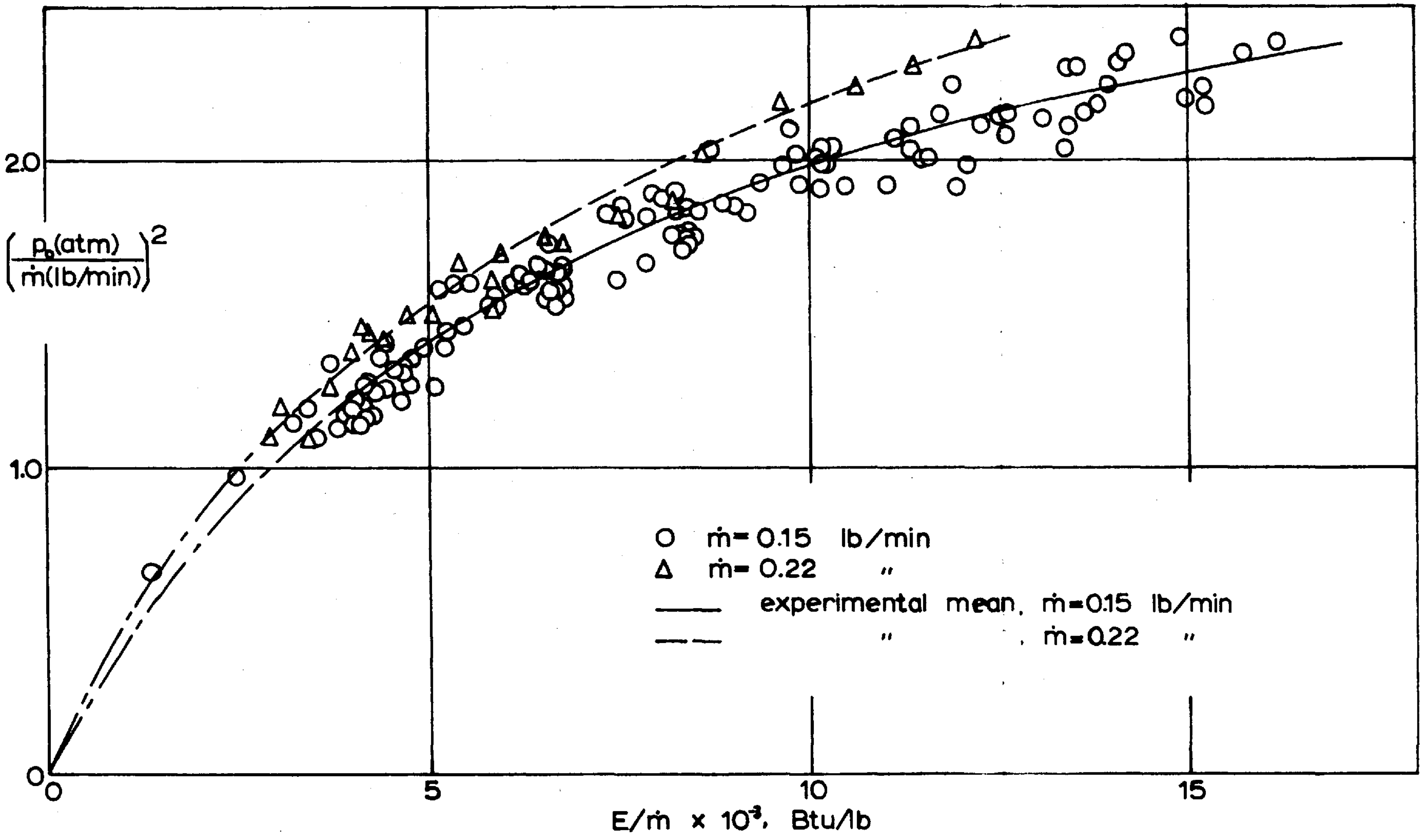

Fig. 12. Relationship between $(p_o/\dot{m})^2$ and $E/\dot{m}$ for argon

I-3.1.3. Flow condition

The theoretical calculations in §I-2.2. were performed for the typical operating flow conditions of the plasma-jet wind tunnel used. The first crucial assumption made in the analysis in §I-2.2. was that thermo-chemical equilibrium is established in the settling chamber. It is not clear, (from the results of the basic flow measurements presented in Figs. 11 and 12 only), whether this assumption is justificiable in the wind tunnel used. Since, however, the enthalpy levels calculated using the power balance method and pressure-mass flow method are approximately equal to each other (within ± 10% of mean), it is inferable that the departure from equilibrium in the settling chamber is small, if any. (This point is discussed in detail in §I-4.1.) The other assumption used in §I-2.2. was the assumption of adiabatic flow. The deviation from adiabatic flow in the tunnel was calculated using the experimental results in §I-3.4. and is seen to be very small (see §I-3.4.). The results obtained in §I-2.2. are therefore directly applicable at least to the first order.

The typical operating conditions and the characteristic constants for each condition are presented in Table 1. The values in the table explain the pertinence of the basic formulae used in the analysis in §I-2.2., i.e.; i) the maximum temperature in the tunnel, i.e. the settling chamber value, is not greater than 12,000°K and hence the equilibrium electron temperature

Table 1. Typical operating conditions and characteristic constants of wind tunnel

	unit	1	2	3
gas flow rate $\mathring{m}$	lb/min	0.15	0.15	0.15
head power input E	kw	16.9	27.7	35.1
settling chamber pressure P_o	atm	0.191	0.215	0.225
head efficiency $\bar{\eta}$	%	28	31	34
total enthalpy H_t	Btu/lb	1850	3250	4500
frozen enthalpy h_{t0}	"	1770	2430	2950
ionization fraction ϕ_0	%	0.05	5	9.5
settling chamber temperature T_0	°K	8000	10000	11000
exit temperature equil. $T_{\infty E}$	"	2200	4300	8500
exit temperature frozen $T_{\infty F}$	"	2100	2690	3000
exit temperature relax. T_∞	"	2100	3300	4600
exit velocity v_∞	fps	4200	4700	5300
exit density $\rho_\infty \times 10^4$	amagat	9.2	7.9	7.2
electron density $N_{e\infty} \times 10^{-14}$	cm^{-3}	0.12	8.0	13
exit Reynolds number per inch		600	420	340
Reynolds no. for sphere model		120	84	68
mean free path in test section (hard sphere approx.)	mm	0.073	0.083	0.093
mean free path in shock layer (hard sphere approx.)	mm	0.024	0.028	0.031
Debye shielding distance in test section $\times 10^5$	mm	93	14	8.6

is almost equal to the atom temperature (Eq. (4)); ii) the flow temperature is higher than 2000°K and the electron density is greater than 10^{13} for $\phi > 0.0005$, and therefore the recombination rate constant of Hinnov and Hirschberg (Eq. (8)) can be used; iii) the mean free path is still very small and so the Maxwell velocity distribution can be established within the neutral atoms and therefore the electron temperature relaxation equation of Spitzer (Eq. (5)) can be used.

In Fig. 13, the temperatures of the flow at the nozzle exit as determined by the various methods are shown. As seen from Fig. 13, the exit flow temperature is controlled sensitively by the ionic recombination process. The result of spectroscopic measurements carried out by Adcock and Plumtree (Ref. 37) agrees better with the calculated electron temperature than the atom temperature.

I-3.2. Shock wave stand-off distance measurement

Illumination pictures of the shock layer over the hemisphere model were taken in the plasma-jet wind tunnel. The camera used for this purpose was D. Shackman & Sons Mk 3 Auto-Camera fitted with a 125mm telephoto lens. The films used were the low speed, fine grain, 35mm Pan F films. The exposure time and aperture were varied from 1/200-f22 to 1/25-f5.6. At high enthalpy levels, the uniform neutral

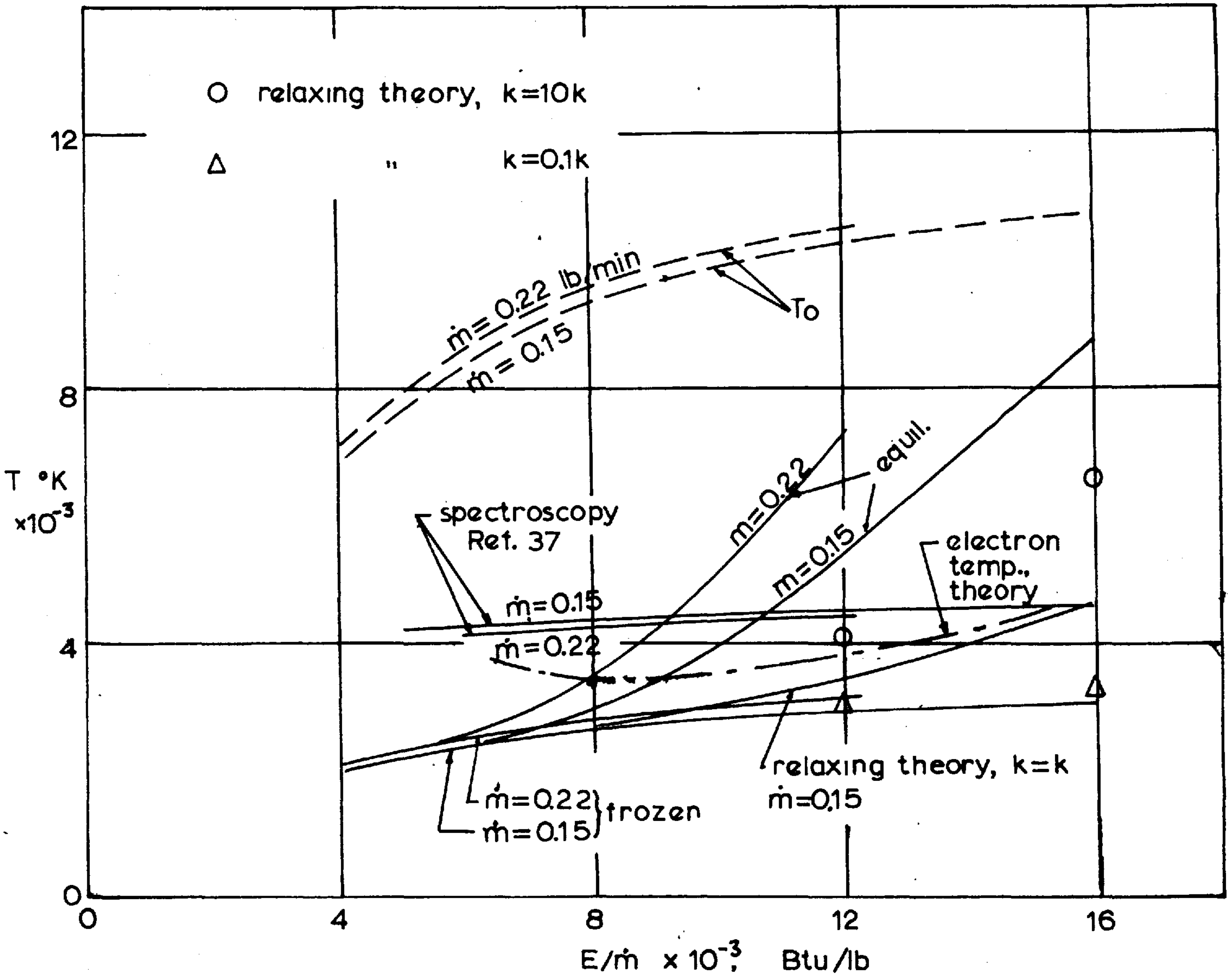

Fig. 13. Comparison of wind tunnel exit temperatures in argon obtained by various methods

filters of filtering ratios 2 or 4 were used to reduce the light amount. A typical picture of the shock layer is shown in Fig. 14. The micro-photo-densitometer trace of the negative is shown in Fig. 15. The densitometer trace shown in Fig. 15 is taken by scanning the negative of the picture across the stagnation region shock layer by a micro-photo-densitometer. The abscissa in the densitograph, Fig. 15, is the distance along the stagnation streamline, and the ordinate represents the brightness of the gas at a point on the stagnation streamline which is related to the brightness by a nonlinear function (see e.g. Ref. 37). The shock wave positions are determined either by extrapolating the trace of the densitograph as in Fig. 15 or by measuring the distance directly from the negative using a traversing microscope. The shock wave stand-off distances measured in this way at different enthalpy levels are compared with the theoretical values derived in §I-2.3. in Fig. 3.

Each vertical segment in Fig. 3 represents a measured value, the centre representing the mean value of the readings taken from the densitograph and from the direct reading, and the length representing approximately the range of uncertainty in reading arising from the diffuse nature of the shock front (see Fig. 15).

As seen from Fig. 3, the measured stand-off distances agree better with the theoretical calculations assuming a frozen flow behind the bow shock wave. There is, however, a weak

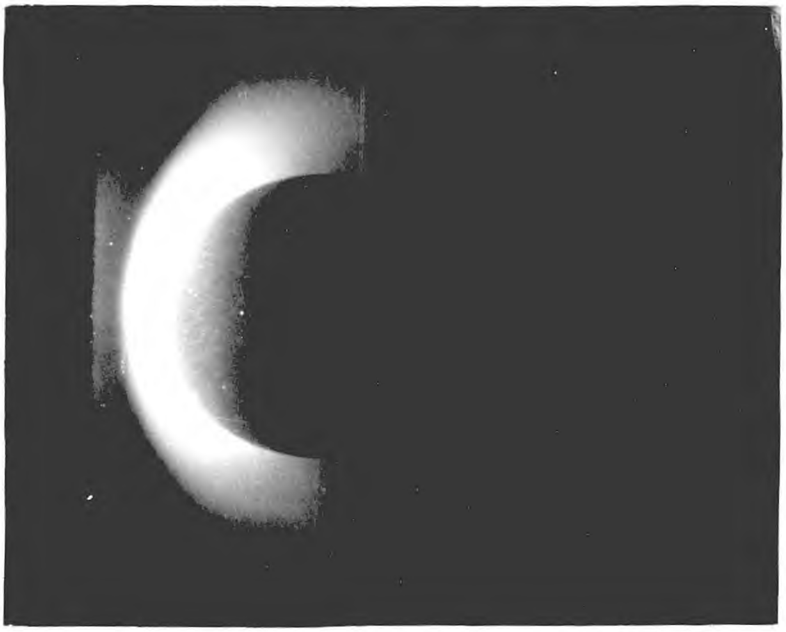

Fig. 14. Typical picture of detached shock wave in argon. $H_t = 1850$ Btu/lb, $\phi_0 = 0$, $\rho_\infty = 0.0014$ amagat

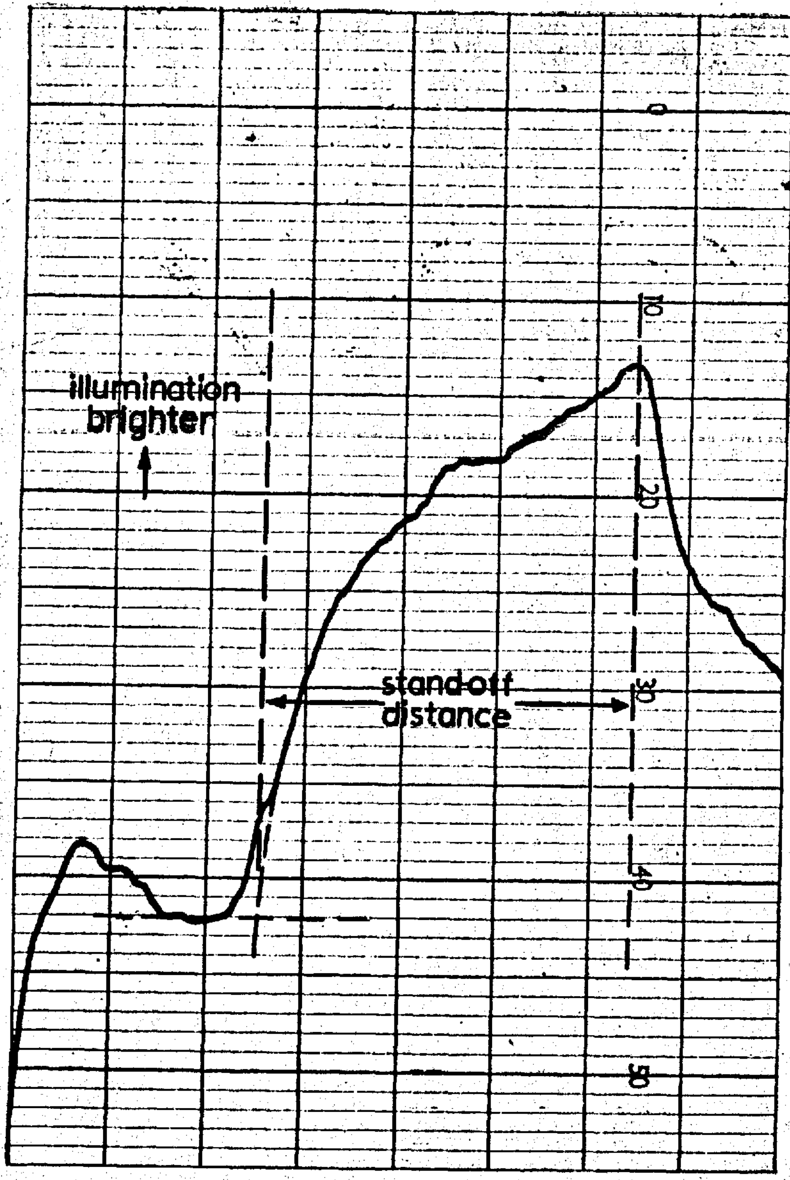

Fig.15. Typical microphotodensitometer trace across stagnation region shock layer and the method of determining shock wave stand off distance, argon

tendency for the shock stand-off distance to decrease at high ionization levels, showing that there is a weak recombination behind the bow shock wave. The trend indicated by the measured results therefore agrees with that expected from the predicted relaxation in the nozzle (see §I-2.3.) The flow Damköhler number behind the shock calculated using the rate constant of Petschek and Byron (Ref. 5) is small but not negligible and hence a weak recombination is expected behind the shock wave.

I-3.3. Heat transfer measurements, hemisphere and cone

The heat transfer models used are a hemisphere-cylinder and a 15° semiangle cone both of 0.4" diameter, and are water-cooled inside (see Figs. 8 & 9). The total heat transfer rate to the hemispherical or conical portion of the model is determined by measuring the difference between the temperature of cooling water going into and coming out from the test portion. The thermocouples used are of a chromel-alumel type (Thermocoax) sheathed wire having a sensitivity of 41μv/deg. C. Both junctions were directly exposed to the cooling water. The resistance of the electrical leak path through these exposed portions is found to be of the order of 10kΩ and is therefore neglected in the calculation of tempera-

---

An abridged version of this section, along with the theoretical work in §I-2.4., is published as Ref. 26.

ture rise. The two thermocouples are connected in an electrically opposed configuration so as to give the difference in emf directly, which is read by either a bridge-type, high precision potentiometer or an amplifier-meter.

Copper and ceramic surfaces were used on the models, the ceramic coating being a Ferro 571 coating, consisting mainly of boro-silicate ceramic. The process of coating is as follows: i) degrease the surface and blast-clean with a non-metallic oxide, ii) mix the coating compound, iii) grind the compound finely, iv) mix the compound with water and electrolytes, v) cold spray, vi) fire at 820°C for 3 minutes, and then vii) air-cool. The coating was developed and applied to the models by the Ferro-Solaramic group of Ferro-Enamels Ltd. The thickness of the coating was either 0.0010" or 0.0030".

The water flow rate through the models was kept between 0.014 and 0.04 lb/sec, by keeping the supply pressure up to about 10 psig. With this water flow rate, the temperature rise in the cooling water measured by the thermocouples was between 3°C and 30°C.

It was verified, using an oscilloscope, that the temperature reading of the thermocouples installed in the water-cooled calorimeter had a rise time of about 3 sec; that there was a random temperature fluctuation of about 3%.

The heat transfer rates from the ionized argon gas to the models described above were measured in the plasma-jet wind tunnel for the following range of conditions;

$0.14 < \dot{m} < 0.3$ lb/min.

$10 < E < 50$ kw,

$0.18 < p_0 < 0.45$ atm.

$5 \times 10^{-4} < \rho_\infty < 1.5 \times 10^{-3}$ amagat.

The results of the test are presented in Fig. 16.

The theoretical values shown in Fig. 16 for comparison with the experimental results are taken from Eqs. (43) and (44), that is, considering the convective heat transfer alone. This is done because the radiative heat transfer to the models is very small compared with the convective heat transfer. The effect of radiative energy transport to the tested models was estimated using the measured radiative heat transfer rates (see the following section). The radiating cap over the hemisphere was assumed to have a mean uniform density of 3 times the freestream value and the conical shell over the cone surrounded by the conical shock surface to have a density twice the freestream value. The ionization fraction in these radiating caps was assumed to be equal to the settling chamber value. The radiant energy was assumed to be emitted from these radiating elements only, i.e. the effect of distant radiation was neglected. The gas was assumed to be perfectly transparent. Half of the energy radiated by these elements was assumed to be absorbed by the model, which is true in the limiting case of an infinitesimally thin shock layer. The result shows that the radiative heat transfer to the tested

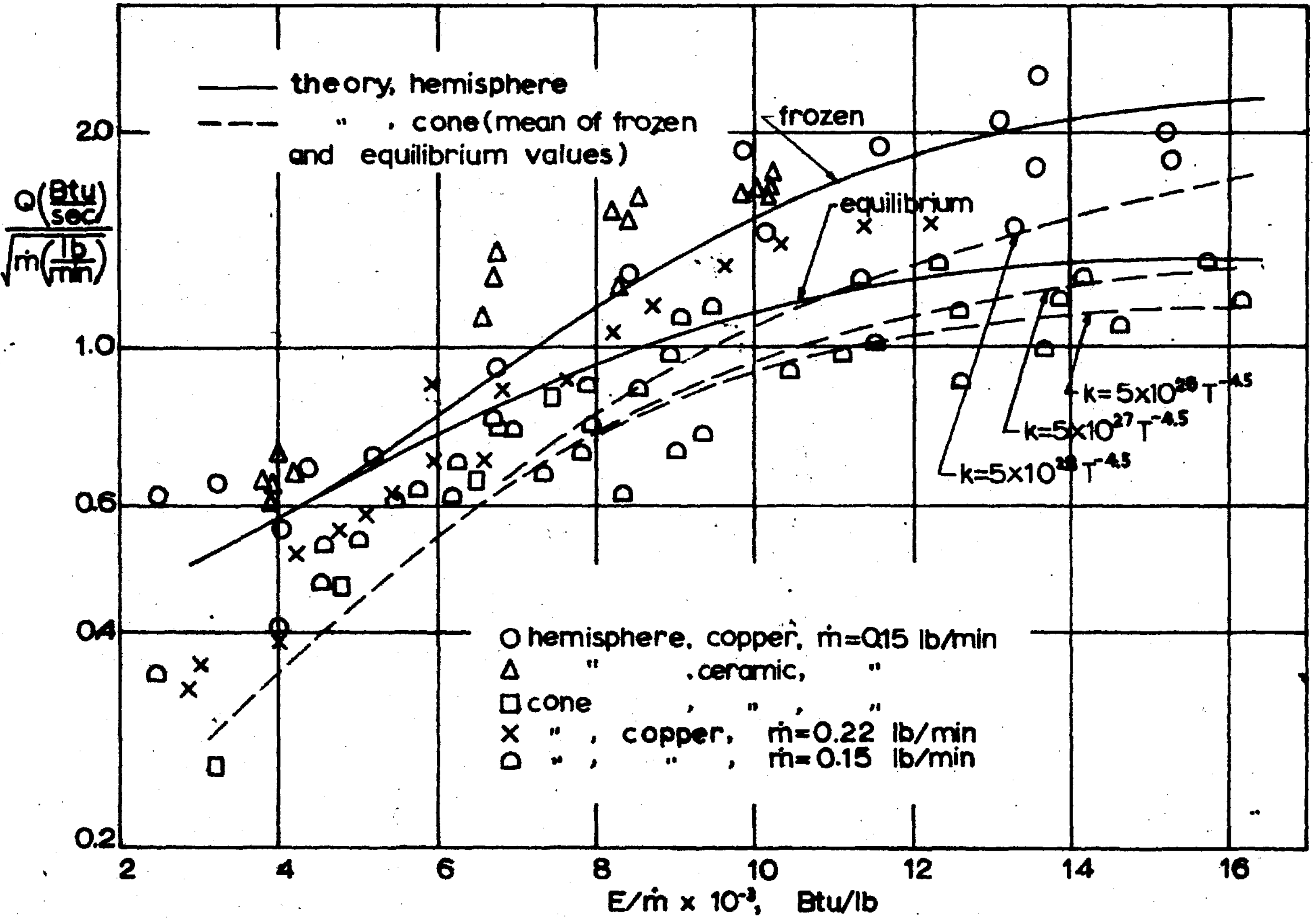

Fig. 16. Experimental results of heat transfer in ionized argon.

models is less than 2 % of the total heat transfer. The radiative heat transfer is neglected therefore in the calculation of heat transfer rates.

In the calculation of the theoretical heat transfer rates to the cone, the mean of the equilibrium and frozen values was used. The surface temperature was taken as the average value over the entire model surface, which was calculated using the known wall thickness of the model and the thermal conductivity of the material,

copper: 7.7×10^{-2} Btu ft^{-1} sec^{-1} ^{o}K^{-1}

ceramic coated copper: 2.5×10^{-2} " .

The average surface temperature was calculated to be about 3.5 % of the total temperature of the flow and hence the error caused by the averaging is thought to be small (see Fig. 12, Part II).

As seen from Fig. 16, no significant difference can be found between the heat transfer rates to the copper and ceramic surfaces. Since the effect of surface temperature is negligible, this means that either

i) all the surfaces have very similar catalytic reaction rates for ionic recombination,

ii) the boundary layer is ionically in equilibrium, at least in the vicinity of the surface, or

iii) the surfaces have very different catalytic reaction rates, but they are all greater than a certain limit (see e.g.

Ref. 38).

Since it is unlikely that the metallic and ceramic surfaces have a similar catalytic effect on ionic recombination, the possibility for case i) is very weak. From the present experiment, it cannot be decided which of the cases ii) or iii) is true. From the physical point of view, however, the cases ii) and iii) are not much different from each other. Microscopically, for a catalytic surface, the interface between the model and gas is of finite thickness and there is deep interpenetration between the media and the gas particles near the wall are trapped firmly so encouraging them to recombine. In the ionic recombination process, the low temperature is the main cause of recombination in this region, because the recombination rate is very large at low temperatures as indicated by the form of rate constant (Eq. (8)). The apparent surface ionic recombination is nothing but the gas phase recombination accelerated by the low temperature near the wall. In this respect, case iii) is a limiting case of case ii).

The measured heat transfer rates to the cone model agree with the theoretical values based on ionic recombination rates of $k = 5 \times 10^{27} T^{-4.5}$ within the accuracy of the experiment. The measured results are obviously lower than the theoretical values based on a rate constant ten times the value mentioned above, i.e. $k = 10k$, but the scattering of the experimental data is too large to determine whether they agree better with the theoretical values using the assumed true value of k or with those values using 0.1 k. The results of this measurement, therefore, partly support the rate constant of Hinnov and Hirschberg (Ref. 8) and show that it is not greater than the value obtained by them.

The heat transfer to the hemispherical model agrees better with the theoretical values of frozen boundary layer flow with fully catalytic surface recombination than with equilibrium boundary layer flow, showing that the boundary layer is ionically frozen. To check whether the result is compatible with the local Damköhler number within the boundary layer, the local Damköhler number K in Eq. (32) was calculated for the boundary layer flow at the stagnation point. The result shows that K is nearly zero within the boundary layer except at the immediate vicinity of the wall, that is, the freezing point is quite near the wall. Thus theory and experiment both support the conclusion that the boundary layer is ionically frozen and the cold wall acts like an infinitely catalytic wall under the present testing condition.

In order to compare the present result with equivalent data for air, the heat transfer rate at the stagnation point is plotted in Fig. 17 with the equivalent flight speed as abscissa. The equivalent flight speed was chosen to give the same enthalpy fraction, i.e. the ratio of energy consumed in ionization to the total energy, as in flight. N_u and R_n in Fig. 17 are the Nusselt number and Reynolds number pertinent to stagnation point flow (see Ref. 20).

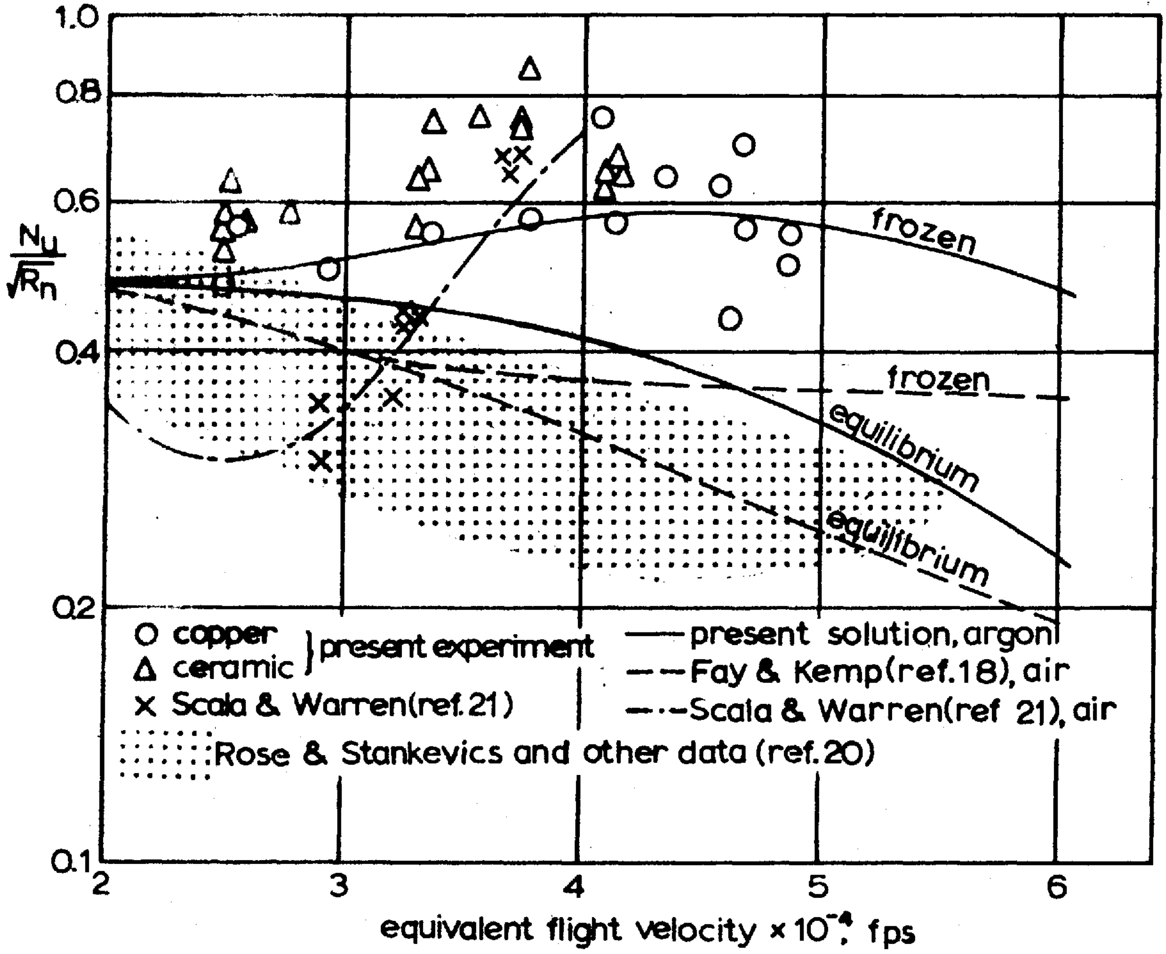

Fig. 17. Comparison of results with other data, stagnation point heat transfer from ionized argon.

The difference between the experimental results presented here and those summarized in Ref. 20 can be attributed to the difference in the testing condition. In Ref. 20, the flow was in equilibrium, whereas here, the flow is nearly frozen. The conditions relevant to the work of Scala and Warren (Ref. 21) are not known, but from the above, it seems that the flow must have been frozen. The disagreement between the results of Scala and Warren and the theory of Fay and Kemp (Ref. 18) for frozen flow remains unresolved. Fig. 16 also shows that the difference between the theoretical heat transfer rates from a frozen and equilibrium boundary layer in an argon flow is more severe than in air. This might arise because the electron-atom collision cross-section in argon is smaller than in air and hence the frozen Prandtl number decreases more rapidly as the ionization fraction increases.

I-3.4. Radiation from ionized argon

The radiation heat transfer from the exit flow of the wind tunnel was measured using a bolometer. The instrument used is a differential type black-body bolometer cased in a PTFE housing (see Figs. 18 & 19). The sensing elements are two brass foils of 3/16" diameter and 0.002" thick placed $\frac{1}{8}$" apart. The elements are hung by three equally spaced BS #42 copper wires attached to the inside of a length of $\frac{1}{2}$" bore PTFE tubing. Two elements are connected by a one

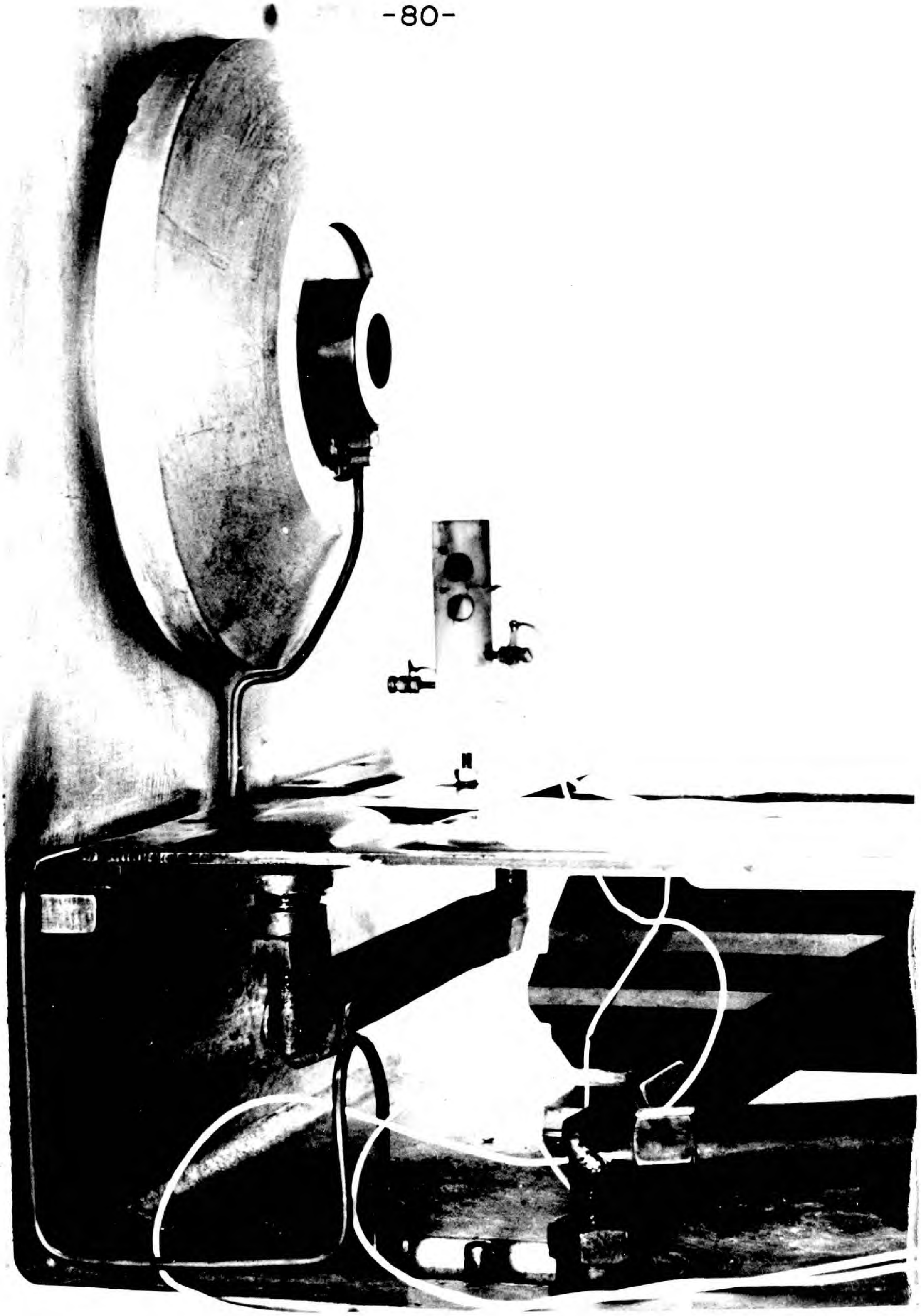

Fig. 18. Differential bolometer in testing position

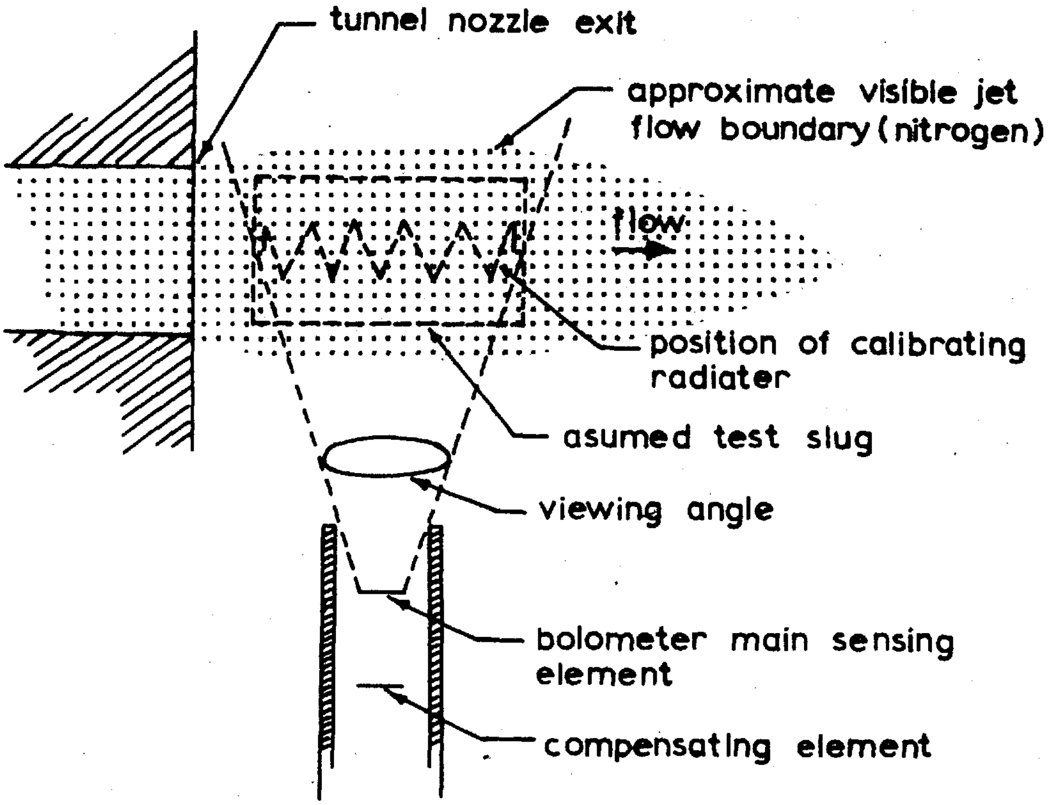

Fig. 19. Sketch of testing condition of radiative heat transfer (original scale).

inch length of BS #42 constantan wire at each centre. Only one sensing element, i.e. the element directly facing the radiation, is blackened by lampblack. Six large holes are drilled through the wall of the housing to permit ready access of the surrounding gases to all faces of the elements. The differential temperature of the two elements is measured by the difference of emf between the two junctions (i.e. the junctions between the constantan wire and the two foils). The bolometer is placed so that the main receiving element may pick up most of the direct radiation (see Fig. 19). With this arrangement, the convective heat transfer to both elements annul each other and only the difference in radiative heat transfer is detected.

The bolometer is calibrated by exposing it to an electrical heating element under the same vacuum conditions as in test, i.e. 5 torr. The electrical heater is a cylindrical coil of $\frac{1}{8}$" diameter and 1.3" long and was placed exactly in the position of the measured gas stream (see Fig. 19). To determine the effect of ambient pressure the calibration was repeated at 0.2 torr. The result of the calibration is shown in Fig. 20, and it is seen that the sensitivity increases as the surrounding gas density decreases. The response time of the bolometer to the changing radiation is about 1 min at 5 torr and 3 min at 0.2 torr.

The bolometer is placed at right angles to the axis of the jet as shown in Figs. 18 and 19. The results of the test

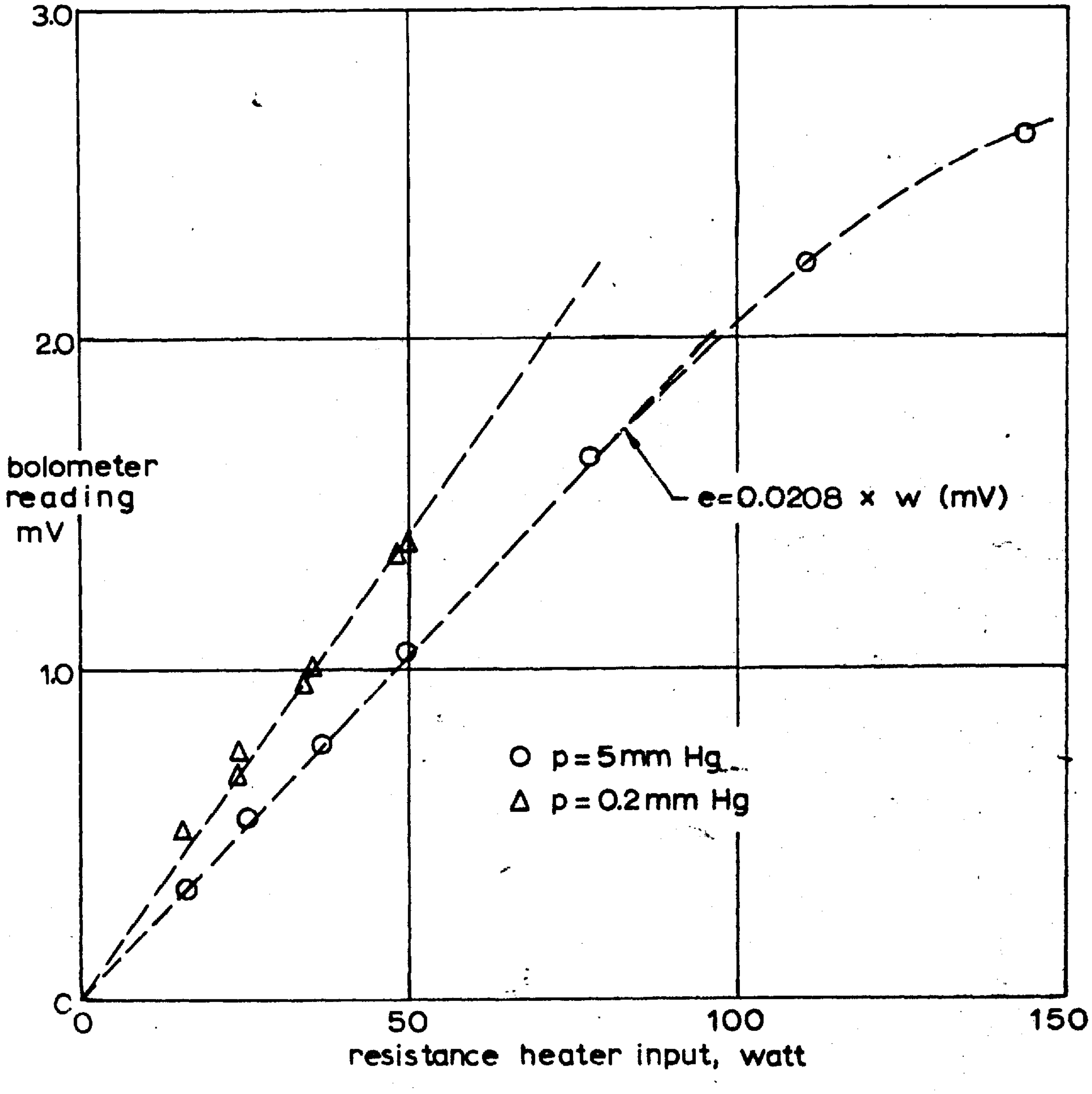

Fig. 20. Calibration of bolometer

are presented in Fig. 21. Shown also in Fig. 21 are the theoretical values calculated using Eq. (46) which requires use of the values obtained from computer solutions of the nozzle flow properties shown in Figs. 2 and 13. The figure shows that the theoretical values agree with the experimental results within approximately 30 % at moderate ionization levels $0.04 < \phi < 0.1$, but are several orders of magnitude smaller at low ionization levels $\phi < 0.01$. The severe departure of the experimental results from the theoretical values at low power level suggests that there is over-ionization in the exit flow, i.e. the ionization level is higher than that predicted by the theory assuming equilibrium in the setting chamber. One possibility is that electro-magnetic fields may increase the ionization level in the plasma-jet wind tunnel both in the settling chamber and the nozzle. The presence of over-ionization may also partly account for the departure of the experimental heat transfer results in the case of the hemisphere from the theoretical values at low ionization levels (see §I-3.3.).

The largest source of error in this measurement is the possible inaccuracy of the bolometer calibration. Even if the calibration of the bolometer is carried out at the same ambient pressure as during the experiments, the absorptive and convective properties of the ambient gas cannot be simulated properly in the calibration. For example, when the calibration curve obtained at 0.2 torr is used, the experimental results

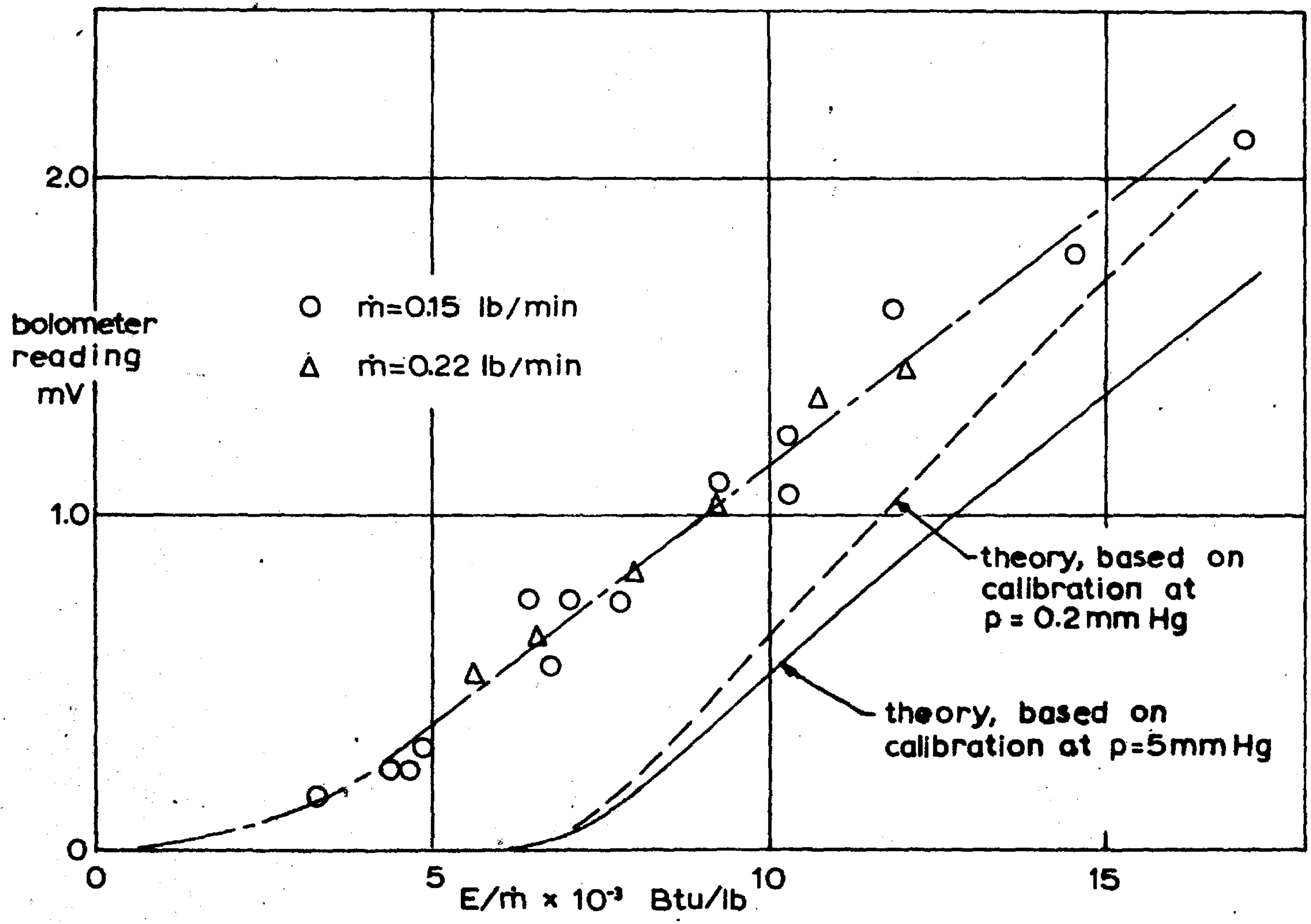

Fig. 21. Radiative heat transfer from argon.

of Fig. 21 come very close to the theoretical values at high enthalpy levels (see Fig. 21). Since a pressure of 0.2 torr represents an effective vacuum (note that under these conditions, the convective heat transfer rate is proportional to density), the true values would lie between the values given by the two calibration curves.

The departure from the adiabatic condition which is due to the radiative energy transport in the nozzle flow, is estimated by comparing the total amount of radiation loss to the total enthalpy. The total amount of energy loss per unit volume is the time integration of radiation loss, i.e. $\int w dt$. For a rough comparison, the energy loss w in the integrand is taken as the maximum value of the energy loss in the system, i.e. the settling chamber value, and the time interval as the total mechanical transit time through the nozzle. Thus the ratio

$$\frac{w_o \Delta t}{H_t}$$

was calculated for the relevant operating conditions. The result shows that the energy loss which is due to radiation is less than 1% of the total enthalpy for all testing conditions. The assumption of adiabatic flow used in §I-2.1. and §I-2.2. is therefore sufficiently accurate for the purpose of the present investigation.

I-4. DISCUSSION

I-4.1. Plasma-jet wind tunnel flow

The crucial assumption made about the nature of the flow in the Imperial College one-inch plasma-jet wind tunnel flow is that thermo-chemical equilibrium is established in the settling chamber. The characteristic Damköhler numbers for ionic relaxation as determined by Eqs. (7) and (8) are of the order of 1 and 10 for the settling chamber. (The Damköhler number for electron temperature equilibration is of the order of 100.) Ref. 39 reports that the flow may not reach equilibrium even if the characteristic Damköhler number for the settling chamber is considerably larger than unity. The results of the radiative and convective heat transfer rate measurements show the presence of excess electrons, which can only be explained by the lack of equilibrium in the settling chamber. Thus the assumption of ionic equilibrium in the settling chamber seems to be good only for relatively high ionization levels.

Ref. 39 considered the effect of Mach number change which is due to boundary layer growth near the throat and concluded that the sonic speed is attained in the convergent portion of the nozzle and that the effective sonic throat is larger than the geometrical throat area. The present work simply calculates the boundary layer displacement thickness and concludes that the effective throat area is larger than the geometrical throat area. Ref. 39 and the present work cannot be compared directly because the definitions of sound speed used are different, but both agree that the effective throat area is larger than the geometrical throat area. The real-gas effect on the boundary layer flow in the convergent portion of a wind tunnel is more complicated than the above mentioned two methods visualize, and therefore neither of the two methods is sufficiently accurate. A detailed study of this subject would be desirable in the future.

The two methods of flow determination, i.e. the power balance method and the pressure-mass flow method, agree with each other within the experimental error (± 20%) when the effective throat area change is accounted for. This is in contrast with the work of Ref. 40 which reports a large difference between the two methods. Since, however, Ref. 40 takes the effective throat area as equal to the geometrical throat area, direct comparison between the two works may not be justified. For more accurate work, a further study on this matter would be necessary and should include the measurement of the axial pressure distribution over the entire convergent portion of the nozzle.

I-4.2. Reaction rates

The result of the measurement of the heat transfer to a cone shows that the recombination rate is not greater than the value reported by Hinnov and Hirschberg (Ref. 8), i.e.

$$k \leq 5 \times 10^{27} (T°K)^{-4.5}$$

within an error of, at most, a factor of 10. In order to check the lower limit of the recombination rate in the plasma-jet wind tunnel, a higher settling chamber pressure, of more than 10 times the operating pressure of the present installation, is necessary.

For an ionized gas, the measurement of heat transfer to a slender cone or, more generally, a flat plate, is a good means of measuring the ionization level in the test flow and hence the recombination rate as seen from the above. This is because firstly, the wall value of ionization is always zero in an ionized boundary layer and secondly, the recombination within the boundary layer does not affect the heat transfer rate to the flat plate to a great extent. This differs from the case of dissociated flow in which there is another unknown factor k_w, the surface catalytic recombination rate, which makes it difficult to deduce the freestream conditions from the measured heat transfer rates.

The measurement of the radiative heat transfer rate taken in the present work presents an almost unique experimental result, as far as the present author is aware, as regards the inelastic two-body recombination rate in an expanding nonequilibrium ionized gas. The agreement of experiment with theory within an order of magnitude at moderate ionization levels supports the validity of the two-body recombination theory of Bond (Ref. 32) and the assumption stated in Eq. (45) under the tested condition. The disagreement of the experimental results with theory at very low ionization levels raises a doubt as to the validity of the assumption of ionic equilibrium in the settling chamber (see the preceding section).

The result of spectroscopic measurement of temperature by Adcock and Plumtree (Ref. 37) lies nearer the calculated electron temperature. This may probably be due to the fact that the spectral line wave lengths used in the spectroscopic measurement (≃4000 A) were short. It has been suggested recently (Ref. 41) that wave-bands with higher energies may tend to indicate the electron temperature while the lower energy bands may indicate the atom temperature. The agreement of the spectroscopically measured temperature and calculated atom (and electron) temperature at high ionization levels (where the electron and atom temperature are nearly equal to each other) partly supports the theory of Spitzer (Ref. 6) for the calculation of electron temperature relaxation time.

I-4.3. Transport properties and heat transfer

The good agreement of the heat transfer results for a hemisphere with the theory for a frozen boundary layer confirms that the Prandtl number is indeed very small in ionized argon. The large departure of the heat transfer rates from equilibrium boundary layer values proves that the cross-section for electron-argon atom collision is indeed very small and partly supports the transport property calculation of Penski (Ref. 24). The accuracy of the calculation of transport properties, however, cannot be judged from the present heat transfer measurement, because, apart from the uncertainty in the local distribution of heat transfer over the hemisphere, the Prandtl number affects the heat transfer rates only mildly, i.e. to the extent of one-third power.

No work has so far been done, as far as the present author is aware, on the transport properties of nonequilibrium gas. In the present work, the Prandtl and Lewis numbers in nonequilibrium flow are assumed to be equal to those values applicable to an equivalent equilibrium flow having the same ionization levels. This is based on the assumption that collision cross-sections are independent of temperature. Since the Coulomb cross-sections vary greatly at low temperatures, the present approximation may not be a good one for high ionization levels. This sets a limitation on the utilization of the present experimental work in deducing transport properties.

The result of convective heat transfer measurement with the hemisphere model shows that the surface material does not participate in recombination and that all surfaces act as an infinitely catalytic surface at the temperatures tested, i.e. $T_W < 1000\,^{\circ}K$. The factor which causes this affinity to infinitely catalytic surfaces is thought to be the increase of the ionic recombination rate at andnear the surface at lower temperatures. The approximate 'freezing point' in the boundary layer will be remote from the surface when the boundary layer is very cold, producing a near-equilibrium flow condition in the lower region of the boundary layer, the latter being more significant than the upper region. When the surface temperature is raised, the 'freezing point' will approach the surface under the same edge condition, approaching more closely to the frozen flow condition and thereby increasing the heat transfer rate. Thus in nonequilibrium ionized boundary layers, the increase in the surface temperature may result in an increase in the heat transfer rate under the above-mentioned condition, which is quite contradictory to common knowledge.

The results of radiative heat transfer measurement agree within an order of magnitude with the theoretical values of Bond when the assumption $h\nu$ = ionization potential is used. Since the radiative heat transfer rate to a body is proportional to the scale of the body for an optically thin gas, there follows the relation

$$\frac{\text{radiative heat transfer}}{\text{convective heat transfer}} \propto \text{body scale}^{1.5}$$

for such a gas. Extending the results of the present work by the above formula, it can be shown that for a sphere of 10 ft radius, the radiative heat transfer rate is approximately 30 times the convective heat transfer in the stagnation region for $\phi = 0.1$. Thus, in an ionized regime radiation is a dominant source of heat transfer when the scale of the body is large.

I-5. CONCLUSIONS

i) A computer programme for the calculation of the ionized gas flow properties in convergent-divergent nozzle flows is developed.

ii) The three-body ionic recombination rate in argon flow is not greater than $5 \times 10^{27}(T^{o}K)^{-4.5}\ cm^{6}\ mole^{-2}\ sec^{-1}$ with a possible error not greater than the factor 10.

iii) It is inferred that the spectroscopic measurement of temperature using the relative intensities of spectral lines having wave lengths around 4000 Å tends to indicate the electron temperature rather than the atomic temperature.

iv) The lack of equilibrium in the tested flow is confirmed by measuring the stand-off distance of the bow shock wave for a sphere.

v) Two methods of determining the flow properties in a plasma-jet wind tunnel, i.e. the power balance method and pressure-mass flow method, are shown to agree within the experimental error after correcting for the effective nozzle throat area.

vi) The result of the radiative heat transfer measurement agrees approximately with the simple inelastic collision theory of Bond (Ref. 32) at moderate ionization levels, and shows the presence of excess electrons at very low ionization levels, implying that over-ionization exists in the settling chamber.

vii) The heat transfer to a hemisphere from ionised argon is greater than from nonionized flow under the tested condition because the boundary layer is ionically frozen and the cold surface acts as a fully catalytic surface to ionic recombination.

I-6. REFERENCES

1. Cheng, H.K., AIAA J. 1 295 (1963)
2. Cordero, J., Dietrich, F.W., & Hurwicz, H., Aerospace Engineering 22 166 (1963)
3. Bray, K.N.C., & Wilson, J.A., Southampton Univ. Aero. & Astro. Rep. 134 (1960)
4. Bray, K.N.C., & Wilson, J.A., Southampton Univ. Aero. & Astro. Rep. 185 (1962)
5. Petschek, H., & Byron, S., Annals of Physics 1 270 (1957)
6. Spitzer, L., Jr., "Physics of Fully Ionized Gases" Chap. 5 (Interscience Publishers, New York) (1956)
7. Freeman, N.C., J. Fl. Mech. 4 407 (1958)
8. Hinnov, E., & Hirschberg, J.G., Phys. Rev. 125 795 (1962)
9. Van Dyke, M., NASA TR R-1 (1959)
10. Heybey, W.H., NAVORD Rep. 3594 (1953)
11. Cohen, C.B., & Reshotko, E., NACA TN 3326 (1955)
12. Rutowski, R.W., 1959 Proc. Heat Transfer & Fl. Mech. Inst. 110 (1960)
13. Adams, M.C., AVCO-Everett AMP 53 (1960)
14. Cohen, N.B., NASA TR R-118 (1961)
15. Hoshizaki, M., ARS J. 32 1544 (1962)
16. Pallone, A., & Van Tassell, W., ARS J. 32 436 (1962)
17. Hansen, C.F., NASA TR R-50 (1959)
18. Fay, J.A., & Kemp, N.H., AIAA J. 1 2741 (1963)
19. Yos, J.M., AVCO-RAD TM 63-7 (1963)
20. Rose, P.H., & Stankevics, J.O., AIAA J. 1 2752 (1963)

21. Scala, S.M., & Warren, W.R., ARS J. 32 101 (1962)

22. Weizel, W., & Rompe, R., "Theorie elektrische Lichtbogen und Funken" (Leibzig.) (1949)

23. Admur, I., & Mason, E.A., Phys. Fl. 1 370 (1958)

24. Penski, K., Chemie-Ingenieur-Technik 34 84 (1962)

25. Ramsauer, C., & Kollath, R., Ann. d. Physik, 9 (1931); 12 529 (1932)

26. Park, C., AIAA J. 2 169 (1964)

27. Hirschfelder, J.O., Curtiss, C.F., & Bird, R.B., "Molecular Theory of Gases and Liquids" (John Wiley & Sons, New York) (1954)

28. Fay, J.A., & Riddell, F.R., J. Aero. Sci. 25 73 (1958)

29. Van Dyke, M., Stanford Univ. Dept. Aero. Eng. Report 112 (1961)

30. Kemp, N.H., Rose, P.H., & Detra, R.W., J. Aero. Sci. 26 421 (1959)

31. Aller, L.H., Astrophysics, "The Atmospheres of the Sun and Stars" Chap. 5 (Ronald Press, New York) (1953)

32. Bond, J.W., Jr., Phys. Rev. 105 1683 (1957)

33. Harvey, J.K., & Simpkins, P.G., J. Roy. Aero. Soc. 66 637 (1962)

34. Harvey, J.K., Simpkins, P.G., & Adcock, B.D., AIAA J. 1 714 (1963)

35. Monaghan, R.J., ARC R & M 2760 (1949)

36. Bosnjakovic, F., Springe, W., Knoche, K.F., & Burgholte, P., Thermodynamics and Transport Properties of Gases,

Liquids & Solids 465 (1959)

37. Adcock, B.D., & Plumtree, W.E.G., J. Quant. Spectrosc. Radiat. Transfer 4 29 (1964)

38. Goulard, R.J., Jet Prop. 28 737 (1950)

39. Arney, G.D., Jr., & Boylan, D.E., AEDC TDR-63-19 (1963)

40. Winkler, E.L., & Griffin, R.N., NASA TN D-1146 (1961)

41. Bray, K.N.C., private communications (1963)

PART II

FLOW OF DISSOCIATED NITROGEN

II-1. LIST OF SYMBOLS

A : nozzle cross-sectional area

C_p, C_v : frozen specific heat at constant pressure and volume

D : diffusivity

$(\frac{du_e}{dx})_o$: stagnation point velocity gradient

E : electrical energy input to plasma-jet head

f : velocity profile function ($f' = df/d\eta = u/u_e$)

g : energy profile function $= h_t/h_{te}$

H : enthalpy $\equiv h + \alpha h_d$, Btu/lb unless otherwise stated

H_t : total enthalpy $= H + \frac{1}{2}u^2$, "

h : frozen enthalpy $= C_pT$, "

h_d : dissociation energy = 14,450 Btu/lb

h_t : frozen total enthalpy $= h + \frac{1}{2}u^2$, Btu/lb unless otherwise stated

h_v : energy of contamination = 16,300 Btu/lb

K : local Damköhler number

k : rate constant, $cm^6 \, mole^{-2} \, sec^{-1}$

k_w : surface catalytic recombination rate constant, fps

L_e : Lewis number

$\dot{m}$: gas mass flow rate through tunnel

N : molar number of particles

n : $= \rho\mu/(\rho_e\mu_e)$

p : pressure, atm unless otherwise stated

Q : overall heat transfer rate, Btu/sec $= Q_c + Q_r$

q : local heat transfer rate $= q_c + q_r$

R : gas constant or nose radius
r_i : distance from centre line
s : index of temperature in reaction rate, see Eq. (6a)
S_c : Schmidt number
T : temperature, $^{\circ}K$
T_d : reference temperature = 113,200 $^{\circ}K$
u, v : velocity in x and y directions
W : head cooling water loss
x, y : distance along and normal to wall
x_0 : reference length
α : atom concentration
γ : effective frozen specific heat ratio
Δ : stand-off distance of bow shock wave
δ : molar fraction of vaporized electrode material
$\bar{\eta}$: plasma-jet head efficiency
θ : vibrational constant = 3380 $^{\circ}K$
κ : polytropic constant, see Eq. (11)
λ : frozen thermal conductivity
μ : viscosity
ξ, η : dimensionless length parameter in x and y directions
ρ : density, cm^{-3} mole
ρ_d : reference density = 5.4 cm^{-3} mole
σ : frozen Prandtl number
τ : relaxation time
χ : vibrational energy

Subscripts

a : atom

c : conduction

e : edge of boundary layer

E : equilibrium

F : frozen

hx : heat transfer

m : molecule

mf : mass flow method

pb : power balance method

r : recombination

s : stagnation point

w : wall

$*$: nozzle throat

∞ : test section of wind tunnel

II-2. THEORY AND ANALYSIS

II-2.1. Fundamentals of nonequilibrium dissociated nitrogen

An approximation to the state of a dissociated pure diatomic gas has been made by Lighthill (Ref. 1) using the ideal dissociating gas model. According to the ideal dissociating gas theory, the state of equilibrium dissociation is determined by

$$\frac{\alpha_E^2}{1-\alpha_E} = \frac{\rho_d}{\rho}\exp\left(-\frac{T_d}{T}\right) \qquad (1)$$

where α is the dissociation fraction, or atom concentration

$$\alpha = \frac{\frac{1}{2}N_a}{N_m + \frac{1}{2}N_a}$$

Eq. (1) is accurate to within approximately ±5% for the following range of conditions (Ref. 1)

$$0.005 < \alpha < 0.9$$

$$0.001 < p < 100 \text{ atm} \quad .$$

The equation of state is taken to be

$$p = \rho RT(1+\alpha) \quad . \qquad (2)$$

The enthalpy of the dissociated diatomic gas is given as (Ref. 1)

$$H = (3.5 + 1.5\alpha)RT + (1-\alpha)\chi + h_d\alpha \qquad (3)$$

where χ is the vibrational excitation energy. Under a complete thermodynamic equilibrium condition, the vibrational excitation χ takes the equilibrium value. Using the harmonic oscillator model, the equilibrium vibrational excitation energy is (Ref. 2)

$$\chi_E = \frac{R\theta}{\exp\left(\frac{\theta}{T}\right) - 1} \qquad (4)$$

For a nonequilibrium flow, the rate equation for the relaxation of the dissociation fraction is derived by Freeman (Ref. 3) as

$$\frac{\partial \alpha}{\partial t} = k \rho_d \rho \left\{ (1-\alpha) \exp\left(-\frac{T_d}{T}\right) - \frac{\rho}{\rho_d} \alpha^2 \right\} \qquad (5)$$

The rate constant k takes the form (Ref. 4)

$$k = C\left(\frac{T^{\circ}K}{4500}\right)^{-s} \qquad (6)$$

Ref. 4 states that the best matching values of s and C for nitrogen are

$$s = 1.5 \qquad (6a)$$

$$C \doteq 10^{15} \quad . \qquad (6b)$$

The rate equation for vibrational-relaxation in the case of the above harmonic oscillator model is (see e.g. Ref. 5)

$$\frac{\partial \chi}{\partial t} = \frac{\chi_E - \chi}{\tau} \qquad (7)$$

The experimental results of the vibrational relaxation time measurement summarized in the paper by Stollery and Smith (Ref. 5) show that the relaxation time for nitrogen can best be approximated by

$$\tau = \frac{1.631 \times 10^{-4}}{p} \left(\frac{T^{\circ}K}{2000}\right)^{-4.21} \text{sec} \quad . \qquad (8)$$

The dissociative relaxation rate equation (5) can be written in the same form as Eq. (7) with χ and χ_E replaced by α and α_E.

II-2.2. Steady one-dimensional nozzle flow

For a steady one-dimensional flow, the rate equation (5) (and also Eq. (7)) can be written in the form (see Eq. (14), Part I)

$$\frac{d\alpha}{d\xi} = K(\alpha_E - \alpha) \qquad (9)$$

where K is the local Damköhler number

$$K \equiv \frac{x_0}{u\tau}$$

To an order of magnitude, the Damköhler numbers for dissociative and vibrational relaxation are proportional to;

$$\begin{aligned} &\text{dissociation,} \quad \rho^2 u^{-1} T^{-s} \\ &\text{vibration,} \quad \rho u^{-1} T^{5.21} \quad . \end{aligned} \qquad (10)$$

Introducing the approximate effective polytropic constant for the relaxing flow for which

$$\frac{T}{\rho^{\kappa-1}} = \text{const.} \quad (1 < \kappa \leq \frac{5}{3}) \qquad (11)$$

the proportional factors of (10) are reduced to;

$$\begin{aligned} &\text{dissociation,} \quad u^{-1} T^{\frac{2}{\kappa-1} - s} \quad (s = 1.5 \text{ in the present work}) \\ &\text{vibration,} \quad u^{-1} T^{\frac{1}{\kappa-1} + 5.21} \end{aligned} \qquad (12)$$

For any possible value of κ, the factors of (12) show that in the supersonic region of the nozzle flow the Damköhler numbers decrease very rapidly along the nozzle. Thus it is seen that these relaxing nozzle flows ultimately approach near frozen flow at large area ratios.

The freezing point can be defined in various ways. When the nondimensionalized rate equation (9) is rearranged as

$$\frac{d(\alpha - \alpha_E)}{d\xi} + K(\alpha - \alpha_E) = -\frac{d\alpha_E}{d\xi}$$

the formal solution can be written as

$$\alpha - \alpha_E = -\frac{\int \exp\left(\int K d\xi\right) \frac{d\alpha_E}{d\xi} d\xi}{\exp\left(\int K d\xi\right)} \quad . \qquad (13)$$

One way of defining the freezing point is to take the point at which the value of K is so small that the integral $\int K d\xi$ remains almost constant beyond that point (see Fig. 1(a) and (b)). If K_F is such a point, Eq. (13) reduces beyond that point to

$$\alpha - \alpha_E = -\int \frac{d\alpha_E}{d\xi} d\xi + \text{const.}$$

that is,

$$\alpha - \alpha_E = \alpha_{E,F} - \alpha_E + \text{const.}$$

i.e. α = constant.

The freezing point K value is dependent mainly on the index of temperature to which the Damköhler number is proportional. In the case of a flow with a rapidly decreasing K value along the nozzle, the integral $\int K d\xi$ approaches the pseudo-limiting value (99% of limiting value, say) earlier than that for the case of K falling slowly and the value of K_F is consequently larger. The appropriate mean value of K_F (freezing point K value) for vibrational relaxation is determined from the exact solutions for an hyperbolic nozzle

$$\frac{A}{A^*} = 1 + \left(\frac{x}{x_0}\right)^2 .$$

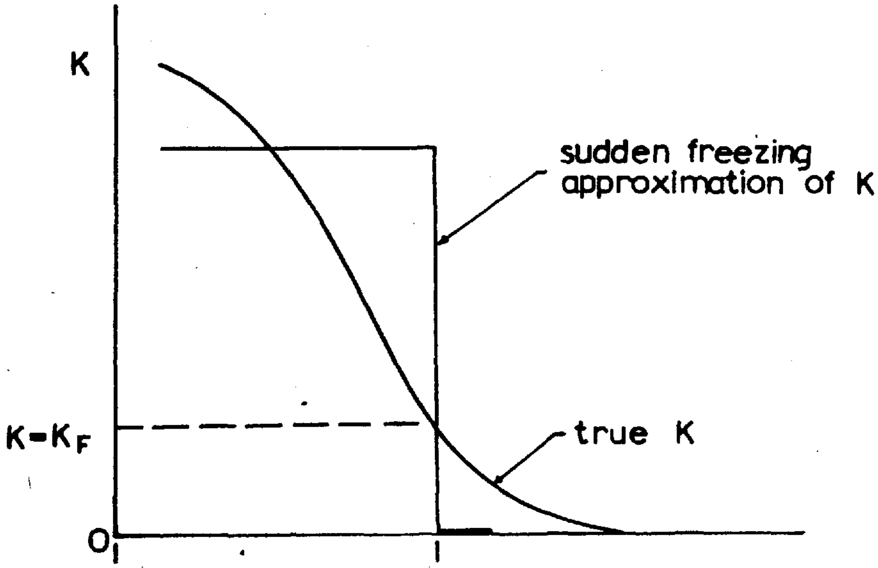

Fig. 1 (a). Variation of K (not to scale).

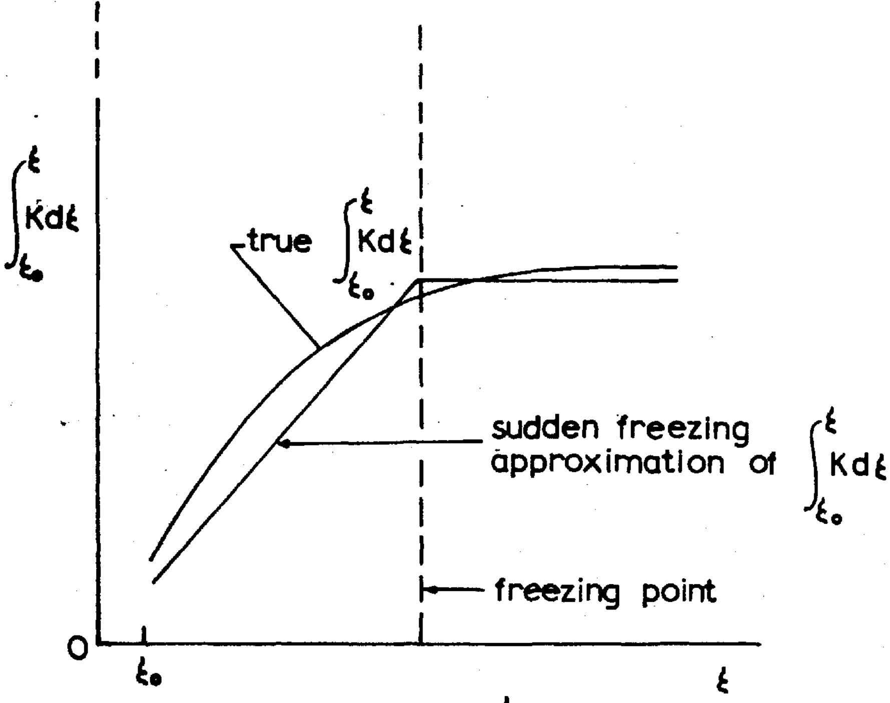

Fig. 1 (b). Variation of $\int_{\xi_0}^{\xi} K d\xi$ (not to scale).

by Stollery and Park in Ref. 6 for air. The expression used for relaxation time in air is different to that given in Eq. (8), but the absolute value of the relaxation time used in Ref. 6 agrees approximately with those calculated by Eq. (8) for the range of temperatures considered in Ref. 6, i.e. $T \leq 2000^{\circ}K$. Thus the result obtained in Ref. 6 can be used for the work with nitrogen here. The freezing point K value found in Ref. 6 was

$$K_F \text{ (vibration)} = 4 \qquad (14)$$

where the length x_0 in this case is taken as the distance from the throat to the point at which the area ratio is two. The freezing criterion Eq. (14) is not related to the criteria of Bray (Ref. 7) and Blythe (Ref. 8). Nevertheless the results of the calculation of freezing temperatures using Eq. (14) (Ref. 6) agree closely (±5% in T_F) with those utilizing Bray's criterion.

The freezing criterion for dissociative relaxation can also be written in the same form as Eq. (14). The freezing point K value here is found from

i) the computed results of dissociative relaxing flow presented by Bray (Ref. 7) (see Fig. 2 (a)), and

ii) a one sample solution of the rate equation for a near frozen flow (see Fig. 2(b)). The sample solution was obtained by performing the numerical integration using a desk calculater as in Ref. 5, the nozzle geometry and settling chamber condition being similar to those of the Imperial College one-inch

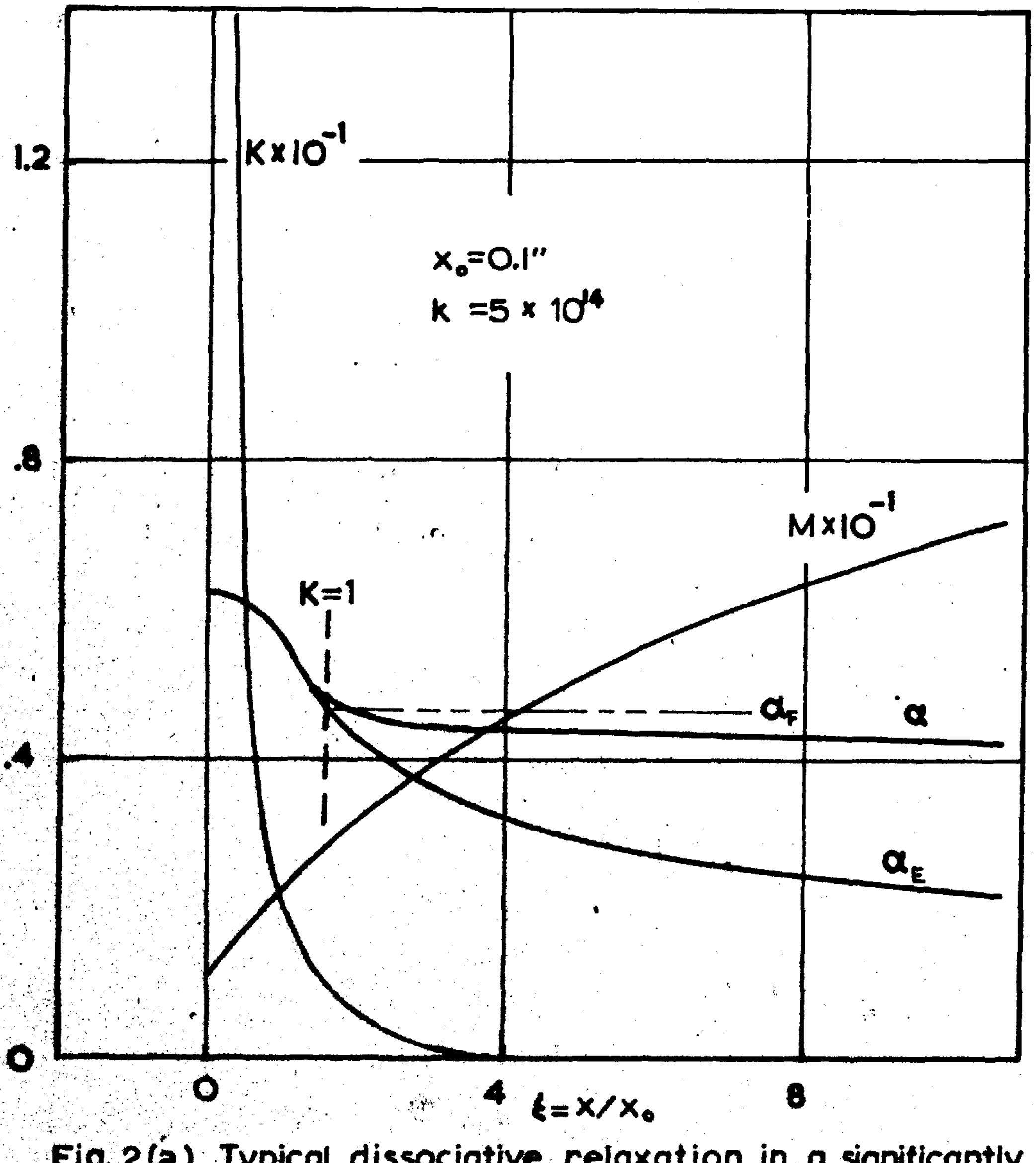

Fig. 2(a). Typical dissociative relaxation in a significantly recombining flow, taken from Bray (ref. 7). Oxygen, T_0=5900 °K, p_0=115 atm, hyperbolic nozzle.

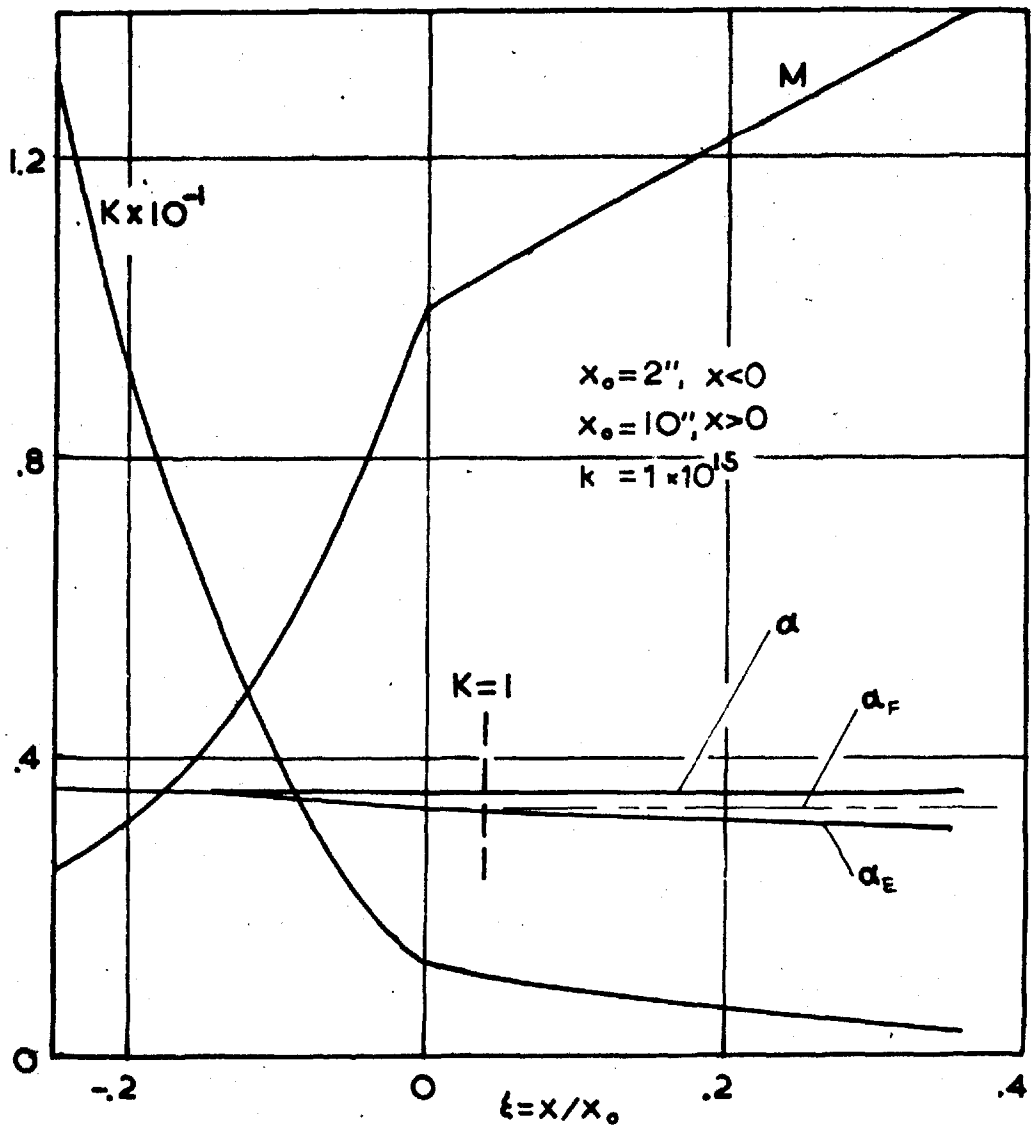

Fig. 2(b). Typical dissociative relaxation in a near frozen nozzle flow. Nitrogen, T_o=7080 °K, p_o=1.93 atm, hyperbolic nozzle.

plasma-jet wind tunnel. The freezing K value found was

$$K_F \ (\text{dissociation}) = 1 \qquad (15)$$

with the resulting error in α_F less than 5%.

When dissociation and vibration are both frozen, the energy equation becomes, from Eq. (3),

$$H_t = (3.5 + 1.5\alpha)RT + \tfrac{1}{2}u^2 + \text{const.} \qquad (16)$$

The frozen specific heat at constant pressure, C_p, and at constant volume, C_v, are both constant and so the effective specific heat ratio is

$$\gamma = \frac{C_{p_F}}{C_{v_F}} \qquad (17)$$

where

$$C_{p_F} = (3.5 + 1.5\alpha)R$$

$$C_{v_F} = C_p - (1+\alpha)R = (2.5 + 0.5\alpha)R.$$

All the flow properties can be determined using the perfect gas relations with the specific heat ratio determined by Eq. (17).

II-2.3. Shock wave stand-off distance of sphere

When a sphere is placed in the testing section of a wind tunnel through which the flow is dissociatively relaxing, the stand-off distance of the bow shock wave over the hemisphere is affected by the relaxation characteristics in the nozzle as well as behind the shock wave (see §I-2.3.). There are three limiting cases in the degree of nonequilibrium in the flow through the nozzle and behind the bow shock wave. They are;

i) case E-E; equilibrium both through the nozzle and behind the shock wave, K very large;

ii) case E-F; equilibrium through the nozzle but frozen behind the shock, K intermediate; and

iii) case F-F; frozen both through the nozzle and behind the shock, K very small.

The condition F-E is again ruled out because it is unlikely to occur. Here the effect of vibrational relaxation is neglected because of its relatively small effect on density compared with that of dissociation, except for one case to be mentioned later. For the above mentioned three limiting cases, the stand-off distance of the shock wave can be determined by using Eq. (25) of Part I, §I-2.3.

For the cases E-F and F-F, i.e. when the flow behind the shock wave is frozen, irrespective of the degree of non-equilibrium through the nozzle, the density ratio ρ_∞ / ρ_e in Eq. (25) of Part I can be determined from the Rankine-Hugoniot relation for a perfect gas with γ given by Eq. (17). When the flow behind the shock wave is in equilibrium, the density ratio can be found readily from the work of Bernstein (Ref. 9).

In Fig. 3, the stand-off distance of the 0.4" dia. sphere placed in the Imperial College one-inch plasma-jet wind tunnel under each of the above mentioned conditions is shown. The calculation was carried out in the same way as in §I-2.3. except

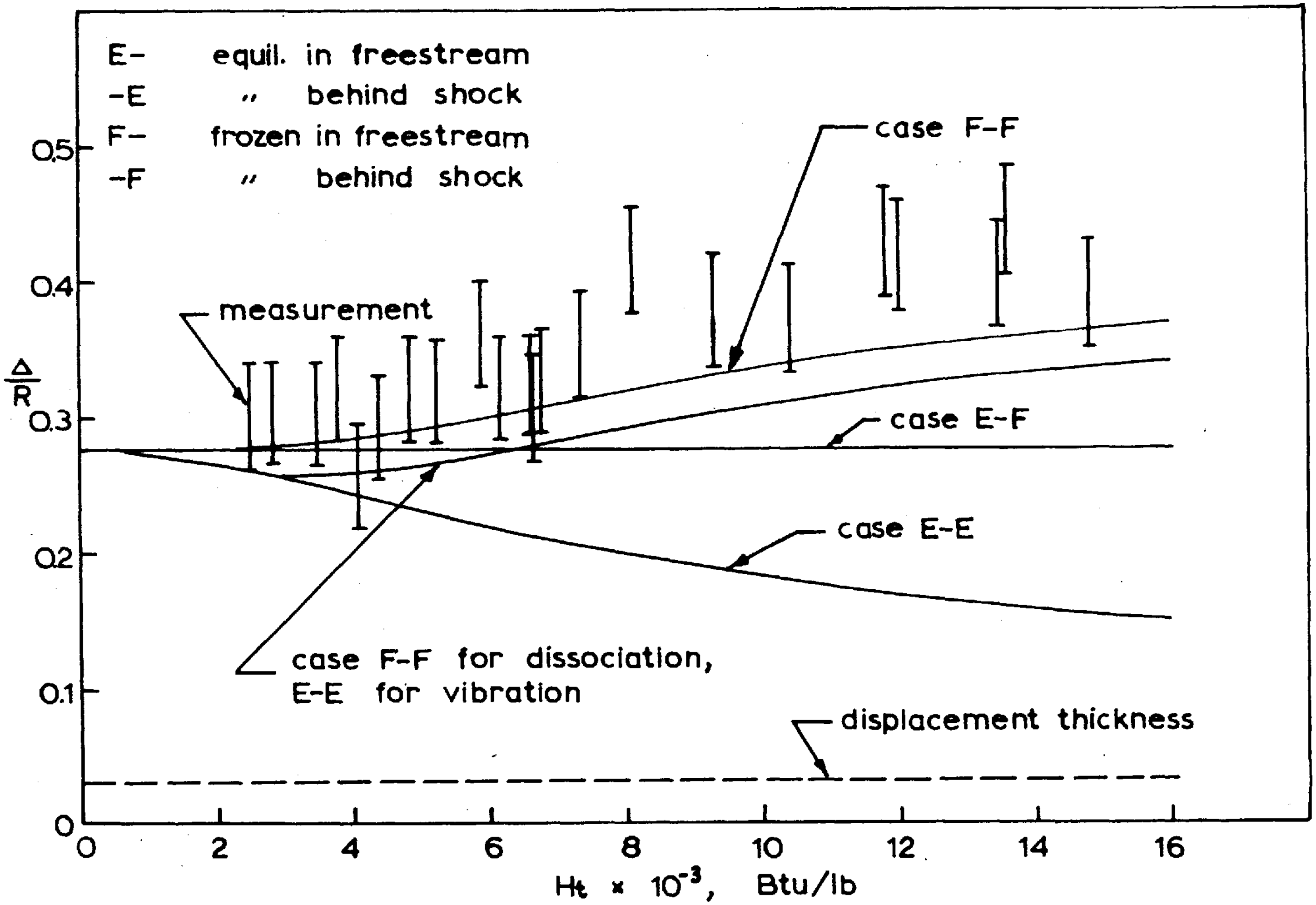

Fig. 3. Shock wave stand-off distance of hemisphere in dissociated nitrogen, measurement at $\dot{m} = 0.08$ lb/min.

that the density ratio in equilibrium flow was obtained from the work of Bernstein. In Fig. 3, the measured stand-off distances are also shown (see §II-3.1.) and compared with the theoretical values.

In Fig. 3, a fourth limiting case, the case F-F for dissociation and E-E for vibration is also shown. In general the three limiting cases mentioned earlier can each be further subdivided into three cases according to the degree of vibrational nonequilibrium. For the purpose of comparison with the experimental results (of §II-3.2.), the case of F-F for dissociation and E-E for vibration taken together seems to be most important because the measured stand-off distances are closer to the F-F (for dissociation) case. Therefore the stand-off distance for this case was calculated and is shown in Fig. 3.

II-2.4. Boundary layer and heat transfer for frozen dissociated nitrogen

The flow of dissociated diatomic gas consists of a binary mixture of atoms and molecules, and therefore the fundamental boundary layer equations, Eqs. (28) to (34) of Part I, are directly applicable. In the present work, consideration is limited to frozen flows only.

The viscosity of nitrogen at high temperatures is calculated by Admur and Mason (Ref. 10) for the nondissociated state and by Yos (Ref. 11) for the dissociated state. The viscosity values at 0.1 atm obtained by these authors are compared in Fig. 4 of Part I. (An extrapolation was made to obtain the values at 0.1 atm from Yos's data which do not give values below 1 atm.) The work of Ahtye and Peng (Ref. 12) on nitrogen provides viscosity values of only 60% of the others mentioned above at high temperatures and is not considered here on the ground that their work uses the conventional Sutherland formula as its basis. The Sutherland formula does not take account of the quantum mechanical effects in collisions at high temperatures and so cannot be used at high temperatures. As seen from Fig. 4 of Part I, the works of Admur and Mason (Ref. 10) and that of Yos (Ref. 11) agree closely over the range of temperatures considered here, i.e. $T < 7000\,^{o}K$. In the present work, the viscosity was approximated to match the data of these authors by

$$\mu = 6.31 \times 10^{-4} \left(\frac{T\,^{o}K}{2000} \right)^{0.784} \text{ poise .} \qquad (19)$$

The boundary condition for the wall value of the atom concentration must be the law of surface reaction. The exact form of the surface reaction law is not known and so the linear reaction law (Ref. 13)

$$\left(\rho D \frac{\partial \alpha}{\partial y} \right)_w = k_w \rho_w \alpha_w \qquad (20)$$

was assumed to hold. The surface catalytic reaction rate constant k_w in Eq. (20) depends on surface material, surface temperature and the way the surface is prepared. Since the recombination heat transfer is given by

$$q_r = h_d \left(\rho D \frac{\partial \alpha}{\partial y}\right)_w \tag{21}$$

one sees that the surface recombination heat transfer increases as the catalytic rate constant increases. The catalytic reaction rate constants of materials are, however, not yet known exactly.

The Prandtl and Lewis numbers in a dissociated diatomic gas were calculated first by Hansen (Ref. 14) (for air) and Ahtye and Peng (Ref. 12) (for nitrogen) using the simple collision model of Kennard (Ref. 15). Later they were calculated more accurately by Yos (Ref. 11) using a reduced Chapman-Enskog method. The data based on the simple collision theory (Hanson, Ahtye and Peng) disagree with those based on the Chapman-Enskog method (Yos) by about 20%. In the present work, the data of Yos was used on the ground that his work involves more accurate collision cross-sections. According to Yos, the frozen Prandtl number decreases from the undissociated value of 0.72 toward somewhere around 0.45 at medium dissociation levels, and the Lewis number decreases from the undissociated value of 1.4 to unity for the fully dissociated state.

II-2.4.1. Heat transfer to a hemisphere

II-2.4.1.1. Stagnation point heat transfer rate

The typical variation of the atom concentration within the stagnation point shock layer in front of a sphere placed in a near-frozen flow in a wind tunnel was obtained by solving the differential equations as in previous work of the present author, Ref. 16. The case chosen for the computation is the one with the same nozzle geometry as considered in §I-2.2. where $p_o = 0.3$ atm and $H_{to} = 9200$ Btu/lb. The result of the computation shows that the flow is almost frozen everywhere; the atom concentration at the edge of the boundary layer is very closely equal to the settling chamber value, and the surface concentration at the stagnation point is almost the same as the value calculated by the frozen flow relation (Ref. 13)

$$\frac{\alpha_{sw}}{\alpha_{se}} = \left[1 + \left\{\frac{\rho_{se}\mu_{se}}{2\left(\frac{du_e}{dx}\right)_o}\right\}^{\frac{1}{2}} \frac{S_c^{\frac{2}{3}} k_w}{0.47\,\mu_{sw}}\right]^{-1} . \tag{22}$$

Calculation shows that the second term in the parenthesis of RHS in Eq. (22) is less than 0.1 under all operating conditions for $k_w < 50$ fps and therefore, within the uncertainty in k_w, Eq. (22) can be approximated by

$$\alpha_{sw} = \alpha_{se} = \alpha_o \quad . \tag{23}$$

For these flow conditions, therefore, the heat transfer rate due to recombination is

$$q_{rs} = k_w h_d \rho_{sw} \alpha_o \tag{24}$$

Since the Prandtl and Lewis numbers are affected mainly by the atom concentration alone, (see e.g. Hansen (Ref. 14), the condition (23) states that the Prandtl and Lewis numbers are approximately constant within the boundary layer at the stagnation point of the tested model. For a flow with constant Prandtl and Lewis numbers, Fay and Riddell (Ref. 17) obtained, for frozen flow,

$$\frac{1}{\sigma_w} \frac{n_w g_w'}{1-g_w} = 0.536\, \sigma^{-0.6}\, n_w^{0.1} \left\{ 1 + (L_e^{0.63} - 1) \frac{h_d}{h_{te}} \right\}. \quad (25)$$

II-2.4.1.2. Overall heat transfer to a hemisphere

The distribution of local conductive heat transfer rate (the term conductive heat transfer is used in the present work as denoting that part of heat transfer which is due to collisions alone, i.e., the part expressible as $q = \lambda(dT/dy)$, in order to distinguish from convective heat transfer which is the sum of the conductive heat transfer and recombination heat transfer) over a hemisphere has been obtained by Kemp, Rose and Detra (Ref. 18).

The local atom concentration at the wall over the hemisphere is not known. However, in the near frozen flow considered in the preceding section, the approximate relation (23) simplifies the matter greatly. If the flow at the edge of the stagnation point boundary layer is frozen, as in the sample solution mentioned in § II-2.4.1.1., the flow at the local boundary layer edge is almost certainly frozen, because the local Damköhler number cannot be greater than that at the edge of stagnation point boundary layer. Thus

$$\alpha_e = \alpha_0 \quad . \tag{26}$$

The surface temperature takes the maximum value at the stagnation point and the minimum value at the shoulder, i.e. the point where the hemisphere adjoins the cylinder. The surface catalytic rate constant k_w varies at the temperature over the hemisphere. In the present work, a simplification was made by assuming

$$k_w = \text{constant} \times T_w \tag{27}$$

The assumption Eq. (27) is based on the fact that the true surface catalytic reaction rate is an increasing function of temperature (see Ref. 19), and that the variation of temperature over the surface is small.

Now using the condition Eq. (27), the local recombination heat transfer rate becomes

$$\frac{q_r}{q_{sr}} = \frac{k_w}{k_{ws}} \frac{\rho_w}{\rho_{ws}} = \frac{p}{p_s} \quad . \tag{28}$$

At the (ideal) Mach numbers around 2.6 for which the sample solution of §II-2.4.1.1. was performed, the local conductive heat transfer rate given by Ref. 18 is approximately proportional to pressure, i.e.

$$\frac{q_c}{q_{sc}} = \frac{p}{p_s} \tag{29}$$

Using Eqs. (28) and (29), there follows

$$\frac{q_r}{q_{rs}} = \frac{q_c}{q_{cs}} \quad . \tag{30}$$

The two overall heat transfer rates over a 0.4" diameter hemisphere, which are due to conduction and recombination, Q_c and Q_r respectively, are obtained by using Eqs. (25) and (30) and the local conductive heat transfer distribution given in Ref. 18 [illegible] by graphical integration. The conductive heat transfer parameter given by Eq. (25) is multiplied by 1.1 in order to correct for the vorticity interaction effect (see §I-2.4.3.). Newtonian approximation $(du_e/dx)_0 = u_\infty/R$ was used to calculate the stagnation point velocity gradient. The results are, neglecting the small terms,

$$Q_c = 1.12 \times 10^{-5} \sigma^{-0.6} n_w^{0.1} \left\{ 1 + (L_e^{0.63} - 1) \frac{h_d}{h_{to}} \right\} \dot{m}^{\frac{1}{2}} h_{to}^{1.394} \times \left(1 - \frac{h_w}{h_{to}} \right) \tag{31}$$

$$Q_r = 2.75\, \alpha_0 \dot{m}\, h_{to}^{\frac{1}{2}} \frac{k_w}{T_w} \quad . \tag{32}$$

II-2.4.2. Heat transfer to cone

II-2.4.2.1. Local heat transfer rate

In the frozen flow over a flat plate or a straight cone, the reduced velocity profile f' is similar and is independent of both energy and atom concentration profiles. When the surface catalytic recombination rate constant k_w is finite, the atom concentration profile becomes

$$\left(\frac{n}{S_c}\alpha'\right)' + f\alpha' - 2\xi f'\frac{\partial\alpha}{\partial\xi} = 0 \tag{33}$$

The problem of solving Eq. (33) has been studied by various authors (see e.g. Ref. 20). According to Ref. 20, the wall atom concentration near the leading edge of a flat plate or a straight cone becomes

$$\frac{\alpha_w}{\alpha_e} = 1 - \left(\frac{x}{x_c}\right)^{\frac{1}{2}} + O\left(\frac{x}{x_c}\right) \tag{34}$$

in which x_c is the characteristic length

$$x_c = \frac{9}{8}\left(\frac{1}{6}\right)^{\frac{2}{3}}\left(S_c f_w''\right)^{\frac{2}{3}}\left\{\frac{\Gamma(\frac{4}{3})}{\Gamma(\frac{2}{3})}\right\}^4 \frac{u_e}{\rho_e\mu_e}\left(\frac{\mu_w}{k_w S_c}\right)^2 \tag{35}$$

For a 15° semi-angle cone of 0.4" max diameter placed at the exit of the wind tunnel nozzle considered in §II-2.4.1.1., the magnitude of the characteristic length x_c is

for $\quad k_w \lesssim 50$ fps (36)

$$x_c \gtrsim 10 \text{ ft} \tag{37}$$

Eq. (37) therefore reduces Eq. (34) approximately for the cone considered to

$$\alpha_w = \alpha_e = \alpha_o \tag{38}$$

so that

$$q_r = k_w h_d \rho_w \alpha_o \quad . \tag{39}$$

The conductive heat transfer rate over the cone is estimated from both the Blasius solution and the work of Fay and Riddell (Ref. 17). The Blasius solution gives, for $u_e^2/h_{te} = 0$ and $n = \sigma = L_e = 1$,

$$\left\{ \frac{n_w g_w'}{\sigma_w (1-g_w)} \right\}_{Bl.} = 0.47 \qquad . \qquad (40)$$

The corrections for the Prandtl and Lewis numbers and n are made by extrapolating those given by Fay and Riddell. Because of the similarity in the relevant equations, the individual correction factors for σ, n and L_e must be the same for both the stagnation point and the flat plate solutions. Thus

$$\frac{n_w}{\sigma_w} \frac{g_w'}{1-g_w} = 0.47 \ \sigma^{-0.6} n_w^{\ 0.1} \left\{ 1 + (L_e^{\ 0.63} - 1) \frac{h_d}{h_{te}} \right\} . \qquad (41)$$

(Since the heat transfer parameter is only weakly dependent on the velocity profile and because the influence of velocity profile on the effect of σ, n, and L_e is of secondary magnitude, the extension of Fay and Riddell's work to the case of a flat plate is thought to be a good approximation.) The effect of u_e^2/h_{te} has been computed for the particular case of $\sigma = 0.66$ and $u_e^2/h_{te} = 1.5$ in which the Blasius profile are used and the method outlined by Eqs. (40) and (41) of Part I and it was found to increase the factor 0.47 in Eq. (41) to 0.48. The calculated Prandtl number varies between 0.72

and 0.45 and u_e^2/h_{te} lies between 1.4 and 1.8 depending on the atom concentration in the particular chosen condition. These variations in Prandtl number and u_e^2/h_{te} are neglected and the value 0.48 was used for the factor in Eq. (41) for all cases. Thus the final form of heat transfer rate parameter over the flat plate and cone becomes

$$\frac{1}{\sigma_w}\,\frac{n_w g_w^{0}}{1-g_w} = 0.48\ \sigma^{-0.6}\,n_w^{\,0.1}\left\{1+\left(L_e^{\,0.63}-1\right)\frac{h_t}{h_{to}}\right\}. \quad (42)$$

II-2.4.2.2. Overall heat transfer to cone

The overall heat transfer rates to a 15° semivertex angle cone of 0.4" diameter placed in the previously considered sample nozzle flow due to conduction and surface recombination are obtained by integrating the local heat transfer rates given in the preceding section over the surface area. The integrations are straightforward because q_r is constant (Eq. (39)) and q_c is a function only of x. The results are, neglecting the small terms,

$$Q_c = 1.35\times10^{-5}\ \sigma^{-0.6}\,n_w^{\,0.1}\left\{1+\left(L_e^{\,0.63}-1\right)\frac{h_d}{h_{to}}\right\}\dot{m}^{\frac{1}{2}}\,h_{to}^{\,1.394}\left(1-\frac{h_w}{h_{to}}\right) \quad (43)$$

$$Q_r = 1.96\,\alpha_0\,\dot{m}\ h_{to}^{\frac{1}{2}}\,\frac{k_w}{T_w}\ . \quad (44)$$

II-2.5. Radiative energy transport

Yos (Ref. 11) calculated the radiant power using the semi-classical formula of Kramers (Ref. 21) for pressures between 1 and 30 atm. The results are presented in Ref. 11 in a diagram and so they are not reproduced here. These data are extended for lower pressures using the proportional relationship

$$w \propto p^2 \phi^2$$

so that they may be compared with the experimental results in §II-3.4.

II-3. EXPERIMENT

To confirm the theories given in the preceding chapter, the following measurements were taken:

i) the stand-off distance of the bow shock wave from a hemisphere;

ii) the heat transfer to a hemisphere and a cone with metallic or ceramic surfaces; and

iii) the radiative heat transfer.

The wind tunnel and the models used are the same as those described in Part I except that the surface materials of the convective heat transfer models were different.

II-3.1. Operation of wind tunnel with nitrogen

The arc is initiated in argon either at 160 v or 320 v open circuit as described in §I-3.1., and changed over to nitrogen operation by controlling the two gas supply valves. The mean operating voltage of the arc was around 60 v. The repeatability of the tunnel is shown in Table 1.

A brief test with the impact pressure probe has shown that flow is uniform at the exit of the nozzle over 60% of the exit diameter for nitrogen flow. The record of voltage and current of the main electrodes has shown that there is an oscillation due to the fluctuation of the arc in nitrogen with frequencies of about 2.5 kc/s together with harmonics of frequencies of the order of a few megacycles. Therefore,

Table 1. Repeatability of tunnel

	nitrogen	nitrogen
gas flowmeter pressure, psig.	0	0
power control setting, %	20	40
open circuit voltage	320	320
average H_{tpb}, Btu/lb	4705	8187
number tested	17	13
standard deviation in P_o, %	2.94	0.88
standard deviation in H_{tmf}, %	4.15	5.44

any steady state value of measurement in nitrogen is a time average (see §II-3.1.3.).

II-3.1.1. Determination of flow properties

The power balance method and the pressure-mass flow method are used to determine the flow properties. The power balance method is the same as that described in the work for argon, §I-3.1.2. The experimental error in this method is given by Eq. (48) of Part I.

The pressure-mass flow method is worked out by considering the nature of the flow through the tunnel to be frozen. The freezing criterion Eq. (14) was applied to determine the freezing point of vibrational excitation in the Imperial College plasma-jet wind tunnel. The result shows that the vibrational excitation is frozen in the convergent portion of the nozzle in the tunnel. Also, using the freezing criterion of Eq. (15), the dissociation is seen to be frozen at low subsonic Mach numbers in the plasma-jet wind tunnel. For the sake of simplicity, therefore, both vibration and dissociation are assumed to be frozen at the settling chamber values, and the relations for the completely frozen flow, Eqs. (16) and (17) are utilized to calculate the flow conditions. Using the specific heat ratio of Eq. (17), the settling chamber condition is computed from the perfect gas relations as a function of the settling chamber pressure and mass flow rate through the nozzle. The results are presented in chart form in the Appendix and are tabulated in Ref. 22. The geometrical throat area was used in the calculation. The true, effective throat area is found by subtracting from the geometrical throat area the contribution of the displacement thickness which in this case is (see §I-3.1.2.)

$$\frac{\delta_*}{r_*} = -0.02 \left\{ \frac{0.15}{\dot{m}(\mathrm{lb/min})} \right\}^{\frac{1}{2}} \quad . \qquad (44a)$$

The procedure for the correction for the displacement thickness is described in the chart.

In the pressure-mass flow method for nitrogen, therefore, the enthalpy H_t ($= H_{tmf}$) is read directly from the chart given in the Appendix for the measured values of p_0 and $\dot{m}$ (corrected for displacement thickness). The error in this case is given in Ref. 22. Typical calculations show that the mass-flow method is approximately twice as accurate as the power balance method in this case.

The tested flow conditions as determined by the above mentioned two methods are described in more detail in the subsequent sections. The characteristic constants of the flow, i.e. mean free path and Reynolds number, are similar to the values for argon shown in Table 1 of Part I.

II-3.1.2. Effect of gas contamination

The model surfaces always showed an deposit of foreign materials on the surface during the course of each experimental run in nitrogen. This first became noticeable about 10 sec after starting the arc under the worst condition and clearly visible after about 1 minute. This is thought to be due to the contamination of the nitrogen by the electrode materials.

In the Imperial College plasma-jet wind tunnel, the main eroding part is the copper anode, since the tungsten cathode has shown very little wearing rate compared with the copper anode. Copper is first vaporized by the bombardment of electrons, and the energy absorbed in this process is 3.29 ev per atom. The vaporized copper atoms are ionized under the influence of the electrical field, absorbing another 7.724 ev. The total energy of formation of one copper ion in the gas is therefore 11.0 ev or 16.300 Btu per lb. of nitrogen, i.e. 1.13 times the dissociation energy of nitrogen. The wearing rate of the copper electrode observed during 12 months by observing the change of electrode shape is of the order of 0.5 lb per 10 lb of nitrogen gas, or about $\delta = 0.025$, where δ is the molar fraction of vaporized material. In the settling chamber, part of the ionized copper atoms will recombine, but due to the low ionization potential of copper, most atoms will remain ionized at least until they pass the nozzle throat.

The electrical energy input to the head by the arc discharge, E, is thus divided in nitrogen flow into i) flow enthalpy H_t, ii) gas contamination by electrode material and iii) wall cooling loss, i.e.

$$\frac{E}{\dot{m}} = H_t + \delta h_v + \frac{W}{\dot{m}} \tag{45}$$

where h_v is the mean effective energy of formation of a contaminating molecule, which is 11 ev (16,300 Btu/lb) for copper.

The amount of vaporization is proportional to the mean energy carried by the bombarding charged particles, and therefore should be approximately proportional to the operating voltage of the arc for a given current. This may be the reason why there is significant contamination in nitrogen flow while in argon the flow is essentially clean. In nitrogen, it is the vaporized electrode materials that provide most of the free electrons needed to conduct the electrical current, because the mean translational temperature of the nitrogen gas is too low to produce significant gas ionization, and the ionization potential of nitrogen is higher than that of copper. On the other hand, in argon gas, a more than sufficient number of electrons is provided by the thermal ionization of argon atoms to conduct the electrical current.

Comparing Eq. (45) with Eq. (47) of Part I, it is seen that in this case the total enthalpy determined from the power balance method is the sum of the true total enthalpy and contamination energy,

$$H_{tpb} = H_t + \delta h_v \tag{46}$$

Supposing that H_{tmf} is a measure of the true enthalpy, then,

$$\frac{H_{tpb}}{H_{tmf}} = 1 + \delta \frac{h_v}{H_t} \tag{47}$$

In Fig. 4, the above ratio is compared, and it shows that the ratio is appreciably greater than unity at low enthalpy levels. At high enthalpy levels, the error in the experiment makes it difficult to detect the difference between H_{tpb} and H_{tmf} because the second term in Eq. (47) in this case tends to vanish.

The power balance method and pressure-mass flow method do not agree, particularly at low enthalpy levels, as shown in Fig. 4. In order to check the two methods, therefore, another enthalpy value, denoted H_{thx}, was derived from the measured heat transfer rate to the hemisphere model. The experimental mean values of heat transfer rate to the hemisphere model (see §II-3.3.) are substituted into Eqs. (31) and (32) to obtain h_{to}, using the catalytic rate constant of 0.063 T_{sw} fps established by the present experiment (see §II-3.3.). The results are compared with H_{tmf} in Fig. 4. It is seen from Fig. 4 that the heat transfer results agree better with the power balance method for the determination of enthalpy than with the pressure-mass flow method. This

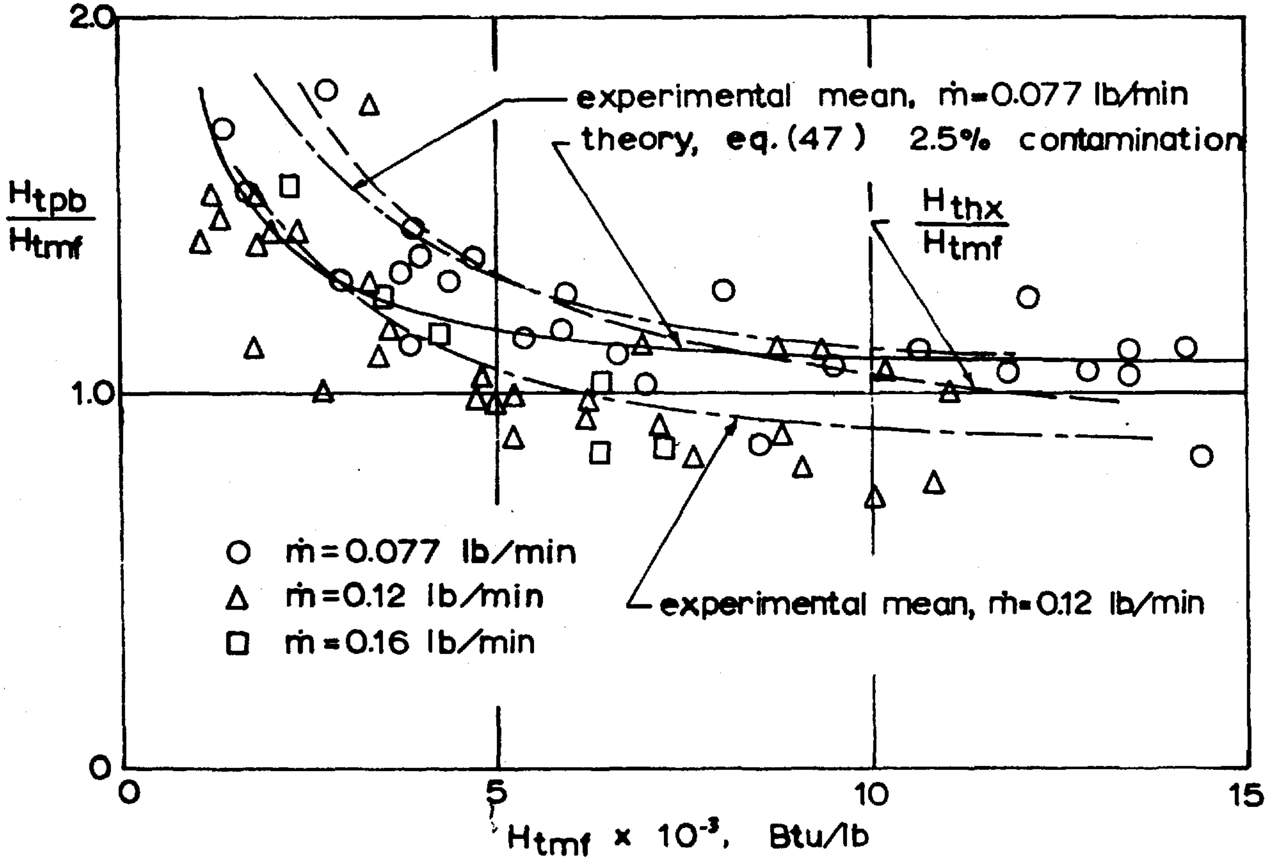

Fig. 4. Power balance and frozen mass flow methods compared for nitrogen

figure also shows that the use of Eq. (47) with $\delta = 0.025$ is approximately compatible with both sets of experimental values of H_{tpb}/H_{tmf} and H_{thx}/H_{tmf}. Thus one sees that the latent energy of ionization of electrode materials, h_V, is given out either to the surface of the model or to the translational energy of the gas before the metallic ions reach the model surface. The exact mechanism of the recovery of the contamination energy is not known. From the works of Part I, §I-3.3., however, it is apparent that the recombination of metallic ions in the boundary layer near the wall may account for the increase in heat transfer.

In the present work, a compromise between the power balance and pressure mass flow methods was made in the case of nitrogen flow to minimize the scatter of the experimental data. This is done by calculating H_{tmf} first and then converting to H_{tpb} by using the conversion curve found from Fig. 4. The resulting H_{tpb} values then have less scatter arising from experimental error than the directly determined H_{tpb}.

The conversion curve in Fig. 4 is obtained from the plasma-jet efficiency data of Fig. 5. As seen from Fig. 5, the experimental efficiency in nitrogen is relatively well defined when compared with the data for argon, Fig. 10 of Part I. This may be because the average efficiency is higher than in argon.

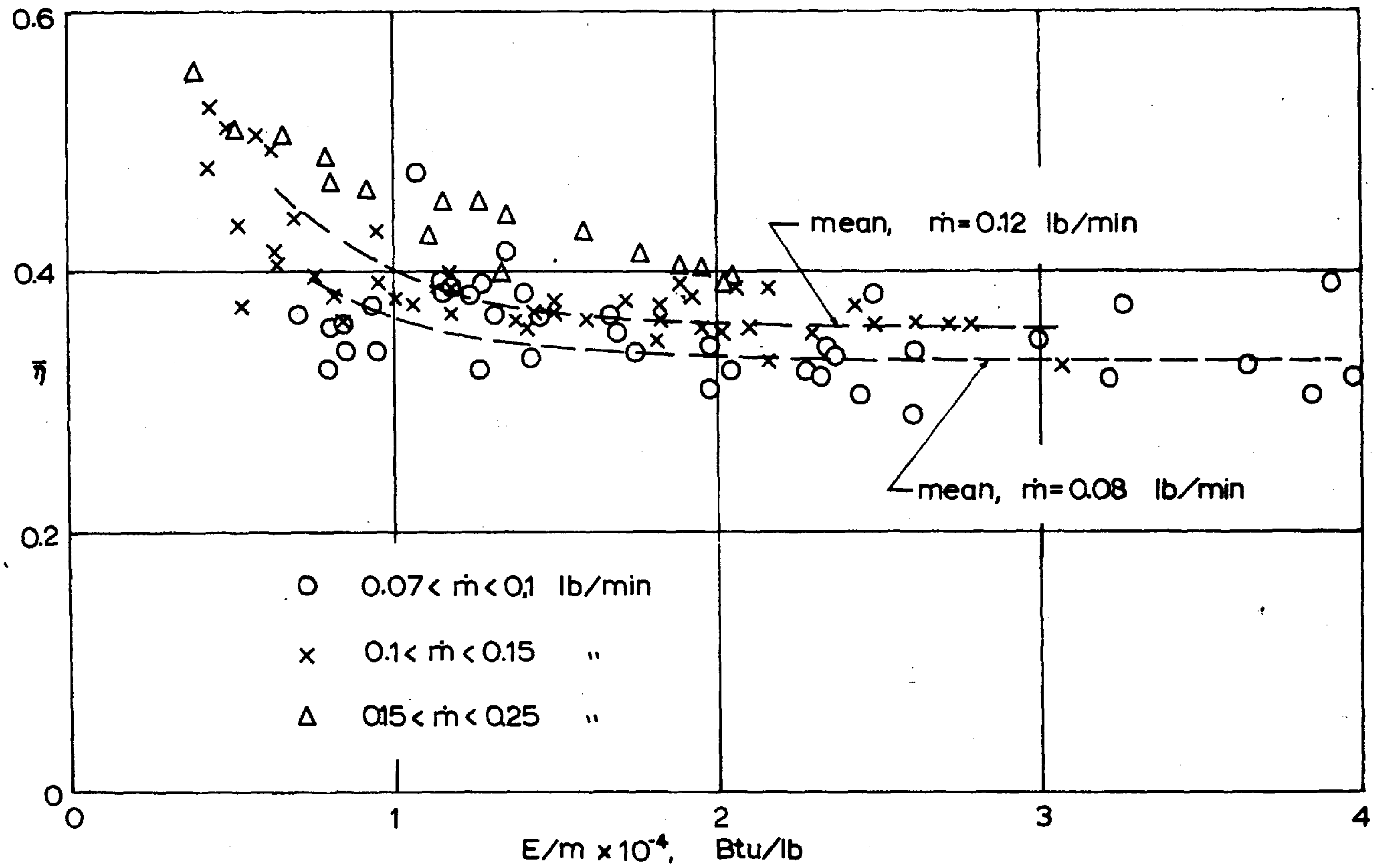

Fig. 5. Tunnel head efficiency for nitrogen

Theoretically, the cooling water loss W will decrease as mass flow rate increases. The cooling water loss is the integral sum of the heat transfer to the electrode components and to the non-electrode parts. The heat transfer to the electrodes is controlled mainly by the arc characteristics and is not directly dependent on the gas mass flow rate. The heat transfer to the non-electrode parts is approximately proportional to $\mathring{m}^{\frac{1}{2}}$ (see e.g. Eq. (43)). Thus the theoretical head efficiency must be of the form

$$\eta = C_1 - C_2 \mathring{m}^{-\frac{1}{2}} H_t^{-1} \quad . \tag{48}$$

The relation Eq. (48) is not confirmed in the present experiment, but at least a trend for the efficiency to increase as the mass flow increases is observed in Fig. 5.

It is possible to rearrange the continuity equation through the nozzle into the form Eq. (22) of Part I for nitrogen flow. The resulting expression is

$$h_{to} = \frac{3.5 + 1.5\alpha_o}{1 + \alpha_o} \left(\frac{\Gamma \, p_o A*}{\mathring{m}} \right)^2$$

where

$$\Gamma = \gamma^{\frac{1}{2}} \left(1 + \frac{\gamma - 1}{2} \right)^{-\frac{1}{\gamma - 1} - \frac{1}{2}}$$

Thus the factor $(p_o/\mathring{m})^2$ is approximately proportional to the frozen enthalpy h_{to}. In Fig. 6, the parameter $(p_o/\mathring{m})^2$ is plotted against $E/\mathring{m}$, and it shows that there is an appreciable amount of dissociation at high enthalpy levels, because if no

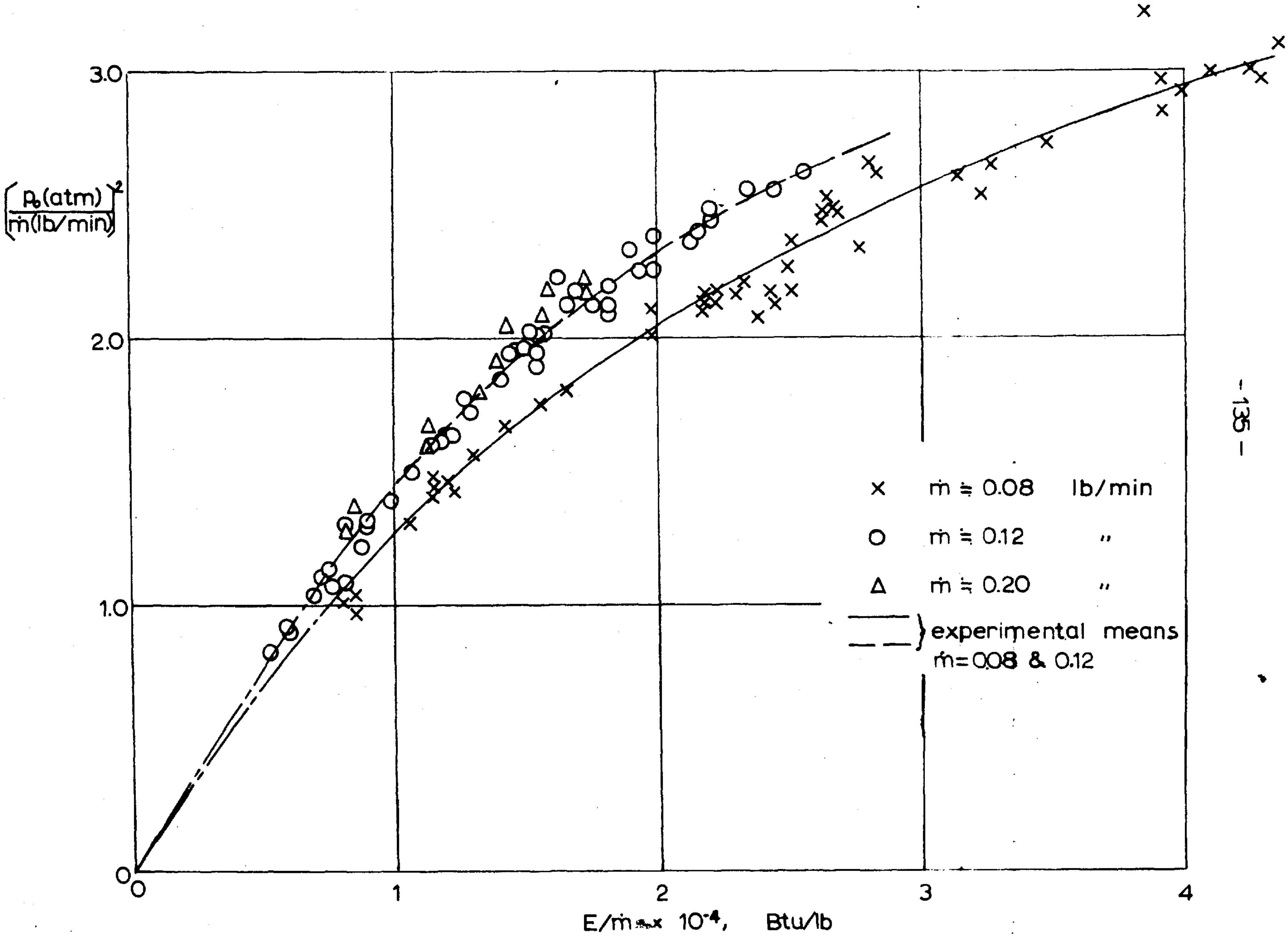

Fig. 6. Relationship between $(p_0/\dot{m})^2$ and $E/\dot{m}$ for nitrogen

energy is absorbed by dissociation, then $(p_0/\dot{m})^2$ must vary linearly with $E/\dot{m}$.

II-3.1.3. Effect of arc fluctuation

In Ref. 23, Harvey, Simpkins and Adcock reported on the nature of the fluctuations in the arc and in the brightness of the exit flow when the plasma-jet is operated with nitrogen, but since the exact nature of this fluctuation is not known, no effort has been made to correct for its effect on the heat transfer measurements. Because of this phenomenon, the heat transfer results are interpreted as a time average of a somewhat large fluctuation (± 40% max.). Since the measurement of heat transfer to the hemisphere and cone models is aimed mainly at the detection of a difference between the catalytic and non-catalytic surfaces, the presence of this fluctuation is not an insurmountable difficulty. The results must, however, be interpreted as gross averages. In the determination of the stand-off distance of the shock wave from a hemisphere, this fluctuation plays an important role and, therefore, due consideration is given to it in interpreting the test results in the following section.

II-3.2. Shock wave stand-off distance measurement

Shock wave stand-off distances from the hemisphere model are measured using the same technique as described in Part I, §I-3.2. Typical pictures of the shock wave are shown in Fig. 7 and are compared with a picture taken with an argon flow. A typical photo-densitometer trace across the shock layer is shown in Fig. 8 (see §I-3.2.).

As seen from Figs. 7 and 8, the shock waves are so diffuse that it is difficult to determine their exact positions. This may be due partly to a fluctuation in the position of the shock wave synchronising with the arc fluctuation. Simpkins and Harvey (Ref. 24) took motion pictures of the bow shock wave of a flat circular disc in the tunnel with a high speed camera, in which it is shown that the shock wave stand-off distance and the luminance change greatly because of the arc fluctuation. The fluctuation of the shock wave stand-off distance as recorded by the high speed camera has a frequency of approximately 2.5 kc/s, which agrees with the arc fluctuation frequency reported in Ref. 23. The exposure time of the camera usually employed in the present study is at least 1/200 sec and therefore is long enough to average the shock shape over at least 10 cycles of such a fluctuation. The precise significance of the observable position which the shock wave occupies is not well known, but because the illumination is much brighter when the stand-off distance is larger, the average shock stand-off distance displayed is thought to be biased toward the greater stand-off distance value.

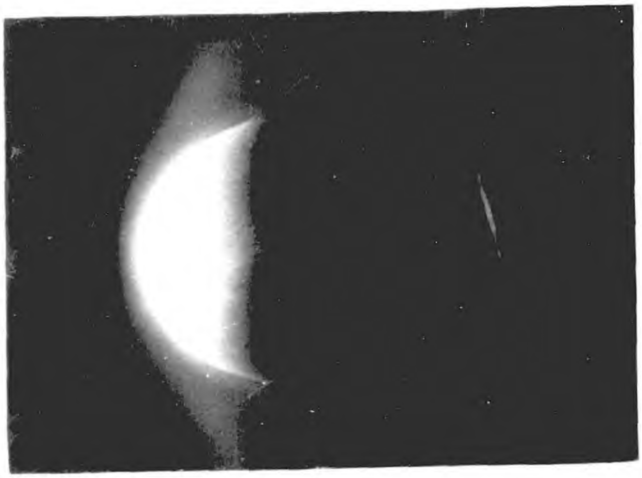

(a) nitrogen
$H_t = 2560$ Btu/lb
$\alpha = 0$
$\rho_\infty = 0.00076$ amagat

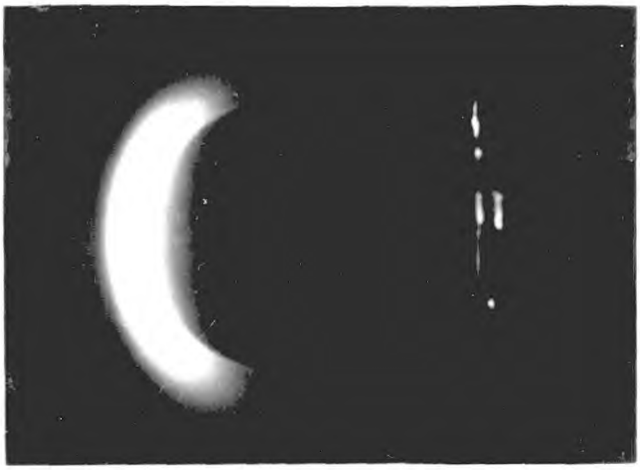

(b) nitrogen
$H_t = 9270$ Btu/lb
$\alpha = 0.36$
$\rho_\infty = 0.00051$ amagat

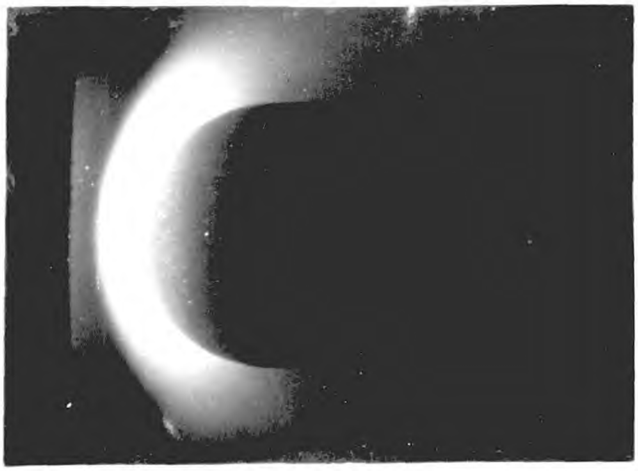

(c) argon
$H_t = 1850$ Btu/lb
$\phi_0 = 0$
$\rho_\infty = 0.0014$ amagat

Fig. 7. Detached shock waves for hemisphere, picture

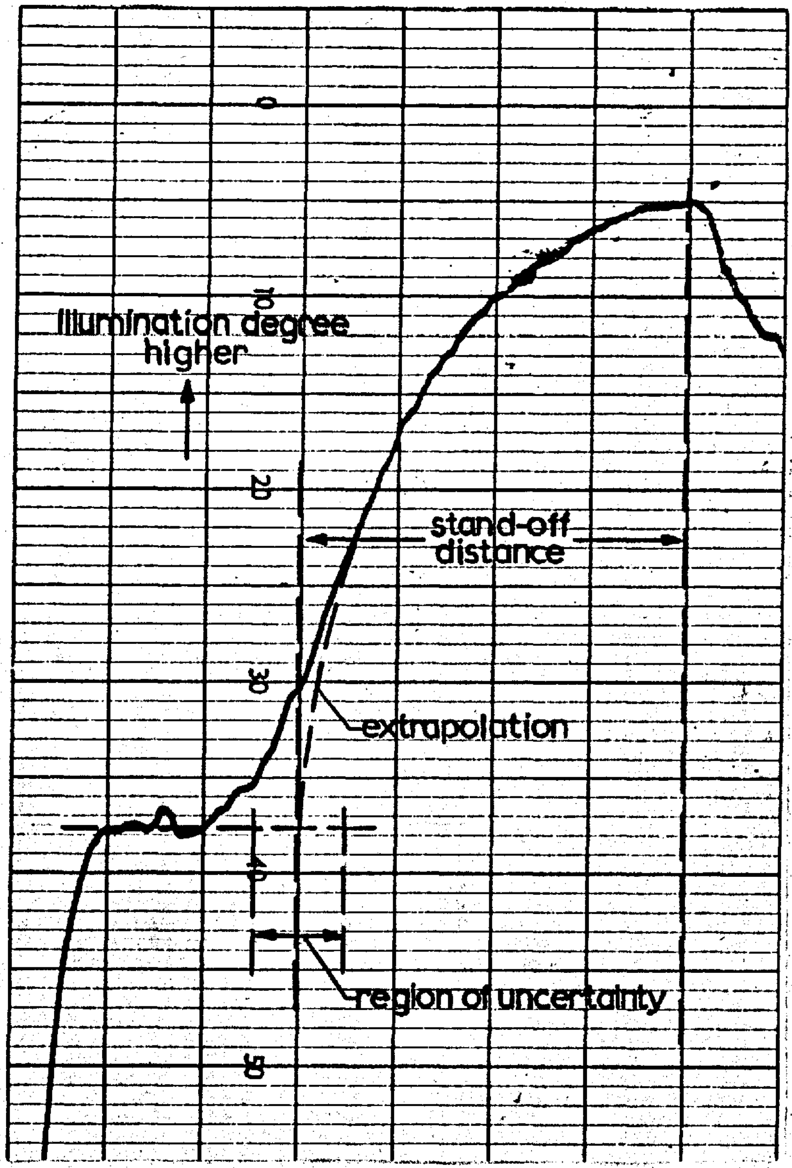

Fig. 8. Typical microphotodensitometer trace across stagnation region shock layer and the method of determining shock wave stand-off distance, nitrogen

The other factor that makes the shock wave position unclear is the apparent increase in thickness of the shock front at low densities. The density of the tunnel exit flow lies in the region

$$3 \times 10^{-4} < \rho_\infty < 1 \times 10^{-3} \text{ amagat}$$

in nitrogen, and the accompanying mean free path L is thus

$$\frac{1}{15} > \frac{L}{\Delta} > \frac{1}{50} .$$

Thus the thickness of the shock wave, which is usually a few mean free paths, is a substantial portion of the stand-off distance.

Coupled with these difficulties is the fact that the non-linearity of the photographic sensitivity of the plates make an estimate of the position even more difficult. In defining the shock wave position therefore, ±2.5 mean free paths are allowed as the possible uncertainty in the determined position of the shock wave.

In Fig. 3, the results of measurements incorporating above tolerance are shown, and it is observed that the measured stand-off distance agrees approximately with the theoretical values for frozen flow, i.e. frozen vibration and dissociation through the nozzle and behind the shock. The experiment thus corroborates the theoretical requirement that the flow of nitrogen is frozen completely under the tested condition.

The experimental results shown in Fig. 3 also prove that dissociation is indeed taking place in the wind tunnel settling chamber, for if the gas is not dissociated, the stand-off distance must remain constant at varying enthalpy levels.

II-3.3. Heat transfer measurements, hemisphere and cone

A hemisphere and a cone of the same dimensions as those used in Part I, §I-3.3. were used for the measurement of convective heat transfer from the dissociated nitrogen. The surface materials used are;

i) the hemisphere; copper, stainless steel and 5210-3C boro-silicate ceramic coating; and

ii) the cone; copper, chromium-coated copper and 571 boro-silicate ceramic-coated copper.

The stainless steel used was 'Staybrite' FMB BS 581 having the chemical composition of C - 0.07, Si - 0.30, Mn - 0.80, Cr - 18.0, Ni - 8.5, and Mo - 2.75%. The 5210-3C boro-silicate ceramic coating was developed and applied by Ferro-Solaramic group of Ferro-Enamels Ltd. to the above stainless steel. The procedure for coating is the same as for the 571 coating described in §I-3.3. except that the firing is carried out at 950°C for 60 minutes. The coating was applied with an average thickness of 0.0011". The 571 coating is applied in the same way as that described in §I-3.3.

Tests were carried out for the following conditions;

$$0.07 < \dot{m} < 0.2 \text{ lb/min},$$

$$15 < E < 80 \text{ kw},$$
$$0.08 < p_0 < 0.3 \text{ atm},$$
$$3 \times 10^{-4} < \rho_\infty < 2 \times 10^{-3} \text{ amagat.}$$

The metallic model surfaces always showed an accumulation of foreign materials on the surface as the experiments proceeded in nitrogen (see §II-3.1.1.). This became noticeable about 30 sec after starting the arc, and there was practically no change in the average thermocouple reading during the period 3 to 30 sec immediately after starting (see §I-3.3.). The thermocouple reading was taken, therefore, at exactly 30 sec after the initiation of the arc. In the case of ceramic-coated models, the deposit was recognizable only after a run of about 1 minute, and at first only around the stagnation region of the hemisphere. In earlier measurements, therefore, the surface of the model was cleaned after each run and was covered initially with a thin PTFE sheet to protect the surface from being poisoned by the blowdown of electrode materials at the initiation of the arc. The use of the protective sheets was found, however, to have no measurable effect on the results and therefore in the later experiment it was abandoned.

It was noted that there was a slight increase of heat transfer to all models as the number of runs proceeded. Both commercial and oxygen-free nitrogen were used, but no difference in heat transfer was found between them.

The results of the tested are presented in Figs. 9 and 10 and are compared with the theoretical values of §II-2.3.

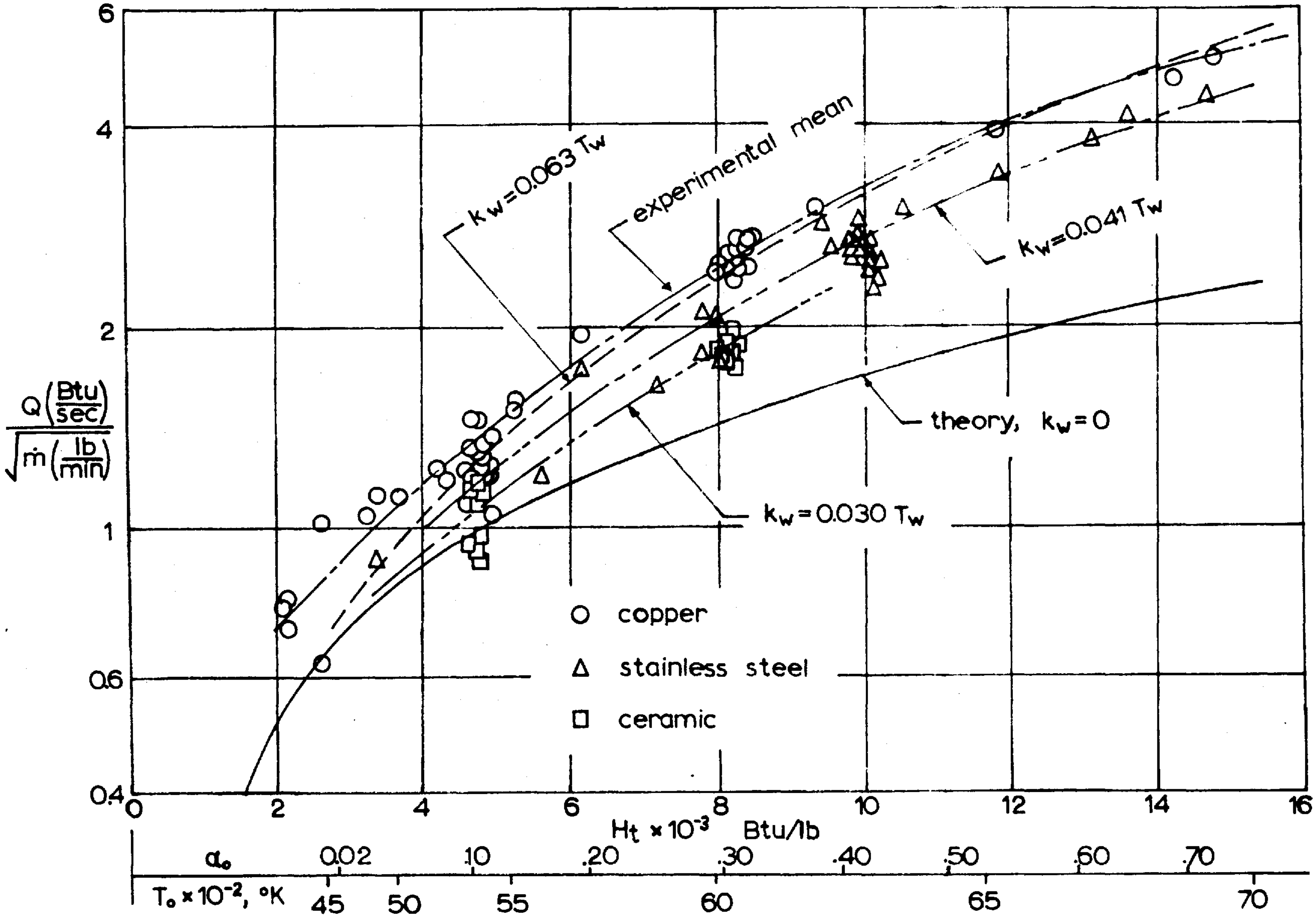

Fig. 9. Heat transfer to hemisphere from dissociated nitrogen

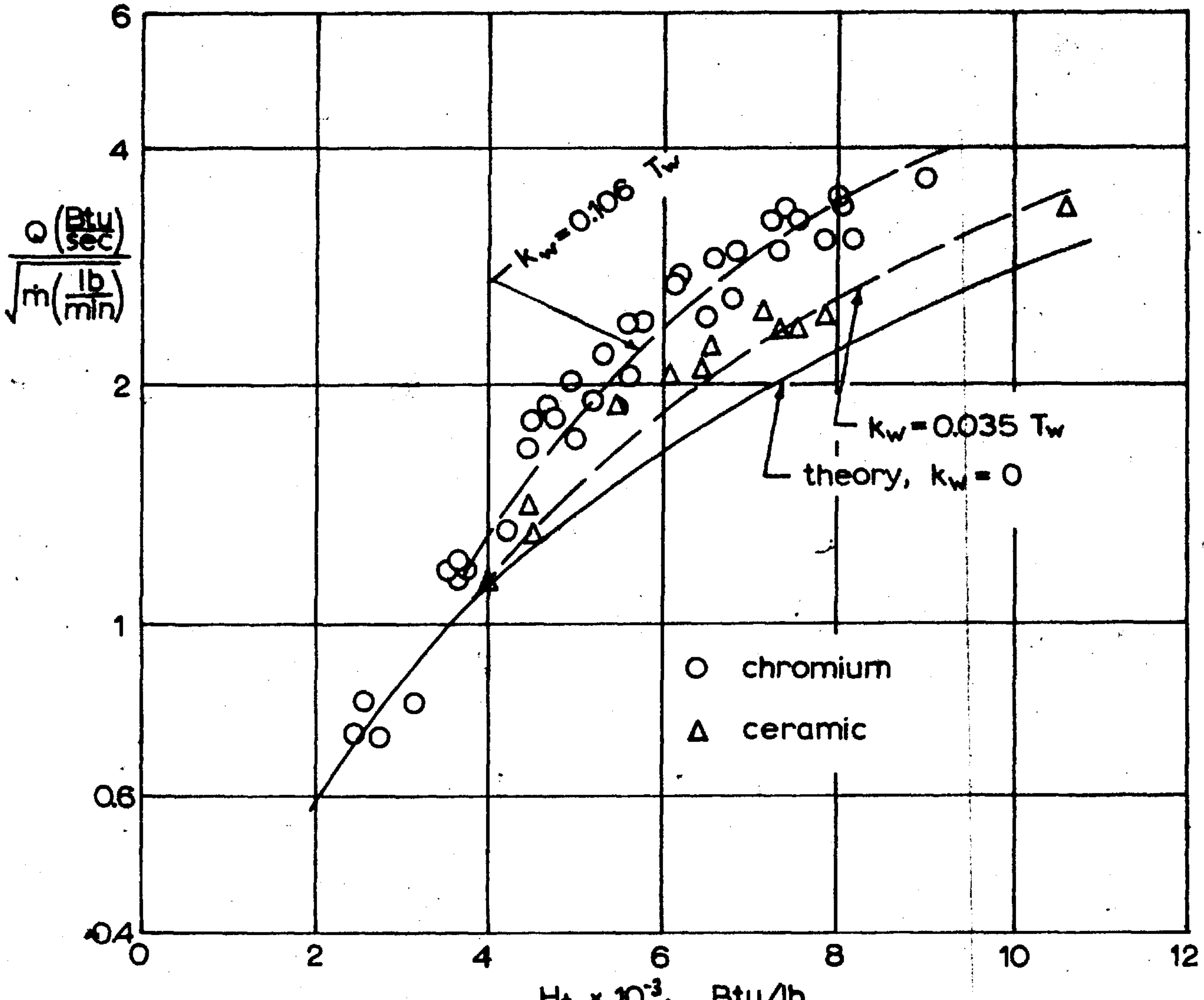

Fig. 10. Heat transfer to 30° included-angle cone from dissociated nitrogen

The average surface temperatures based on $\dot{m}$ = 0.1 lb/min are calculated from the thickness of the model wall and the effective thermal conductivities of the materials;

i) copper : 7.7×10^{-2} Btu ft^{-1} sec^{-1} $(deg\ C)^{-1}$
ii) stainless steel : 3.77×10^{-3} "
iii) ceramic-coated copper : 2.5×10^{-2} "
iv) ceramic-coated stainless steel : 3.43×10^{-3} " .

The calculated average wall temperatures are shown in Fig. 11. The radiative heat transfer was again neglected for the same reason as given in §I-3.3. (see also the following section) .

Figs. 9 and 10 show that all the experimental values of heat transfer rates are considerably higher than any of the theoretical values for conductive heat transfer alone, i.e. for $k_w = 0$, showing that there is an effective dissociation in the flow and recombination at the surface. The value of the best matching k_w for each surface is indicated in Figs. 9 and 10. Since k_w is determined from Eq. (32) or (44) as

$$\frac{k_w}{T_w} = \frac{Q - Q_c}{2.75\ \alpha_0 \dot{m} \sqrt{h_{to}}} \quad \text{or} \quad \frac{Q - Q_c}{1.96\ \alpha_0 \dot{m} \sqrt{h_{to}}} \qquad (49)$$

where Q = measured value and
Q_c = theoretical value,

the error in the determination of k_w can be estimated after considering the error in Q_c. At low enthalpy levels there should be no recombination heat transfer, however the experimental heat transfer rates exceed the theoretical values by

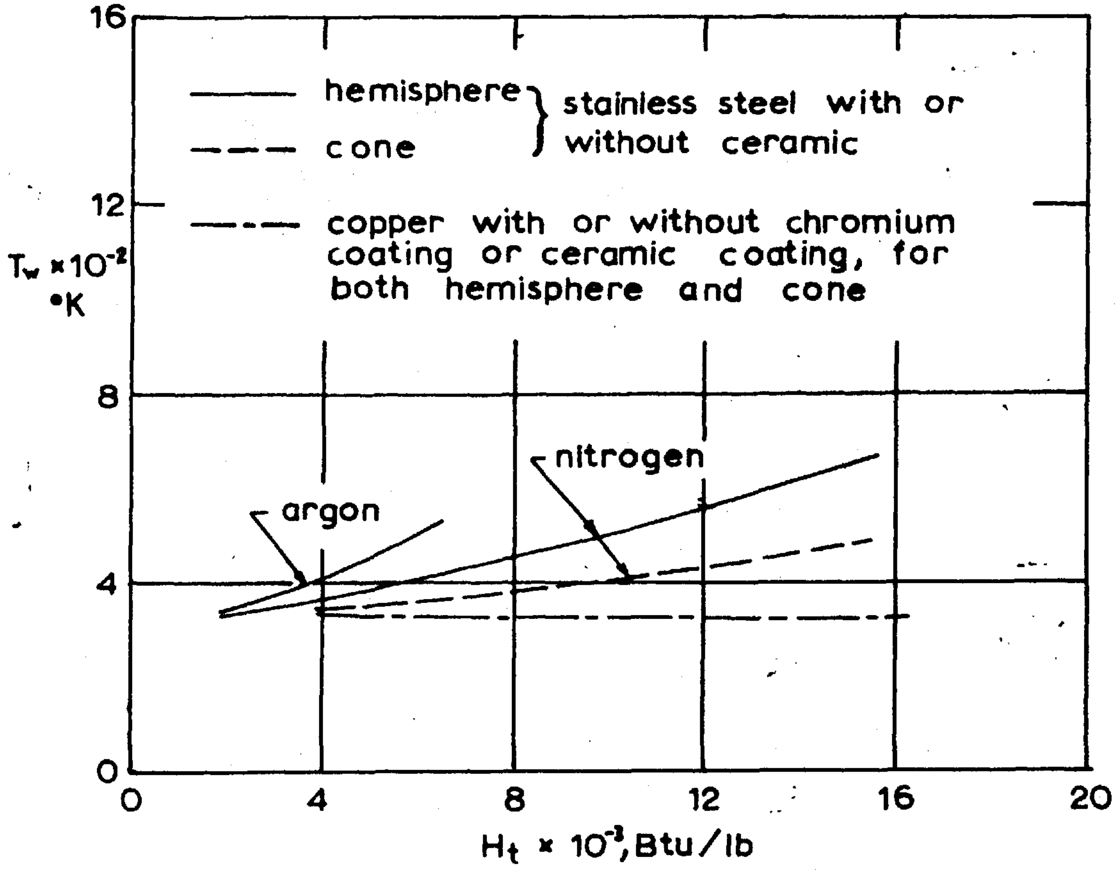

Fig. 11. Approximate average surface temperatures of models calculated for $\dot{m}$ = 0.1 lb/min.

approximately 15% in average. This means that the theoretical values of Q_c are, for some reason, underestimated by around 15%.

Allowing this possible error in the theoretical values of Q_c in Eq. (49), the most probable values of k_w are seen to fall within the following ranges;

i) copper hemisphere, $0.033T_w < k_w < 0.063T_w$

ii) chromium cone, $0.070T_w < k_w < 0.106T_w$

iii) stainless steel hemisphere,

$0.011T_w < k_w < 0.041T_w$

iv) ceramic hemisphere, $0 < k_w < 0.030T_w$

v) ceramic cone, $0 < k_w < 0.035T_w$.

Substituting the average surface temperature values $300 < T_w < 600^\circ K$ (see Fig. 11), it is seen that the catalytic recombination rate constant k_w for the metallic surfaces lies within the range expected by Goulard (Ref. 13)

$$10 < k_w < 60 \text{ fps} .$$

It is now possible to calculate the effective enthalpy from the values of measured heat transfer and the obtained catalytic rate constant. This calculation was carried out and the results are presented in Fig. 4 as H_{thx}. The calculated H_{thx} is subject to the inaccuracy in k_w at high enthalpy levels, but should be accurate at low enthalpy levels where the dissociation level is low. As mentioned in §II-3.1.1., the enthalpy determined in this way is closer to $H_{\epsilon pb}$, which suggests that the latent energy of ionization of vaporized electrode materials is recovered by the translational energy of the gas in the same manner as in nonequilibrium ionized argon gas (§ I-3.3.).

II-3.4. Radiative energy transport

The radiative energy transport from the nozzle exit flow in nitrogen was measured with the same bolometer as that described in §I-3.4. The same calibration curves, i.e. Fig. 20 of Part I, were used. The results of the tests are presented in Fig. 12. Shown also in Fig. 12 are the theoretical values calculated using the data of Yos (Ref. 11) (see §II-2.5.). As seen from Fig. 12, the experimental values of radiative heat transfer are at least three orders of magnitude greater than the theoretical value of continuum radiation determined using the semiclassical formula of Kramers (Ref. 21), irrespective of whether equilibrium or frozen ionization is assumed through the nozzle.

The enormously high experimental values of radiative heat transfer as compared with the theoretical values may be due to either one or both of the following reasons:

i) The semiclassical theory of Kramers is a poor

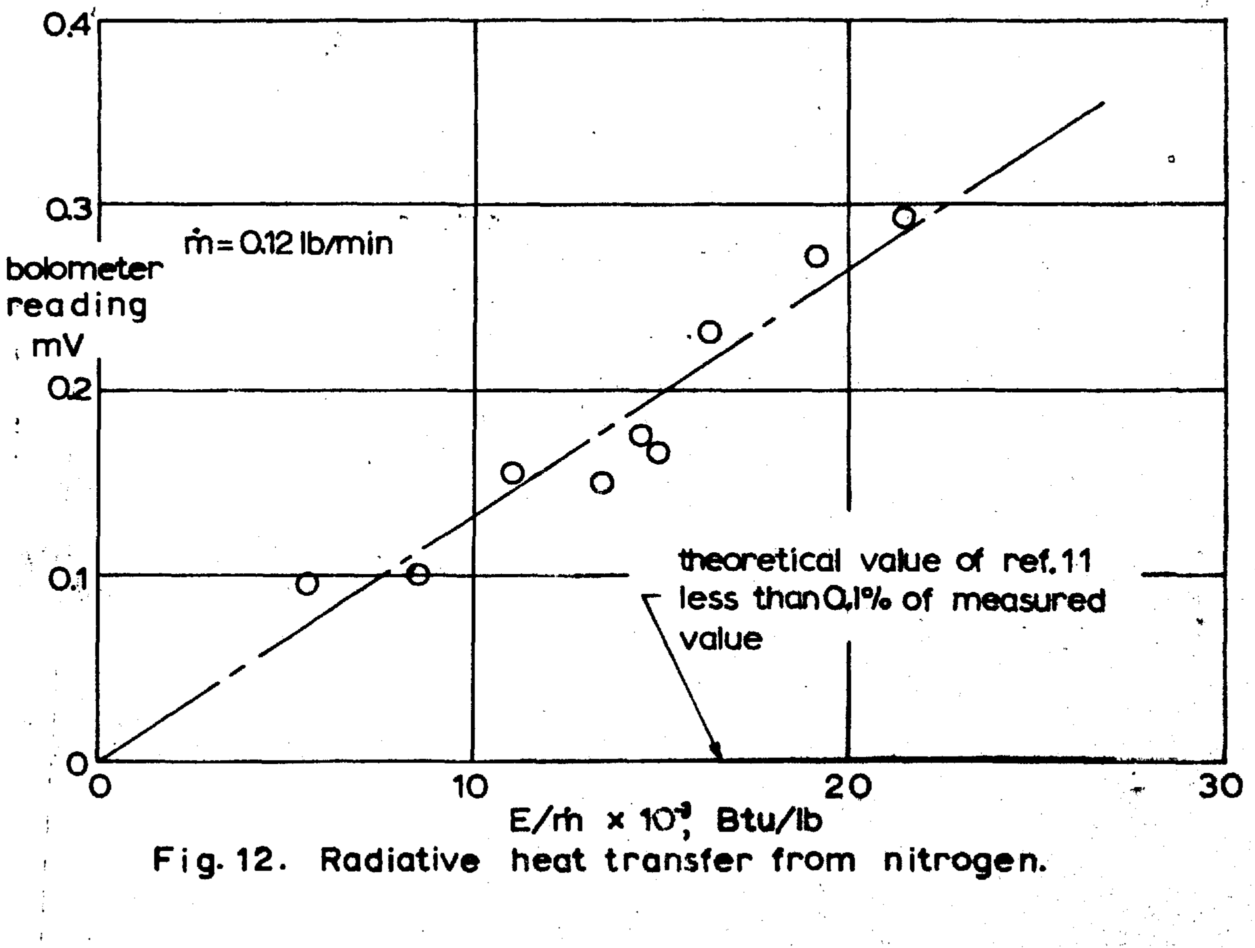

Fig. 12. Radiative heat transfer from nitrogen.

approximation to the true value. In the case of argon, the Kramers' theory gives a value for radiated power at least two orders of magnitude smaller than the quantum theory which is used in the work of Part I (see Ref. 32 of Part I). There is apparently no data available on the quantum theory of radiation from nitrogen and therefore Kramers' theoretical values are used here.

ii) The discrepancy may due partly to the presence of electrons derived from the metallic impurities, i.e. vaporized electrode materials. Because of the low ionization potentials of the contaminants, and/or the small ionic recombination of the contaminant ions, substantial numbers of electrons and metallic ions may still be present in the jet exit flow.

The experimental result of radiative heat transfer in nitrogen and also the work with argon (Part I, §I-3.4.), confirms that the radiation loss in the nozzle flow is negligibly small and the flow is almost perfectly adiabatic.

II-4. DISCUSSION

II-4.1. State of nitrogen flow in the wind tunnel

The flow Damköhler numbers in the Imperial College plasma-jet wind tunnel for nitrogen dissociation and recombination are quite low. Calculation shows that the characteristic Damköhler number of the flow in the settling chamber with respect to the dissociation of nitrogen is of the order unity. Ref. 25 reports that the flow may not reach equilibrium in the settling chamber even if the characteristic Damköhler number is considerably larger than unity. The stand-off distance of the bow shock wave for a hemisphere, and the heat transfer measurements taken ascertain that there is dissociation of nitrogen to a degree very much the same as that at the equilibrium level. Perhaps in the arc there is a dissociation rate quite different from that in a shock-compression. In shock-compression dissociation, the molecules obtain energy necessary for dissociation through collisions with other atoms or molecules, while in arc-dissociation, the energy may come partly through collisions with highly mobile electrons. Since the cross-section and the mean free path of the collision are different in the two cases, the dissociation rate may also be different.

The comparison of H_{tpb} with H_{tmf} shows that a significant amount of energy is absorbed in the vaporization of electrode materials, which are no doubt ionized subsequently. Thus the assumption of ionic equilibrium in the operation with nitrogen is seen to be a crude approximation. The presence of radio frequency oscillations in the nitrogen flow (see §II-3.1.3.) may partly be responsible for generation of excess electrons in the flow (see e.g. Ref. 26). An effort is currently being made to reduce the contamination level and the arc fluctuations.

The two methods of flow determination, i.e. the power balance and the pressure-mass flow methods, agree with each other when both the negative displacement thickness at the throat and the gas contamination by electrode materials are accounted for. The effect of gas contamination is quite large, particularly at low enthalpy levels. This point emphasizes the desirability of an impurity-free plasma-jet wind tunnel.

II-4.2. Transport properties

The viscosity values used here for the calculation of heat transfer rates to the hemisphere and cone models for comparison with the experimental results are those obtained from the (reduced) Chapman-Enskog method (see § II-2.4.). The values of viscosity calculated using the Sutherland formula, which has been used with much success for temperatures below 2500°K and which is indeed used by Ahtye and Peng (Ref. 12) for calculation in the dissociated and ionized regimes, are lower than the Chapman-Enskog method values by nearly 40% within the range of enthalpy levels tested. The present heat transfer results show a reasonable agreement with the theoretical values calculated by Yos's method. If the Sutherland formula is used, the experimental values will exceed the theoretical values by quite a large value at the lowest operating conditions. The results of the heat transfer measurement presented here, therefore, strongly support the use of the Chapman-Enskog approximation for the calculation of viscosities at temperatures above 2500°K.

The theoretical values for conductive heat transfer were taken basically from the work of Fay and Riddell (Ref. 17) which includes the effect of $n = \rho\mu/(\rho\mu)_e$, the Prandtl and the Lewis number. The correction factors accounting for these effects amount approximately to 1.7 at the high enthalpy levels tested. By incorporating this correction factor, the calculated conductive heat transfer rate was approximately 70% of the total heat transfer measured at high enthalpy levels. If those effects are neglected, therefore, the theoretical heat transfer due to conduction alone will account for only 40% of the total heat transfer rate measured. The remaining 60% which must be accounted for by surface recombination is impossibly high. This leads to the conclusion that for the calculation of conductive heat transfer from a dissociated gas, the effects of n, the Prandtl and the Lewis numbers must be considered. It must be recalled also that the values of the

Prandtl and the Lewis numbers have been calculated using the work of Yos (Ref. 11) which utilizes the Chapman-Enskog method. If the method of Hansen (Ref. 14) or equivalently of Ahtye and Peng (Ref. 12)(which uses the simple collision model) is used, these effects will be less pronounced (the corrective factor will be 1.5 maximum) and therefore the agreement between theory and experiment will be poorer. This point again emphasizes the use of the Chapman-Enskog method for a dissociated gas.

II-4.3. Surface catalysis

The reasons for choosing boro-silicate ceramics for testing in the role of low catalytic materials were;

i) they are the only industrially available high temperature ceramics at present that withstand the required operating conditions,

ii) their strong adhesion and good mechanical properties (see Ref. 27),

iii) a large thickness is easily obtainable, and

iv) the uncertainty and variability of the catalytic rate constant of a material under the various conditions (Ref. 28) do not warrant the use of an elaborate or especially pure coating material.

The second and third points are important particularly in regard to the experimental condition of the present work. In these experiments, the conditions were such that in the starting process, thermal shock can cause a temperature difference of well over 1000 °C across the faces of the coating. A substantial coating thickness of around 0.001" was necessary because the surface needed to be polished frequently with abrasives to remove the foreign material deposited on the surface of the model. The vacuum evaporation method used by Busing (Ref. 29) or the contact fusing utilized by Leah (Ref. 30) were not suitable for these reasons.

It is generally believed (Ref. 13) that pure silicon monoxide and silica have such a low catalytic activity for oxygen recombination that they can be taken as practically non-catalytic under such conditions as in the present work. But this point is not at all conclusive when considering high surface temperatures. Also the catalytic recombination rate for nitrogen may be somewhat different from that for oxygen. The bombardment of the surface by the high energy particles contained in the plasma-jet wind tunnel flow and the contamination of the surface with impurities may change the catalytic rate. For these reasons the pure silicon oxides were not used in the present experiment. The boro-silicate ceramics used instead consist mainly of the oxides of silicon and boron and therefore were supposed to have catalytic rates comparable with that of the silicon oxides. The result of the present experiment shows that these ceramics are substantially less catalytic to nitrogen recombination than the metals used.

II-4.4. Freezing of the wind tunnel flow

The stand-off distance measurement confirms that the flow of the plasma-jet wind tunnel used is indeed frozen for both dissociation and vibrational excitation. The frozen nature of the flow is used in the present work as an advantage; that is, the atom concentration and other flow properties are determined in a simple way making use of the condition of constant atom concentration. This approximation made the determination of the surface catalytic reaction rate constant k_W quite simple. If the dissociation is relaxing through the nozzle and behind the shock wave, another unknown factor must be determined, i.e. the rate constant. Thus a completely frozen flow is suitable for a heat transfer experiment with catalytic and non-catalytic surfaces.

The frozen wind tunnel flow is a good simulation of the flight condition as regards the atom concentration level at the edge of the stagnation point boundary layer. Up to an altitude of about 200,000 ft, the atom concentration at the edge of the stagnation point boundary layer of a re-entering blunt body is equivalent to the equilibrium value in the inviscid region, and therefore it is simulated in the wind tunnel by reproducing the same atom concentration level in the settling chamber in a frozen flow. Beyond 200,000 ft, however, Chung (Ref. 31) and the present author (Ref. 16) have shown that the atom concentration at the edge of a boundary layer is decreased by the lack of equilibrium in the shock layer. For the simulation of altitudes above 200,000 ft, therefore, it is necessary to produce a near-equilibrium condition in the test section. Near-equilibrium flow is also necessary to prevent the loss of thrust inherent with frozen flow, for the study of ram-jet engines (see e.g. Ref. 32).

The required settling chamber pressure for the production of dissociative equilibrium at the test section was determined by solving the freezing criterion (see Eq. (15))

$$K_F = 1$$

for two nozzle geometries and is presented in Fig. 13. As seen from Fig. 13, it is essential to maintain the settling chamber pressure high enough to produce a near-equilibrium flow in the test section for test flow Mach numbers $M > 2$.

A possible method of equilibrating the exit flow in a nozzle is to add a 'catalyst' to the flow which may increase the effective recombination rate. An effort has been made by the present author to find a catalyst for nitrogen recombination and also for the reactions in hydrogen-oxygen products in the plasma-jet wind tunnel. The tests proved unsuccessful however, mainly because of the instability of the arc induced by the injection of the foreign materials.

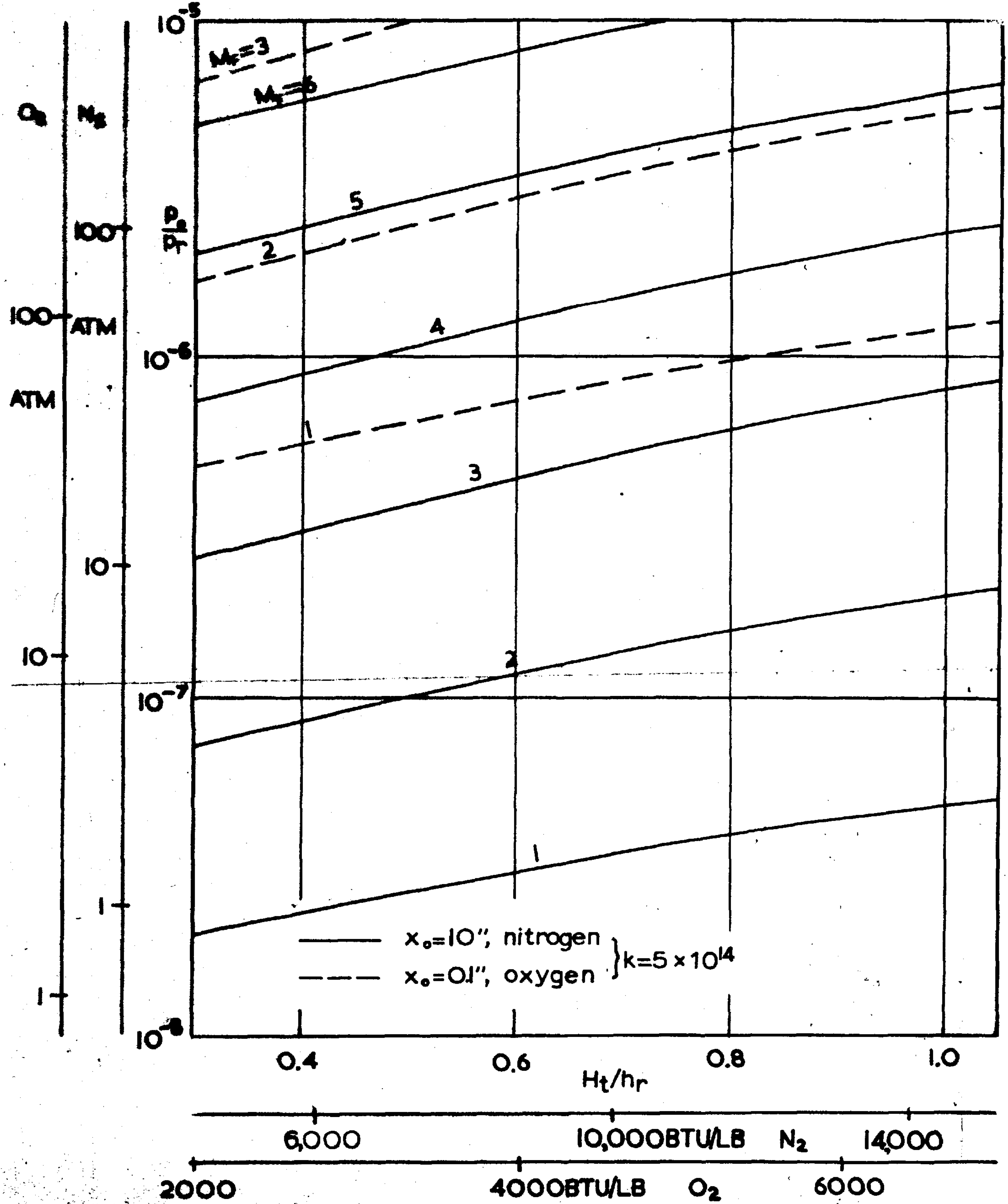

FIG. 13. APPROXIMATE FREEZING POINT MACH NUMBER FOR DISSOCIATING GAS.

II-5. CONCLUSIONS

i) For an approximate calculation of vibrational excitation and dissociation levels in a relaxing convergent-divergent nozzle flow, the criteria

$K_F = 4$, for vibration, and

$K_F = 1$, for dissociation

agree with the exact solution to within ±5%.

ii) The increase of the shock wave stand-off distance of a sphere in a frozen dissociated flow is confirmed.

iii) Two methods of determining the flow properties in a plasma-jet wind tunnel, i.e. the power balance and pressure-mass flow methods, are shown to agree approximately after correcting for the negative displacement thickness at the throat and for gas contamination.

iv) Copper, chromium and stainless steel have surface catalytic reaction rate constants of the order of 10 fps for nitrogen recombination and the two boro-silicate ceramics used are much less catalytic than those metals.

v) The heat transfer results support the use of the Chapman-Enskog approximation instead of the simple collision model in the calculation of transport properties at high temperatures and refutes extrapolation of the Sutherland formula to higher temperatures.

vi) The experimental values of radiative heat transfer are several orders of magnitude greater than those predicted by the semiclassical theory of Kramers.

II-6. REFERENCES

1. Lighthill, M.J., J. Fl. Mech. 2 1 (1957)
2. Herzfeld, K.F., Thermodynamics and Physics of Matter (Princeton series) B. 111 (Oxford, London) (1955).
3. Freeman, N.C., J. Fl. Mech. 4 407 (1958)
4. Wray, K., Teares, J.D., Kivel, B., & Hammerling, P., AVCO-Everett RR-83 (1959)
5. Stollery, J.L., & Smith, J.E., J. Fl. Mech. 13 225 (1962)
6. Stollery, J.L., & Park, C., Imperial College Aero. Rep. 115 (1963), to be published in J. Fl. Mech.
7. Bray, K.N.C., "Atomic recombination in a hypersonic wind tunnel nozzle", ARC 20,562 (1958)
8. Blythe, P.A., J. Fl. Mech. 17 126 (1963)
9. Bernstein, L. "Tabulated solutions of the equilibrium gas properties behind the incident and reflected normal shock-wave in a shock-tube", ARC 22,778 (1961)
10. Admur, I., & Mason, E.A., Phys. Fl., 1 370 (1958)
11. Yos, J.M., AVCO-RAD TM-63-7 (1963)
12. Ahtye, W.F., & Peng, T.C., NASA TN D-1303 (1962)
13. Goulard, R.J., Jet Prop. 28 737 (1958)
14. Hansen, C.F., NASA TR R-50 (1959)
15. Kennard, E.H., "Kinetic theory of gases" Chap. 4 (McGraw-Hill, New York) (1938)
16. Park, C., "Dissociative relaxation in viscous hypersonic shock layers", to be published in AIAA J.

17. Fay, J.A., & Riddell, F.R., J. Aero. Sci. 25 73 (1958)

18. Kemp, N.H., Rose, P.H., & Detra, R.W., J. Aero. Sci. 26 421 (1959)

19. Wood, B.J., & Wise, H., "The interaction of atoms with solid surfaces", Rarefied Gas Dynamics (Academic Press, New York) (1961)

20. Freeman, N.C., & Simpkins, P.G., "On the diffusion of species in similar boundary layers with finite recombination rate at the wall", to be published in Quart. J. of Math. & Appl. Mech.

21. Unsöld, A., "Physik der Sternatmosphären", 2nd ed. (Springer, Berlin) 163 (1955)

22. Park, C., "Measurement of heat transfer to a hemisphere in high enthalpy argon and nitrogen streams in a plasma-jet wind tunnel", ARC 24,948 (1963)

23. Harvey, J.K., Simpkins, P.G., & Adcock, B.D., AIAA J. 1 714 (1963)

24. Simpkins, P.G., private communications (1963)

25. Arney, G.D., & Boylan, D.E., AEDC-TDR-63-19 (1963)

26. Meek, T.M., & Craggs, T.D., "Electrical breakdown of gases", Chap. 9 (Oxford, London) (1953)

27. Potter, D.M., Aircraft Production 23 354 (1961) and 23 417 (1961)

28. Rosner, D.E., private communications (1961)

29. Busing, J.R., "The effect of catalytic surfaces on stagnation

point heat transfer in partially dissociated flows", preprint AGARD Spec. Mtg. Rhode-St.-Genese, April (1962)

30. Leah, A.S., Rounthwaite, C., & Bradley, D., Phil. Mag. 61 468 (1950)

31. Chung, P.M., NASA TR R-109 (1961)

32. Lezberg, E.A., & Lancashire, B., NASA TN D-1052 (1961)

ACKNOWLEDGEMENT

The author expresses his sincere thanks to Mr. J. L. Stollery for his inspiring supervision and kind interest.

This research was made possible by the award of the British Council Scholarship for 1961 - 1963, and financial assistance through the good offices of Prof. P. R. Owen in 1963 - 1964. This opportunity is taken to tender thanks to all concerned.

$\dot{m}$, MASS FLOW RATE, LB/MIN
P_o, PLENUM CHAMBER PRESSURE, ATM
T_o, " TEMPERATURE, °K
i_o, " ENTHALPY, BTU/LB
α_o, " ATOM CONCENTRATION, %

$\dot{m}$ BASED ON THROAT DIAMETER 0.447 INCH. FOR OTHER THROAT DIAMETERS, MULTIPLY $\dot{m}$ BY

$$\left(\frac{\text{THROAT DIAMETER IN INCH}}{0.447}\right)^2.$$

FOR ENTHALPY VALUES BELOW 2500 BTU/LB, USE THE FORMULA

$$i_o = 1666\left(\frac{P_o \text{ ATM}}{\dot{m} \text{ LB/MIN}}\right)^2 \text{ BTU/LB}$$

AND ASSUME PERFECT GAS

EFFECTIVE γ FOR ALL PURPOSES:

$$\gamma = \frac{7+3\alpha}{5+\alpha}$$

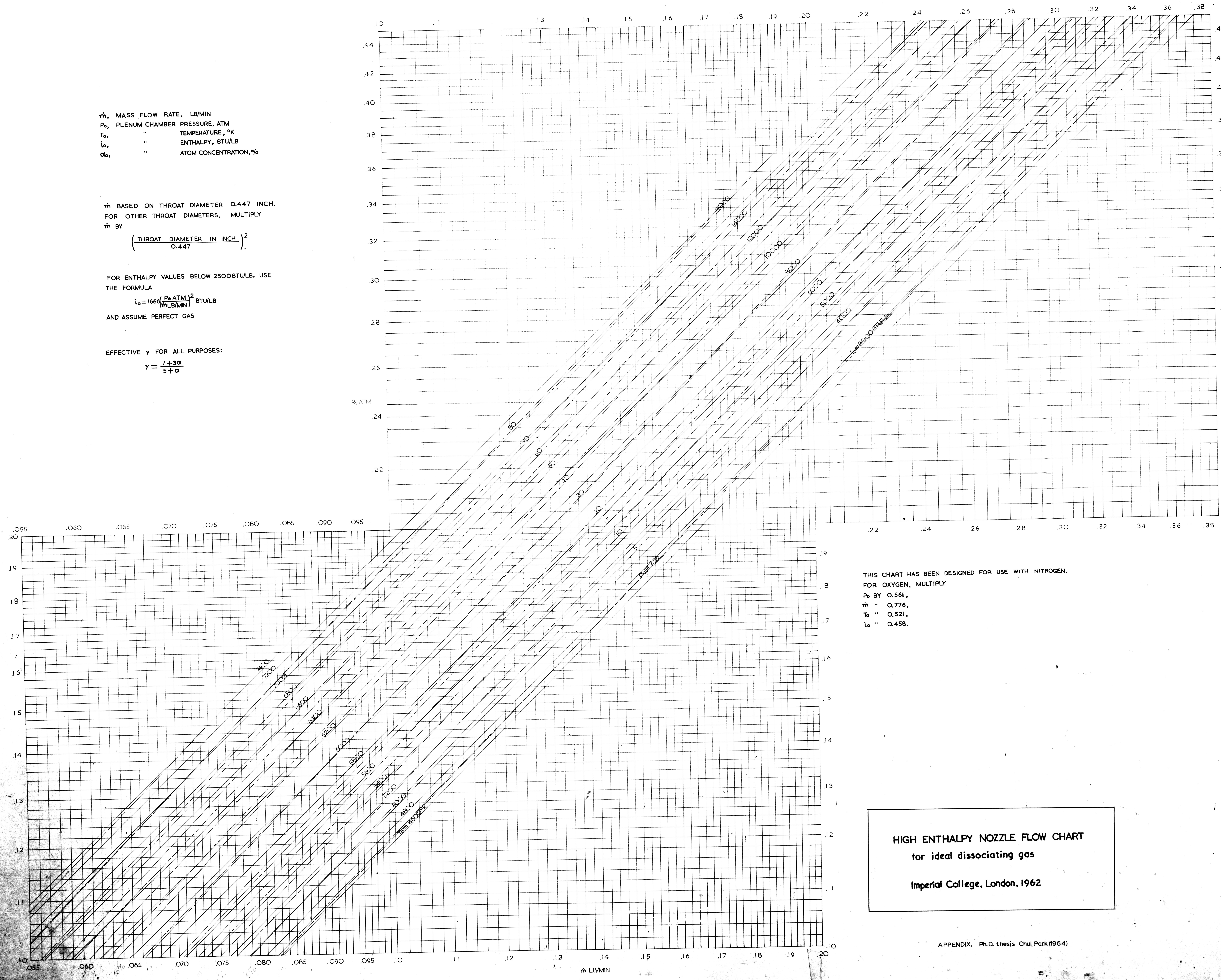

THIS CHART HAS BEEN DESIGNED FOR USE WITH NITROGEN.
FOR OXYGEN, MULTIPLY
P_o BY 0.561,
$\dot{m}$ " 0.776,
T_o " 0.521,
i_o " 0.458.

HIGH ENTHALPY NOZZLE FLOW CHART
for ideal dissociating gas

Imperial College, London, 1962

APPENDIX. Ph.D. thesis Chul Park (1964)